POLITECNICO DI MILANO

Facoltà di Ingegneria Industriale

Corso di Laurea in
Ingegneria Aeronautica

INNOVATIVE METALLIZED NANO-SIZED ADDITIVES FOR HYBRID ROCKET PROPULSION

Supervisor: Prof. Luigi DE LUCA

Co-Supervisor: Dr. Christian PARAVAN

Authors:

Paolo LEONI Matr. 735809

Giulio VADALA' Matr. 755724

Academic Year 2011 - 2012

Acknowledgments

Questo lavoro non sarebbe stato possibile senza l'idea del prof. DeLuca che vogliamo ringraziare per la sua fiducia e costante presenza.

Desideriamo ricordare inoltre tutti i membri del laboratorio e gli amici di SPLab. In particolare Alice, Pietro, Stefano, Matteo, Marco, Fabio, Elena, Luca, Andrea, il prof. Galfetti e il sig. Colombo per l'infinita disponibilità e Filippo per averci insegnato il valore delle domande e della discussione scientifica.

Un pensiero di ringraziamento anche ad amici, famigliari e tutti coloro che ci sono stati accanto con affetto e comprensione.

Infine un ringraziamento speciale è per Christian che più di ogni altro
ci è stato vicino, per ciò che ci ha insegnato, per la sua competenza,
la sua inesauribile pazienza e la sua amicizia.

Grazie

Abstract

This work of thesis is focused on production, characterization and test of bimetallic nanometric Aluminum-Copper powders used as additives in hybrid fuels.

Powders were produced and characterized in the *Institute of Strength Physics and Materials Science & Department of Technical Physics of Tomsk State University* in Tomsk, Russian Federation. Further test have been performed in Aerospace *Propulsion Laboratory of Politecnico di Milano(SPLab) , Italy.*

The objective of the work is the ballistic characterization of new bimetallic Aluminum Copper powders used as additives in hybrid HTPB based fuels. Seven different Al-Cu concentration powders have been produced by EEW method, from ALEX^{TM} to pure Copper powders. For all the types, a coated version has been created. Every fuel has a 10% concentration in weight of powders. All tests were performed using pure liquid oxygen.

Several Al-Cu powders loaded fuels exhibit enhancements of regression rate and mass burning rate with respect to pure HTPB fuel. Moreover Al-Cu powders with the 15% and 74% of Aluminum exhibit better performances with respect to ALEX^{TM} in every tested condition (G_{ox} from 150 to 350 kg/m^2s). Fuel regression rate percent increase for both formulation is higher than 23 % for G_{ox}= 150 kg/m^2s and 15 % for 350 kg/m^2s. Percent increase in mass burning rate is even better than regression rate one, especially for Al15-Cu85 powders, because of the higher density of Copper (8920 kg/m^3) with respect to Aluminum (2700 kg/m^3). Furthermore, in every tested formulation addition of copper in powders lowers the influence of oxidizer flux on fuel regression rate. This is an advantage connected to an easier control of thrust for a possible practical application of these powders. Powders with high concentration of Aluminum or Copper exhibit the best performances. On the other hand, powders with approximately the same concentrations are characterized by low regression rate in every condition. The comparison between DSC-TG analysis and Hybrid motor ballistic tests exhibits a high influence of maximum heat flux and oxidation peak temperature of powders on performances of metal loaded fuels. Introduction of coating is connected to a general decrease of fuel regression rate, especially for the fastest formulations. For high G_{ox}, big reductions of r_f were observed. On the other hand, for low G_{ox} coated powder loaded formulations are equal or faster than uncoated ones. Moreover coating reduces the influence of oxidizer flux on fuel regression rate.

Sommario

Il presente lavoro di tesi si colloca nell'ambito dello studio dei motori ibridi per la propulsione aerospaziale. L'obiettivo consiste nella produzione, caratterizzazione e utilizzo, all'interno di combustibili ibridi, di nuove polveri bimetalliche a base di Alluminio e Rame.

La fase di produzione e caratterizzazione delle polveri è stata svolta presso *Institute of Strength Physics and Materials Science* e *Department of Technical Physics of Tomsk State University,* entrambi a Tomsk, Russia. La fase di analisi sperimentale su combustibili ibridi è stata interamente svolta presso il *Laboratorio di Propulsione Aerospaziale* del Politecnico di Milano (*SPLab*). Sono stati prodotti 7 tipi di polveri, caratterizzate ognuna da una diversa concentrazione di Alluminio e Rame. Una parte del quantitativo prodotto è stato poi rivestito da Fluorel™ e Telomer n5 in modo di avere due diverse versioni per ogni polvere: una ricoperta e una uncoated. I combustibili utilizzati per i test balistici sono tutti a base di HTPB e additivati con una concentrazione, pari al 10% in massa, di polveri metalliche. Le prove sono state tutte eseguite in ossigeno puro.

Molte delle formulazioni testate sono caratterizzate da velocità di regressione r_f significativamente superiori alla baseline di HTPB senza alcun additivo metallico. Particolarmente interessanti sono i combustibili caricati con polveri al 15% e 74% di Alluminio. L'aggiunta di queste due polveri ha infatti permesso un incremento della r_f, in ogni condizione di flusso investigata (G_{ox} da 150 a 350 kg/m^2s) anche rispetto al combustibile caricato con ALEX™. Per entrambe le formulazioni l'aumento percentuale di r_f è superiore al 23% per G_{ox} = 150 kg/m^2s e maggiore al 15% per G_{ox} = 350 kg/m^2s. I risultati relativi all'aumento percentuale della portata massica di combustibile rilasciato sono addirittura migliori. La densità del rame (8920 kg/m^3) è infatti molto superiore a quella dell'alluminio(2700 kg/m^3). In tutti i casi inoltre la presenza del rame, in parziale o totale sostituzione dell'Alluminio, ha portato a una riduzione dell'influenza del G_{ox} sulla r_f. Quest'ultimo è un vantaggio connesso principalmente ad un più facile controllo del livello di spinta in una possibile applicazione pratica di questi combustibili. Le migliori prestazioni sono state ottenute con polveri caratterizzate da un'alta concentrazione di uno degli ingredienti (Al o Cu). Al contrario, i combustibili additivati con polveri aventi una simile concentrazione di Alluminio e Rame sono quelli che hanno mostrato le r_f più basse. Un'analisi incrociata tra le prestazioni ottenute nei test balistici e i risultati delle prove DSC-TG sulle polveri ha mostrato una possibile influenza del massimo flusso di calore e della temperatura del primo picco di ossidazione sulla r_f.

Nelle condizioni investigate l'aggiunta del coating ha portato ad una generale riduzione della r_f, specialmente per le formulazioni più veloci. I decrementi si sono registrati specialmente ad alti G_{ox}. Per bassi flussi (G_{ox} < *200* kg/m^2s) i combustibili con polveri coated hanno mostrato r_f simili o superiori a quelle delle formulazioni con polveri non ricoperte. L'introduzione del coating, nelle condizioni di flusso investigate, ha il vantaggio di limitare la dipendenza di r_f da G_{ox}.

Contents

List of Figures

List of Tables

Symbols and Acronyms

Latin Symbols

B	-	*Blowing parameter*
Cal	*pixels/mm*	*Calibration equivalence*
D	-	*Calibration distance*
F	-	*Friction factor*
G	kg/m^2s	*Specific mass flow*
H	W/m^2K	*Effective convective heat transfer coefficient*
I_{sp}	*s*	*Specific Impulse*
I_{vol}	$s\ kg/m^3$	*Volumetric Specific Impulse*
M	*kg*	*Mass*
$\dot{m}$	$kg\ /\ m^2$	*Mass flux*
n_r	-	*Power exponent*
P_r	-	*Prandtl Number*
P	*Mpa*	*Pressure*
Re	-	*Reynolds number*
r_f	*mm / s*	*Fuel regression rate*

T	*K*	*Temperature*
T	*S*	*Time*
X	-	*Cartesian longitudinal coordinate*
Y	-	*Cartesian vertical coordinate*

Greek Symbols

Δh_f	*J/ kg*	*Net Fuel Enthalpy*
$\Delta \dot{m}_{f,\%}$	-	*Mass Burning Rate Percent Increase*
$\Delta n_{r,\%}$	-	n_r *Percent Increase*
$\Delta r_{f,\%}$	-	*Fuel Regression Rate Percent Increase*
P	kg/m^3	*Density*

Abbreviations

Al	-	*Aluminum*
ALEX™	-	*Nano Aluminum Uncoated Powder*
Al_2O_3	-	*Alumina*
AMROC	-	*AMerican ROcket Company*
$Ca(OH)_2$	-	*Calcium Hydroxide*
CO_2	-	*Carbon Dioxide*
Cu	-	*Copper*

CuO	-	*Cupric Oxide*
Cu_2O	-	*Cuprous Oxide*
DOA	-	*Dioctyl Adipate*
DoD	-	*Department of Defense*
DSC	-	*Differential Scanning Calorimetry*
EEW	-	*Electric Explosion of Wires*
Gox	$kg/(m^2s)$	*Oxygen Mass Flux*
HAHST	-	*High Altitude High Speed Target*
HAST	-	*High Altitude Supersonic Target*
HPDP	-	*Hybrid Propulsion Demonstration Program*
HPIAG	-	*Hybrid Propulsion Industry Action Group*
HRE	-	*Hybrid Rocket Engine*
HTPB	-	*Hydroxyl Terminated Polybutadiene*
HyTOP	-	*Hybrid Technology Options Project*
IPDI	-	*Isophorone Di-Isocynate*
IRFNA	-	*Inhibited Red Fuming Nitric Acid*
ITCS	-	*Integrated Tracking and Control System*
JIRAD	-	*Joint Government/Industry Research and Development*
JPL	-	*Jet Propulsion Laboratory*
LEX	-	*Lithergol Experimental*
LRE	-	*Liquid Rocket Engine*
LOX	-	*Liquid Oxygen*
MgO	-	*Oxygen Mass Flux*
MON	-	*Mixture of Oxides of Nitrogen*
NASA	-	*National Aeronautics and Space Administration*

NOX	-	*Binary compound of Oxygen and Nitrogen*
Nlpm	-	*Normal liters par minute*
O_2	-	*Oxygen*
PMMA	-	*Plexiglass*
P_r	-	*Prandtl Number*
Rpm	-	*Rounds par minutes*
SEM		*Scanning Electron Microscope*
SRM	-	*Prandtl Number*
TIN	-	*Dybutylin Diacetate*
TOT		*Thickness over Time*
TEM	-	*Transmission Electron Microscopy*
TGA	-	*Thermogravimetric analysis*
TMD	-	*Theoretical Mass Density*
UDP-5	-	*Machine used for metal nanopowders production by EEW method*
UTC-CSD	-	*United Technology Center – Chemical System Division*
XRD	-	*X-Ray Diffraction*
ZnSe		*Zinc Selenide*

1. Introduction

1.1. Motivations

Termochemical propulsion is the key technology for access to space [1] [2]. In thermochemical systems, reaction of oxidizer and fuel enables conversion of reactant chemical bond energy into thermal energy of the propellant. The latter is then converted in kinetic energy by the gasdynamic nozzle. Thermochemical propulsion systems serve also in several in-space applications (as orbital maneuvering, attitude control, soft-landing, de-orbiting).

Thermochemical propulsion systems are classified according to the state of matter of the reactants into solid, liquid and hybrid propellants.

In Solid Rocket Motors (Figure 1.1), the fuel and oxidizer are chemically premixed and formed into a solid propellant grain. The chemical reactions in the combustion chamber are activated by ignition, leading to the transformation of the primary chemical energy into the thermo-chemical secondary energy. The gaseous combustion products are then expanded in a gasdynamic nozzle producing the thrust. Solid motors are very simple. However, they are not as efficient as liquid motors, cannot be throttled or stopped, and may present an explosion hazard.

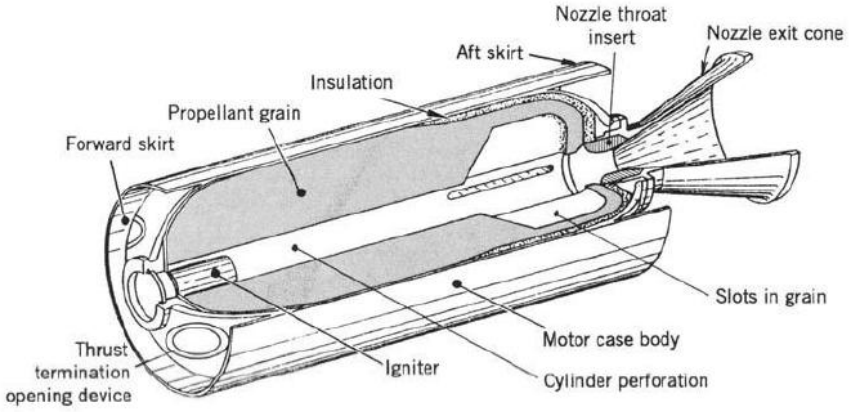

Figure 1.1: Architecture of a Solid Rocket Motor [2].

Liquid Rockets Engines (Figure 1.2) use liquid fuel and liquid oxidizer stored in different tanks. The propellants are either pressure fed or pumped from their tanks into a combustion chamber. Liquid Rocket Engines generally provide a good level thrust, can be throttled, and are characterized by a higher efficiency. However, due to plumbing complexity, redundancies for reliability, and propellant storage issues, LRE cost and weight can be high.

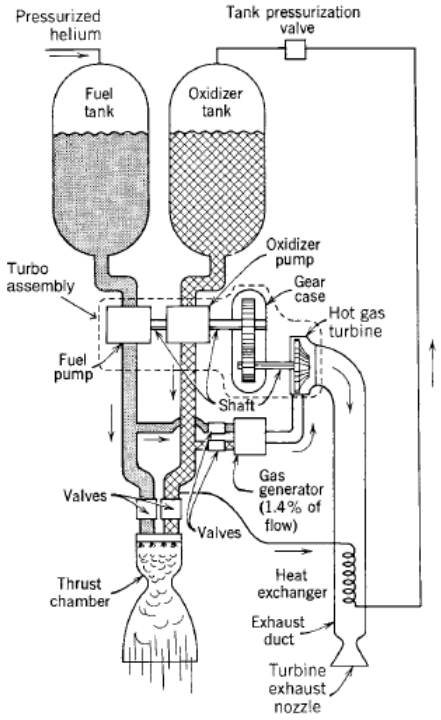

Figure 1.2: Simplified schematic diagram of one type of liquid propellant rocket engine with a turbo pump feed system and a separate gas generator [2].

Hybrid motors combine elements from both systems. The hybrid rocket engines (HREs) are devices in which oxidizer and fuel are stored separately in two different physical states. The most common type, called *direct HRE* (Figure 1.3), presents a solid fuel grain stored in the combustion chamber and a fluid (gaseous or liquid) oxidizer stored in a separated tank. The *reverse HRE* proposes a solid oxidizer grain with a fluid fuel. This work will focus only onto the direct HREs. Gaseous or liquid oxidizer is, in general, liquid oxygen (LOX) or nitrous oxide (NOX). Fuel grain is generally plastic or rubber. A source of ignition is applied to the fuel grain, vaporizes some of the fuel, and the oxidizer is injected into the chamber. High temperature and pressure combustion products generate thrust passing through the nozzle.

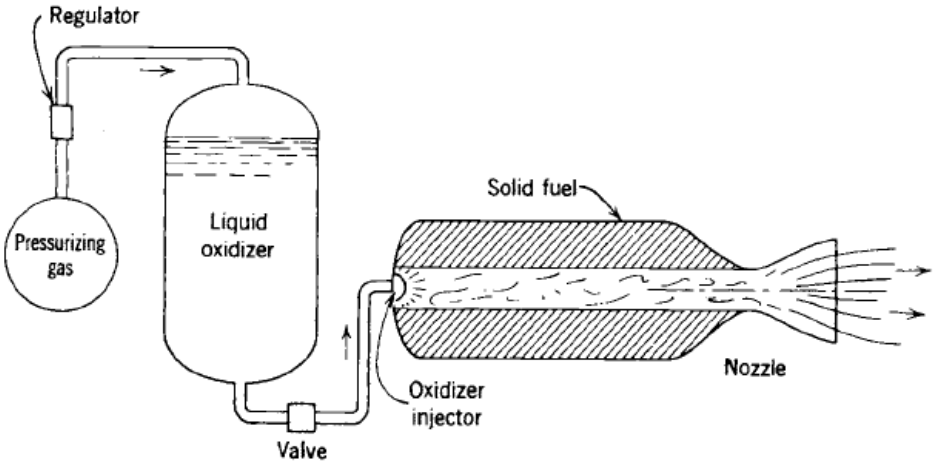

Figure 1.3: Architecture of a direct Hybrid Rocket Engine [2].

The use of HRE systems has many advantages in comparison with LREs or SRMs [3] [4]. The main are listed below:

- *Safety.* In the early stages of manufacturing, assembly, transport and operations on the launch pad only inert materials are used. Therefore is impossible any accidental ignition due to shock, vibration, static electricity as observed in SRMs. Moreover, in case of emergency, it is also possible the shut off the engine simply by interrupting the flow of the fluid component into the combustion chamber. Furthermore, the pressure in a HRE combustion chamber is proportional to the mass flow entering in the combustor and not to the surface area exposed to the flame. It excludes the possibility of dramatic events such as explosions caused by breakage or cracks in solid grain.
- *Versatility.* In Hybrid Rocket Engines, like LREs, is possible to easily control the level of thrust during the mission. Moreover HREs architecture is simpler than LREs one.
- *Costs.* Hybrid propulsion is characterized by lower costs than LRE one thanks to the simple architecture of the engine and the wide choice of propellants.

- *Environmental safety.* In HREs it is possible to use less dangerous oxidizer than Ammonium Perchlorate used in SRMs.
- *Good Performances.* The value of HREs Specific Impulse I_{sp}[1] is between 280 and 350*s*. This value is better than every type of solid motor (Table 1.1). Cryogenic LREs can reach and overcome HREs specific impulse. On the other hand for hybrid motors the volumetric specific impulse I_{vol}[2] is still bigger because of the density of reactants.

Table 1.1: Maximum I_{sp} for different thermochemical motors [1].

Technology	Maximum I_{sp} [*s*]
Solid Motor	270
Hybrid Engine	350
Liquid Engine(Cryogenic)	500

On the other hand, it is necessary to consider some drawbacks that still prevent the full development of this class of engines. First of all, the low fuel regression rate that does not allow use of HREs as launch systems. Moreover variation of the mixture ratio during mission, difficulties to operate on large scales, rough and inefficient combustion in comparison to the corresponding values obtained in SRMs are other problems to solve.

1.2. Objectives

The main objective of the work is the fuel regression rate enhancement in Hybrid motors by innovative metal nanopowders.

In detail work is focused on bimetallic Aluminum-Copper powders. These additives could have a double effect inside a Hybrid Rocket Engines.

The high reactivity of copper in combustion can be a catalyst for Aluminum oxidation.

The main problem in Aluminum combustion is the oxide coating that has an high melting point, much more higher than Aluminum one [5] [1].

[1] I_{sp} is the total impulse that the motor generates per unit of propellant weight expressed in second (s)

[2] I_{vol} is the total impulse delivered per unit of propellant volume

During production of Aluminum-Copper nanopowders by Electric Explosion of Wires method it is proved that copper tends to stay on the surface because of its higher melting temperature [6].

In this way copper could partially substitute Alumina coating on powder increasing their reactivity.

Moreover Copper is denser than Aluminum, so bimetallic powders increase fuel density. So in the same fuel regression rate conditions Aluminum-Copper powders could create a higher mass release.

Another aspect is related to intermetallic compounds [7]. Vaporized Aluminum and Copper can create, after a fast condensation, new metallic structures not deeper studied yet. Behavior of these materials in combustion is still unknown, and it is possible that some could be very energetic and reactive.

Production of bimetallic powders by EEW method is more complicated than monometallic ones, so the first part of the work is focused on production and characterization of these new materials. All these powders were produced in the *Institute of Strength Physics and Materials Science* in Tomsk by the authors of the present work, thanks to the help of its stuff.

Some quantity of each powder has been coated with a Fluorinated Polymer (Fluorel™+ Telomer n5). So a second aim of this work is to evaluate the differences in combustion behavior of hybrid fuels due to addition of coating.

In general, coating is used to stabilize active metal concentration inside powders [8]. In this case decomposition of coating generates oxidizer products during combustion, due to Fluorine. This could increase fuel regression rate.

1.3. Presentation Plan

This work is composed of different sections:

- Chapter 2: Literature Survey, with a short description of hybrid rocket history. A review of previous works concerning hybrid rockets ballistics is also presented.

- Chapter 3: Solid Fuel Formulations, in which the HTPB-based fuel compositions tested are described. Details on chemical components are also given.

- Chapter 4: Production and Characterization of Powders, in which all powders production phases, are fully described. At least a series of characterization tests (DSC-TGA, TEM, and Centrifuge) is presented.

- Chapter 5: Samples Manufacture, a description of the procedures used to prepare the fuel samples is given. For each fuel theoretical and real concentration of all ingredients is listed.

- Chapter 6: Experimental Set-Up, a presentation of the experimental micro burner used during the data collection is provided. A description of the mathematical procedure used to evaluate the regression rate is also given.

- Chapter 7: Experimental Results, in which the fuel regression rate for every type of fuel is analyzed. Particular attention is given to the effects due to introduction of coating and copper inside powder.

- Chapter 8: Conclusions and Future Developments, a presentation of conclusions and possible future developments.

Production of powders by EEW method was performed in the *Institute of Strength Physics and Materials Science SB RAS, pr. Akademicheskii 2, Tomsk, 634021 Russia.*

Characterization of metal particles was made in *Department of Physics of Tomsk State University, 36 Lenin Prospekt, Tomsk, 634050, Russia*.

Fuel production and characterization was completely performed in *SPLab, Politecnico di Milano, Via La Masa 34, Milano, 20156, Italy* .

2. State of the Art of Hybrid Propulsion

In this chapter history of hybrid rocket engines development and fundamentals of hybrid combustion mechanism are reviewed. State of the art of research activity on HREs will be discussed with focus on studies on techniques for regression rate enhancement.

2.1. History

As for solid and liquid rockets, hybrid propulsion was born in early 1930s. The solid propellants were investigated by well known figures as Robert Goddard and Hermann Oberth. These pioneering studies highlighted the explosion hazards of propellant formulations. Oberth stated "Powder believes it must explode all at once; from the old use in shells and guns, it is too well trained always to destroy" [9]. A tragic demonstration of this dictum occurred in 1933 when the rocket engineer Reinhold Tiling, and three of his assistants were killed in a detonation of about 20 *kg* of powder fuel.

Meanwhile in Russia there were a number of amateur groups and solitary researchers in existence, but GIRD[3] was the world's first large professional rocketry program. The group was organized as four brigades and ten projects to study rocket engines and also winged and wingless missiles. Sergey Korolev, the future leader of the Soviet space program, was the over-all director of GIRD, as well as a brigade leader and the chairman of its technical council.

[3] Группа изучения реактивного движения, Group for the Study of Reactive Motion, abbreviated ГИРД, GIRD

Fridrikh Tsander headed the GIRD's 1st Brigade, which comprised Tsander's research team, transferred from the Institute of Aircraft Engine Construction (IAM). Tsander had begun to consider rocket-powered interplanetary flight as early as 1907 and was one of the founding members of the Society for the Study of Interplanetary Communication in 1924.

Tsander had begun work on the OR-1 experimental engine in 1929 while still at the IAM; this subsequently became GIRD Project 01. It ran on compressed air and gasoline and Tsander used it to investigate high-energy fuels including powdered metals mixed with gasoline. The chamber was cooled regeneratively by air entering at the nozzle end and also by water circulating through a coil.

Project 02, the OR-2 engine, was designed for Korolev's RP-1 rocket-powered glider. It burned oxygen and gasoline, and its nozzle was made of heat-resistant graphite. The engine was later modified to burn alcohol, which generated less heat than gasoline, and its thrust was increased. After cooling the engine walls, the compressed oxygen entered the top end of the chamber in a swirling pattern. Fuel was injected through an atomizer at the center, to create efficient mixing and combustion.

In January 1933 Tsander began the development of the GIRD-X missile. It was originally to use a metallic propellant, but after various metals had been tested without success it was designed without a metallic propellant, and was powered by the Project 10 engine which was first bench tested in March 1933. This design burned LOX and gasoline and was one of the first engines to be regeneratively cooled by the LOX, which flowed around the inner wall of the combustion chamber before entering it. Problems with burn-through during testing prompted a switch from gasoline to less energetic alcohol. The final missile, 2.2 *m* long by 140 *mm* in diameter, had a mass of 30 *kg* and it was anticipated that it could carry a 2 *kg* payload to an altitude of 5.5 *km* [10].

The first flight of GIRD-X (renamed GIRD-09) was on August 18th, 1933. The rocket generated a thrust of 500 *N* for 15 *sec* and reached the modest altitude of 400 *m.*

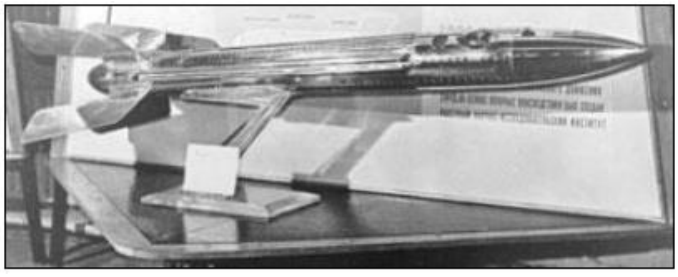

Figure 2.1: GIRD-09 model.

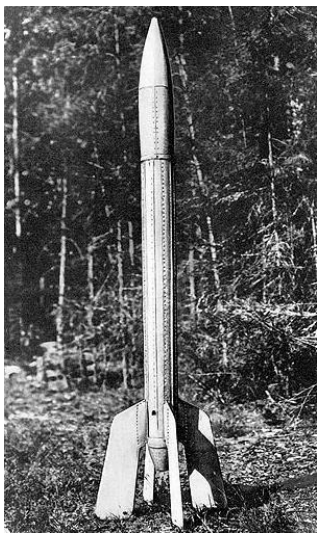

Figure 2.2: GIRD-09.

In the period 1937-1943, burning tests were conducted at I.G. Farben laboratories [9]. Based on an original idea by Leonid Andrussow, Noeggerath and Lutz performed tests on a rocket employing multi-perforated coal disks as fuel, and nitrous oxide as oxidizer. The motor could deliver 10 *kN* of thrust for a burning time of 120 s. Regression rate of this fuel/oxidizer combination shared the same unsuccessful results of experiments with LOX and graphite by Goddard. The high heat of vaporization of carbon was the main cause for the poor results achieved.

In the 1940's tests on hybrid rocket engines were conducted by the California Pacific Rocket Society. In these investigations, LOX was used as oxidizer, while several fuels such as wood, wax and rubber were considered. This group flew twenty three rockets in the period from 1947 to 1951, achieving specific impulses up to 160 s with combustion pressure up to 2.0265 *MPa* [11].

During this experimental campaign a LOX/rubber rocket reached an altitude of about 9 km in 1951 [12].

In 1946 the NASA JPL tested a solid fuel ramjet with graphite as fuel and air as oxidizer. Solid fuel ramjets follow the same internal ballistics of HREs, the main difference being the scooping of air from the atmosphere by dedicated intakes. In the frame of this research program, the first analytical model of hybrid combustion was developed by Bartel and Rannie [11].

During the '50ies, Dembrow and Pompa (General Electric, USA) tested the propellant couple made by hydrogen peroxide (H_2O_2) and polyethylene in a rod and tube grain design [12]. Dembrow and Pompa achieved a very smooth combustion produced a high combustion efficiency. Engine throttling was demonstrated during this study, though H_2O_2 thermal stability could limit the inherent safety of HREs.

In the same period, the US Applied Physics Laboratory tested the first reverse hybrid using JP as liquid fuel and different inorganic reactants as solid oxidizers [9]. Other version of the reverse HREs were separately studied at the United Technology Center –

Chemical System Division in the mid-1960's utilizing hydrazine-based liquid fuels and further solid oxidizer such as hydrazinium diperchlorate and nitronium perchlorate [9]. The solid charges of oxidizer were obtained by compression using a nonreactive fluorocarbon binder. The reverse hybrid approach was soon abandoned because of the poor combustion quality and insufficient performances enhancement that do not justify the difficulties related to charge pressing.

During the '60ies and the '70ies, a laboratory hybrid motor was developed by the UTC-CSD. It was composed of a Plexiglas fuel tube operating with gaseous oxygen as oxidizer. This device proved to be safe, inexpensive and an excellent toll for investigating interior ballistics behavior. It was used to obtain images of hybrid combustion elucidating many of its complex features.

In the same years, a requirement from Department of Defense of USA was emitted for target drones that could fly at high altitudes for a duration up to five minutes. The unit had to be launched at an altitude of about 12 km and accelerated to 30 km at Mach number values between 2 and 4. The system should have performedperform an initial boost phase followed by a low-thrust sustain phase. This operating profile highly fits to HREs.

The UTC-CSD proposed the Sandpiper rocket to satisfy this requirement. This drone was a modified Beech AQM-37A and used a storable propellant combination of MON-25 (25% NO + 75% N_2O_2) as liquid oxidizer and PMMA loaded with Mg as solid fuel.

After the Sandpiper tests were successful, the Air Force formally started the XAQM-81A HAST program to develop a production target based on the AQM-37 Sandpiper configuration.

The HAST (later renamed to HAHST) development program apparently met with some difficulties because the configuration was not finalized before the late 1970s.

Figure 2.3: XAQM-81A HAHST [13]

However, the offer for a full-scale development contract was considered too expensive, and therefore the USAF called for competitive bids for HAHST development from the industry. In December 1979, the AQM-81 contract was awarded to Teledyne Ryan's Model 305 Firebolt. The first test flight of an XAQM-81A occurred in June 1983.

The Firebolt was based on the AQM-37, but used a hybrid liquid/solid rocket propulsion system as originally demonstrated in the Sandpiper program. The engine, built by the CSD of United Technology, was throttleable between 0.53 *kN* and 5.3 *kN*. A ram air turbine, with an inlet below the center fuselage, pressurized the IRFNA oxidizer before it was delivered to the thrust chamber, and also provided electrical power for the missile. After air launch at about Mach 1.5 from an F-4 aircraft, the hybrid rocket could propel the XAQM-81A to speeds of more than Mach 4 at altitudes of 30000 *m*. The Firebolt could fly a pre-programmed course and/or respond to guidance commands from the ground. The parachute recovery system allowed either a soft landing or a mid-air retrieval.

The designation AQM-81B was allocated to a projected U.S. Navy version. This was to have support for the Navy's AN/USW-3 ITCS radar augmentation for ground tracking requirements, and a floatation gear for recovery over water. The designation AQM-81N is sometimes quoted for the Naval version, but the N suffix is unofficial.

The AQM-81 test and evaluation program was successfully completed in late 1984. However, no follow-on contract for Firebolt production was awarded, presumably because it was significantly more expensive than the simpler AQM-37 [14].

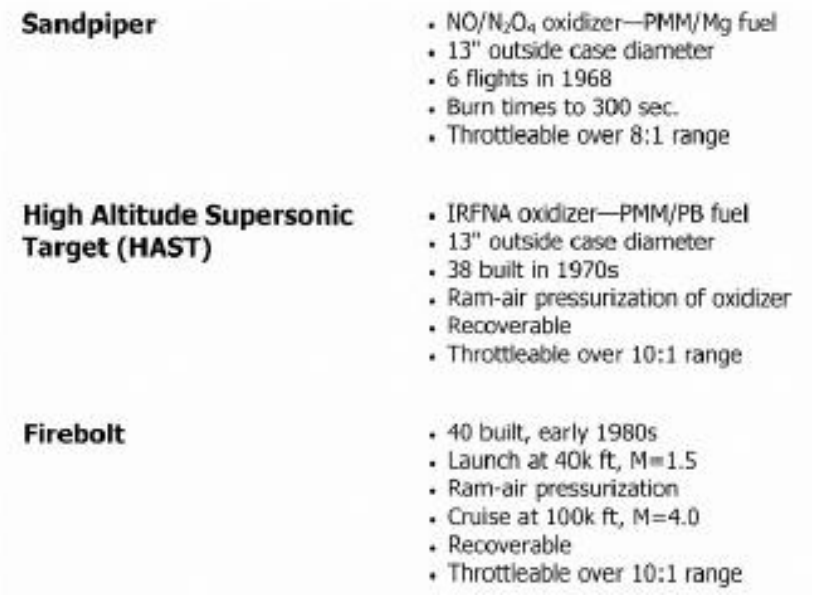

Figure 2.4: HRE–based target drones developed by UTC during the 1960s [9].

In the same period, European research activities on HREs were performed in France and Sweden. A hypergolic propellant named LEX was developed by the French agency ONERA. The LEX propellant was based on nitric acid as liquid oxidizer and diamine/nylon-metatoluene as solid fuel. The first flight of LEX took place in 1964; in

total eight successful flights were realized with this system. Altitudes above 100 km were reached. A larger scale version, the LEX-04, was tested on ground but was never flown.

The Swedish program was conducted by Volvo-Flygmotor and started in 1962. An hypergolic combination using Nitric Acid as liquid oxidizer and a polybutadiene-based solid fuel. A prototype of the Volvo designed system flew successfully in 1969, reaching an altitude of 80 km with a payload of 20 *kg.*

Interest in the HREs was revived in the late 1970's due to concern expressed for the storage and handling of the large solid propellant segments of the Shuttle booster. The storage of solid propellant grains has costly requirements due to the possible ignition and deflagration. The same safety concern arose again after the Challenger disaster in 1986, see Figure 2.5.

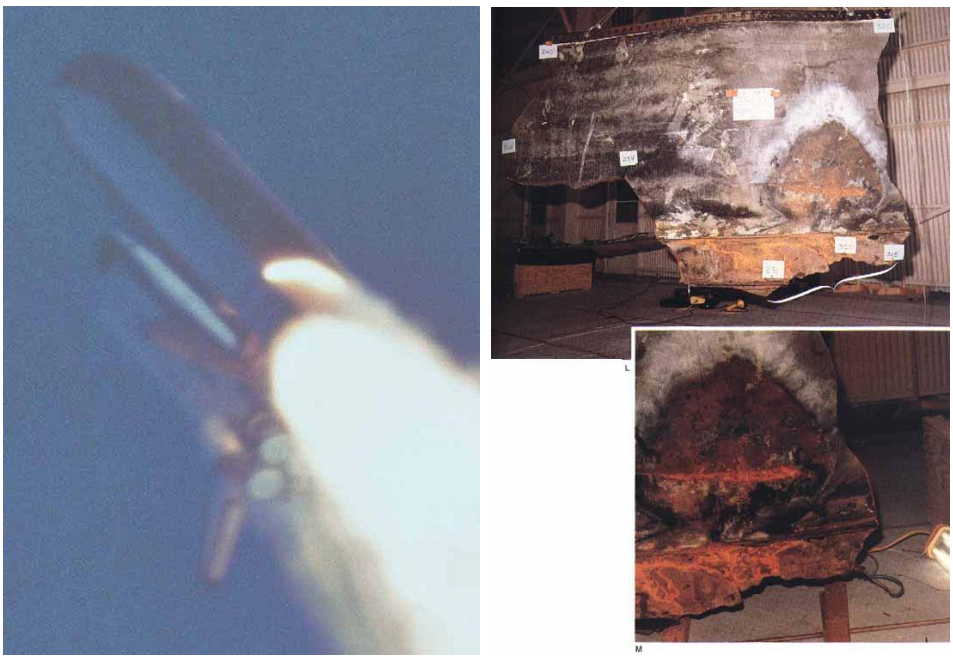

Figure 2.5: Enlarging hole of the right SSB of Challenger (left), particular of extent of burn through the right hand booster's aft field joint (right) [15]

Recent, dramatic failures of solid propellants renewed the interest on HREs also in Europe. As demonstrated by an ONERA study by Maisenneuve and Lengellé [4], the interest for HREs is not simply due to the possibility of an enhanced safety of space launch/navigation systems, but is also due to enhanced performance. In their study Maisenneuve and Lengellé evaluated the effects of a substitution of Ariane 5 solid boosters with an hybrid counterpart providing the same mission operating profile. As shown in Figure 2.6, under the constraints of identical total specific impulse and thrust duration, the hybrid LOX/HTPB boosters turns out to be more efficient in term of masses, though an increase in the cross sectional area of the system. The latter being related to the need of a larger burning area for a given thrust level in turn caused by the low regression rate of HREs.

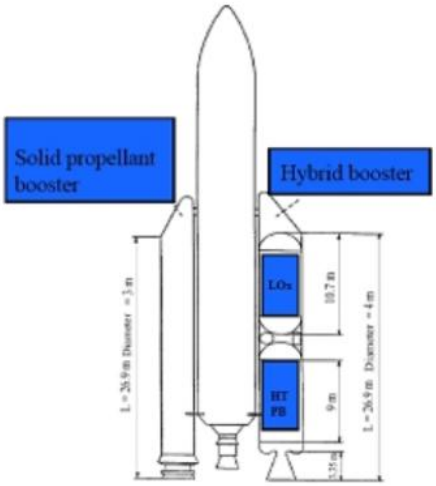

Solid-propellant booster		hybrid booster	
Solid propellant	: 237.0 t	HTPB	: 65.1 t
		Oxidizer	: 144.9 t
		Other	: 9.0 t
Structure	: 19.5 t	Structure	: 18.0 t
Insulation	: 4.7 t	Insulation	: 1.0 t
Nozzle	: 6.1 t	Nozzle	: 6.1 t
Igniter	: 0.3 t	Turbopump	: 0.5 t
Structural mass	: 30.6 t	Structural mass	: 25.6 t
Total mass	: 267.6 t	Total mass	: 244.6 t

Figure 2.6: Comparison between Ariane 5 solid propellant boosters and the possible hybrid counterpart [3].

More recently, two significant hybrid efforts occurred: the formation of the AMROC, and the HPIAG.

The AMROC is an industrial company devoted to the development of large hybrid engine. While the HPIAG was a consortium of system and propulsion companies studying HREs for the Space Shuttle booster and other launch system applications.

Due to the low regression rate of the considered fuel formulations (LOX/HTPB), both programs encountered technical problems for high thrust generation. The resulting designs had multi-perforated grains with port geometries requiring large cross sections due to the lower volumetric efficiencies.

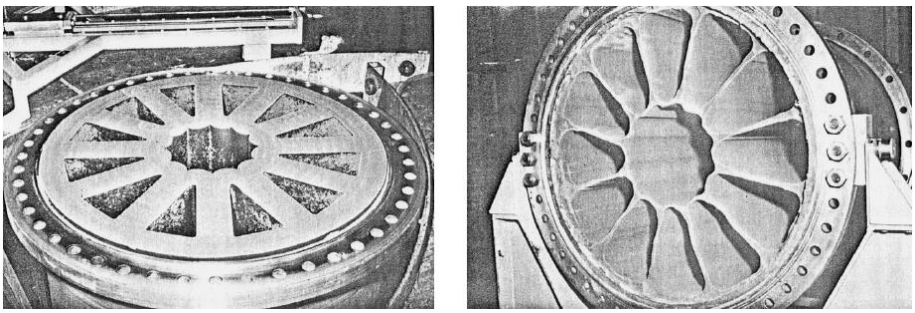

Figure 2.7: UTC wagon wheel solid fuel grain (based on PB loaded with aluminum) delivering 180 kN thrust before (left) and after firing (right) [9].

Although AMROC successfully tested small and sub-scale systems, difficulties were encountered when the engine was scaled up to 1.11 *MN* thrust. The low regression rate

of the fuel dictated a 15 port grain design. This configuration, though performing in terms of achieved thrust level, has possible weak points in solid grain mechanical properties and integrity during combustion.

Figure 2.8: Test of AMROC H–500 motor, using LOX/HTPB propellant [5].

Several hybrid propulsion programs were initiated in the late 80's and early 90's. The JIRAD program involved the testing of 11 and 24 inch diameter hybrid motors at the NASA Marshall Space Flight Center. Another hybrid program initiated during the early 90's was DARPA's HyTOP. The goal of this program was to develop the HyFlyer launch vehicle and demonstrate the feasibility of hybrid boosters for space applications. The members of the HyTOP team were AMROC, Martin Marietta and CSD/UTC. The HPDP began in March 1995. The goal of the HPDP was to enhance HREs performance and to demonstrate several critical technologies which are essential for the full-scale development of hybrid rocket boosters for space launch applications. The government and industry participants in the program were NASA, DARPA, Lockheed Martin, CSD/UTC, Thiokol, Rocketdyne, Allied Signal and Environmental Aeroscience Corporation. Even though the tasks of the HPDP program included systems studies and subscale testing, the main objective of the program was the design and fabrication of a 1.11 *MN* thrust test-bed. The design of the motor was guided by the subscale motor tests performed under the JIRAD program.

The latter has a wagon wheel solid grain configuration with 7 burning ports with a single central port lodging fuel web support (Figure 2.9) and was made of conventional hydroxyl-terminatedpolybutadiene (HTPB)/ Escorez fuel.

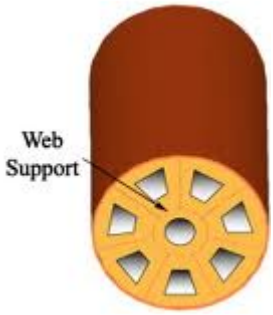

Figure 2.9: High burning multiport surface geometry

The 1.11 *MN* thrust test-bed motor was fired for short times in July 1999. It exhibited large pressure oscillations and anisotropic burning rates in the various ports. Problems related to low regression rate inherent in conventional hybrids fuels were not solved.

The most recent advance in hybrid rockets occurred in the Fall of 2004 when the Space Ship One carried flew to over 117000 *m* and won the Ansari X-prize, a space competition in which the X-Prize Foundation offered a US$10,000,000 prize for the first non-government organization to launch a reusable manned spacecraft into space twice within two weeks. The competition goal was adopted from the SpaceCub project, demonstration of a private vehicle capable of flying a pilot to the edge of space, defined as 100 km altitude. This goal was selected to help encourage the space industry in the private sector, which is why the entries were not allowed to have any government funding. It aimed to demonstrate that spaceflight can be affordable and accessible to corporations and civilians, opening the door to commercial spaceflight and space tourism.

This privately funded, sub-orbital flight ushered in a new era in space tourism.

Figure 2.10: Space Ship One carried aloft by the White Knight [Credit: Scaled Composites, LLC].

The propulsion system used for this project used a HTPB-based solid fuel grain with four ports, with nitrous oxide (N_2O) as the oxidizer. Combustion of the HTPB grain produced strong vibrations on the SpaceShipOne structure, as reported by the pilot Brian Binnie after landing [16].

Figure 2.11: Various systems of Space Ship One [Credit: Scaled Composites, LLC].

Nowadays several research groups all over the world are active in hybrid propulsion study. Development activities are mainly carried out in USA, but contribution are found from Canada, India, Korea, Russia and Europe too.

In Italy several teams are interested in studies on hybrid motor fluid-dynamic modeling, testing of new HEDMs and solving problems connected to the project of large motors. Research teams are mainly associated to the University of Naples [17], [18], [19], University of Padova [20], [21], [22], Politecnico di Torino [23], [24] and Politecnico di Milano(SPLab) [25], [26], [27], [28], [29], [30], [31]. SPLab provides contribution to several international programs since '70ies.

2.2. Fundamentals of Hybrid Propulsion

Active sponsorship of basic studies began in about 1960, largely in the US and to a lesser extent in France, Germany, and Sweden. At least six organizations entered the field in the U.S. In a series of basic contracts originally sponsored by the Navy, UTC conducted a group of fundamental investigations on the combustion behavior and internal ballistics in hybrid motors.

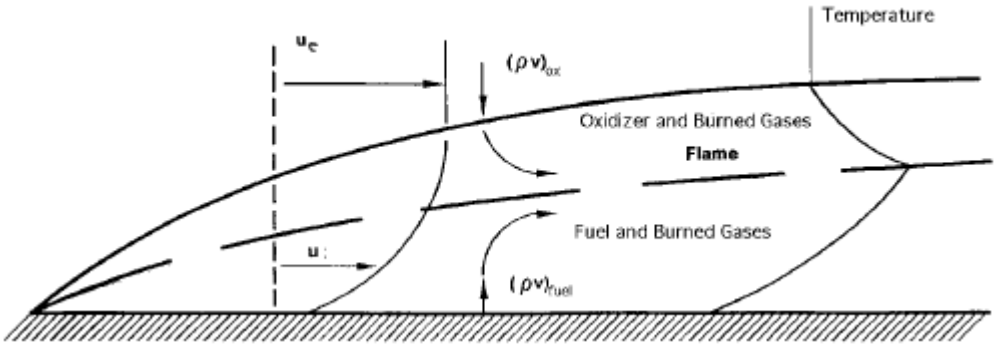

Figure 2.12: Regression rate model derived from the Schlieren photograph.

In hybrid rockets a diffusion flame is established in the boundary layer [12]. The reaction zone is characterized by a finite thickness (Figure 2.12) whose boundaries depend on propellant mixture flammability limits. The heat feedback, both convective and radiative, from the reaction zone to the fuel grain induces pyrolysis of the solid fuel surface, thus sustaining the process together with a continue oxidizer flow.

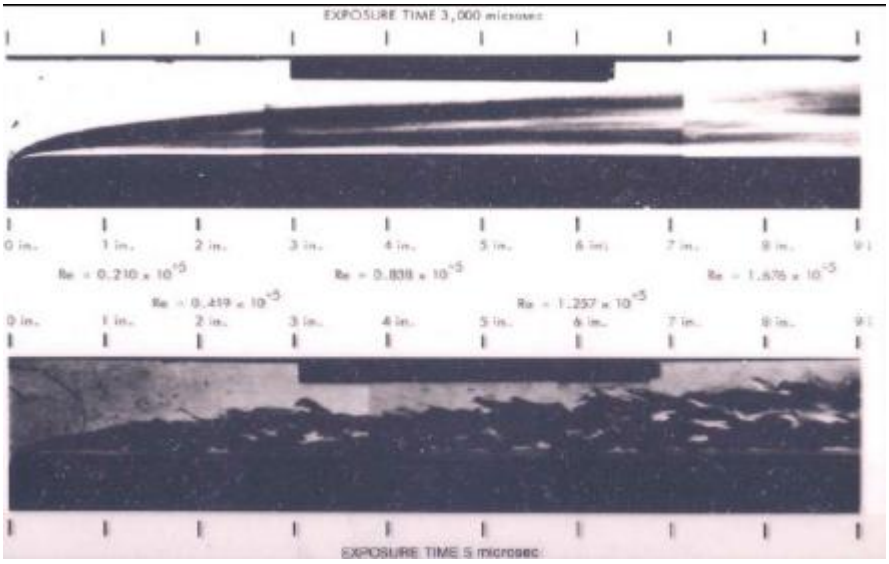

Figure 2.13: Schlieren visualization of Plexiglas combustion in GOX. Reacting boundary layer developing over the fuel slab [12].

The heat transfer limited model, based on a idealized turbulent boundary layer combustion, was proposed by Marxman and Gilbert [32] in 1963. Basic hypotheses of this model include the presence of a relatively thin flame zone within the boundary layer inducing surface pyrolysis. Combustion occurs between fuel vapors and oxidizer mutually diffusing one into the other. The reacting boundary layer and the heat transfer between the flame and the regressing surface is affected by the mass addition from the

solid fuel grain (the so called blowing). The hybrid fuel combustion is characterized by a macroscopic diffusive flame theoretically placed in the boundary layer where the stechiometric O/F ratio is achieved. The temperature presents its maximum value at the flame, while the velocity grows monotonically from the wall to the free-stream one.

The flow is easily transferred from laminar flow to turbulent flow because of the reaction in the boundary layer flame zone and the mass addition from the solid surface, or blowing . Therefore, the hybrid boundary layer was treated as turbulent over the entire length.

Marxman and Gilbert model considers, as starting point, the convective energy balance at the regression surface yields, under steady conditions. The radiation term and the conduction depth in the solid are not considered:

$$\dot{q}_s = \rho_f r_f h_f = h\Delta T \tag{2.1}$$

Where ρ_f, r_f and h_f are respectively the density, the regression rate and the gasification enthalpy of the solid fuel, while $h\Delta T$ is the thermal flux in the boundary layer evaluated at the gas phase side of the surface. The Reynolds analogy, in this case, states that the heat exchange coefficient at the surface, evaluated as Stanton number C_h, is connected to the surface friction factor coefficient C_f by means of the Prandtl number P_r. In this way, an expression for the fuel regression rate can be defined:

$$r_f = \frac{C_f}{2}\frac{\Delta h}{h_f}\frac{\rho_e u_e}{\rho_f} P_r^{-\frac{2}{3}} \tag{2.2}$$

In the above expression, due to the mass addition from the solid grain surface, actually a boundary layer subjected to blowing due to the transversal mass injection has to be considered. All the relevant parameters have to be properly evaluated to take into account the blockage effect yielding a reduction of the surface friction coefficient and the heat exchange coefficient due to the blowing phenomenon itself. In absence of radiation, for traditional hybrid engines, the non dimensional blowing parameter B can be approximated as:

$$B = \frac{\Delta h_f}{h_f} = \left(\frac{f}{f^*}\right)^{-1.47} \tag{2.3}$$

In a turbulent boundary layer, it is commonly accepted that $P_r \approx 1$, leading to an expression for the solid fuel regression rate:

$$r_f = C_1 \left(\frac{\mu}{x}\right)^{0.2} \frac{\left[G_{ox} + G_f(x)\right]^{0.8}}{\rho_f} B^{0.32} \quad \textbf{(2.4)}$$

The lack of an explicit dependence on pressure should be underlined.

In general, a simplified form of Marxman's diffusion controlled regression rate (Eq. (2.4)) is widely used:

$$r_f = a_r G_{ox}^{n_r} \quad \textbf{(2.5)}$$

In the first model, Marxman and coworkers did not take into account the effect of radiation. However, in case of metalized and hydrocarbon rich formulations the heat exchange by radiation is important. Moreover radiative heat transfer is independent on the blowing effect, but the presence of its associated regression rate hinders the convective exchange. The convection-radiation coupling was later studied by Marxman yielding an empirical formula for the regression rate [33]:

$$r_f = r_{f,c}(0.37 \frac{\dot{q}_{rad}}{\dot{q}_c}) \quad \textbf{(2.6)}$$

2.3. Performance Enhancement

The two main unsolved, but somewhat unique, technical performance-degrading problem of hybrid rockets are the low overall combustion efficiencies and slow regression rate.

The regression rate increase of the solid fuel can be achieved either by fluid mechanical or chemical approaches.

Fluid dynamic methods use devices to enhance turbulence levels at the combustion surface. As a consequence the corresponding heat exchange coefficient is increased. Due to the higher heat feedback from the flame, the regression rate can be increased. A turbulence generator can be achieved inserting screens of metallic wires in the solid grain. A similar result can be obtained using chemical additives that easily sublimates

during the combustion, thus making the exposed surface sufficiently rough. Another possibility is to generate vortexes in the perforations of the solid grain by an oxidizer tangential injection, also called swirl injection [34], or driving the flow by a helical grain configurations [35].

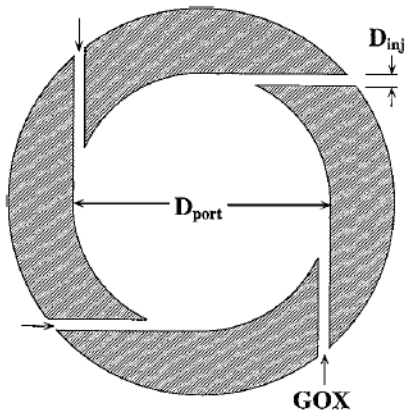

Figure 2.14: Typical Swirl Injector [36].

The helical grain configuration reduces the charging volume due to the tracks into the fuel by 1~2% but increases dramatically the regression rate without resort to any additional device [35].

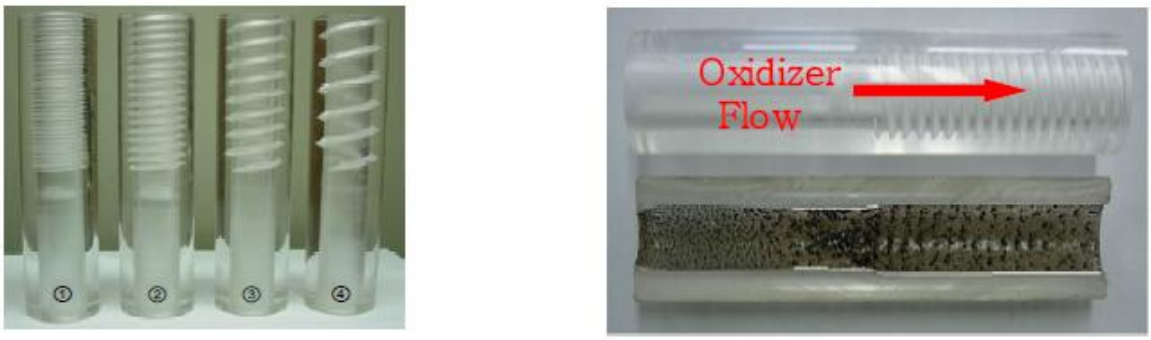

Figure 2.15: Different grain configurations and Sample cross section.

Although regression rate could be increased up to four times by means of fluid dynamics methods, the application to large-size engines and the capability to maintain a sufficient vortex intensity during combustion for geometries of practical interest is an intrinsic difficulty of this technique.

Another possibility is the use of entrainment fuels, like cryogenic materials or paraffin-based fuel [37]. During the combustion, these substances create a low viscosity, thin, fluid layer that allows the gaseous stream to capture fuel droplets from the fuel surface.

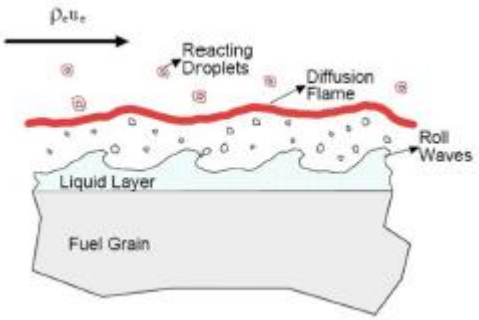

Figure 2.16: Entrainment of melted fuel droplets from surface melted layer of fuel grain by oxidizer flow [37].

This behavior reduces the value of the blowing coefficient and also the heat needed in the combustion process because the droplets absorb only the heat of fusion. However this heat has to be absorbed before the droplets leave the combustion chamber in order to start the burning process. Otherwise, no chemical reaction could occur and no heat release could be achieved from droplet combustion. So, the main problem connected to this technique is that the droplets have to react completely into the engine to maintain unaltered the rocket theoretical performances. This imposed the presence of a post-combustion chamber.

In the '60ies, attempts made in order to increase solid fuel regression rate have been conducted introducing energetic additives into the grain. Chemical additives, like oxidizers (NH_4ClO_4 e NH_4NO_3), work to decrease the solid fuel effective gasification enthalpy by means of exothermic reactions on the regressing surface. Problems connected to this technique can be for the use of oxidizer, the reduction of the safety and the possibility of re-ignition in case of desired extinction. A second solution is to dope fuel with energetic materials, for example metal powders. Different studies have been made on metal powders, especially Aluminum, loaded fuel or propellants [38] [39]. The idea is to augment the heat release near or at the regressing surface, increasing the heat feedback and thus the regression rate of solid grain. In case of addiction of metal powders one of the most important parameter is combustion heat release.

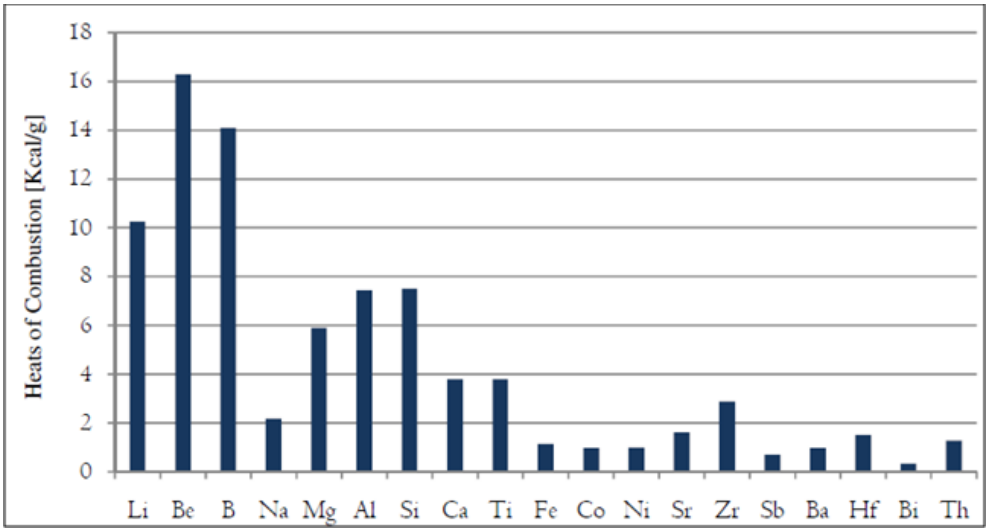

Figure 2.17: Heats of Combustion for different metal species [40].

Beryllium is the most energetic material, but unfortunately is toxic, Boron is difficult to ignite and can be added only coupled with a reactive material like Magnesium. Nowadays in SPLab are in progress different studies on this topic. Lithium could be a good choice, from an energetic point of view, but is pyrophoric. The only material that is in the same time: energetic, easy to find and cheap is Aluminum. For this reason is the most used metal in Hybrid and Solid boosters. The three main advantages in using metal powders are: higher heat release due to oxidation of metal, higher radiation heat exchange (that is more efficient than convective one because of blowing) and increase of volumetric specific impulse. Another important effect that can be achieved only with some types of particles, for example μAl, is dumping of possible high-frequency instabilities [5]. On the other hand, introduction of metal creates condensed combustion products [41] that reduce theoretical increases in I_s.

3. Solid Fuel Formulations

This work is focused on Hybrid solid fuel formulation HTPB based. 13 different types of fuels have been tested:

- HTPB + 10% ALEX™
- HTPB + 10% ALEX™ + Fluorel™ + Telomer n5
- HTPB + 10% Al85-Cu15
- HTPB + 10% Al85-Cu15 + Fluorel™ + Telomer n5
- HTPB + 10% Al74-Cu26
- HTPB + 10% Al74-Cu26 + Fluorel™ + Telomer n5
- HTPB + 10% Al47-Cu53
- HTPB + 10% Al47-Cu53 + Fluorel™ + Telomer n5
- HTPB + 10% Al32-Cu68
- HTPB + 10% Al32-Cu68 + Fluorel™ + Telomer n5
- HTPB + 10% Al15-Cu85
- HTPB + 10% Al15-Cu85 + Fluorel™ + Telomer n5
- HTPB + 10% Cu

All Burning test have been performed in Gox.

3.1. Baseline (Cured HTPB)

Binder is made by HTPB-R45 (>79%), a plasticizer and a curing agent. This is important to lend it solidity and good mechanical proprieties.

3.1.1. Hydroxyl Terminated Polybutadiene

Hydroxyl terminated Polybutadiene (HTPB) is an organic compound produced at first in '60s. Nowadays is the most used binder in solid propulsion and fuel in hybrid one [42].

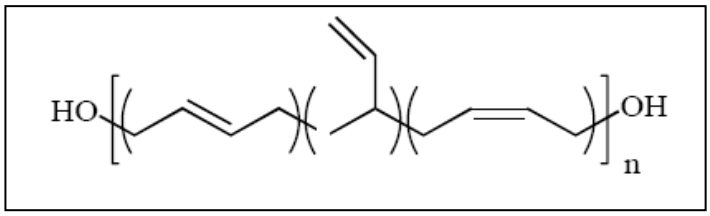

Figure 3.1: HTPB-R45 chemical structure [42].

Moreover HTPB is inert; it can improve safety during manufacturing processes. The particular type of HTPB used in SPLab is HTPB-R45.

It is characterized by a chain of 45 butadiene monomers $C_4 H_6$ [43] .

At ambient temperature HTPB is a viscous, non Newtonian, amber colored liquid.

Table 3.1: Physical and chemical properties of HTPB-R45.

Physical State at ambient conditions	High viscosity amber color liquid
Molecular weight [*g/mol*]	2800
Density [kg/m^3]	901
Combustion Heat [*kJ/kg*]	4180

3.1.2. Plasticizer: Dioctyl Adipate

It is commonly used to add a plasticizer to the Binder, in this case Dyoctil Adipate (DOA $C_{22}H_{42}O_4$).

DOA can increase mechanical proprieties of HTPB during manufacturing process. In particular it is used to reduce binder viscosity.

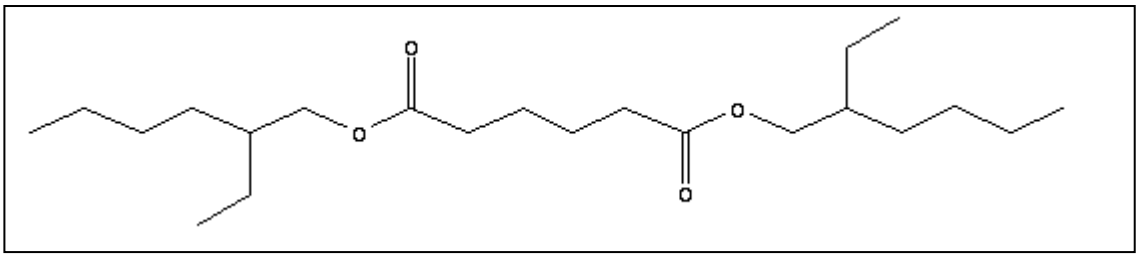

Figure 3.2: Diocityl Adipate chemical structure.

Even a small quantity of this chemical affects the production of binder. DOA used for all the sample presents physical – chemical properties shown in Table 3.2.

Table 3.2: Physical and chemical properties of DOA.

Physical State at ambient conditions	Uncolored Liquid
Molecular weight [*g/mol*]	370.58
Density [kg/m^3]	920
Melting Temperature [K]	206
Flash point Temperature [K]	454
Auto Ignition Temperature [K]	668

3.1.3. Curing Agent: Isophorone Di-Isocyanate

The Isophorone Di-Isocyanate (IPDI, $C_{12}N_{18}H_2O_2$) create permanent cross links between HTPB molecules. Thanks to IPDI, Binder is solid in ambient conditions.

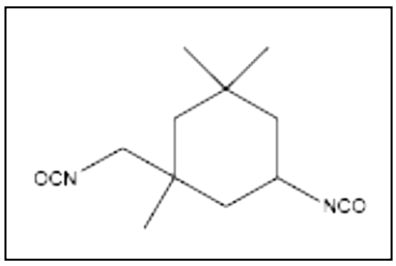

Figure 3.3: IPDI chemical structure.

IPDI is a volatile compound, and it is highly toxic because of isocynate groups.

Table 3.3: Physical and chemical properties of IPDI.

Physical State at ambient conditions	Uncolored Liquid
Molecular weight [*g/mol*]	222.29
Density [kg/m^3]	1061
Melting Temperature [K]	213
Flash point Temperature [K]	428
Auto Ignition Temperature [K]	703

The mechanical proprieties of the binder are strictly connected to the curing level that represents –*NCO* and -*OH* groups ratio [42].

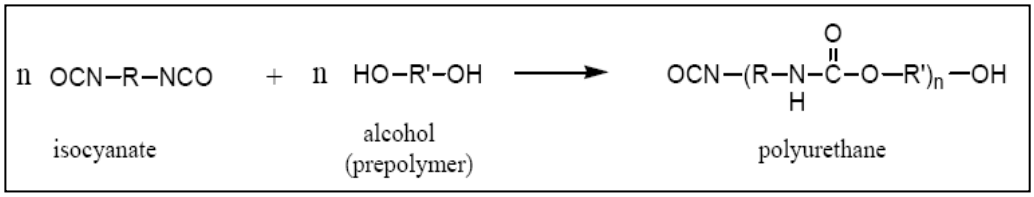

Figure 3.4: Chemical scheme of polyurethane synthesis between HTPB and IPDI.

3.1.4. Curing Catalyst : Dibutylin Diacetate

Dybutylin Diacetate *$((CH_3CO_2)_2Sn[(CH_2)_3CH_3]_2)$* is the curing catalyst and it is used to lower the activation energy of the curing reaction itself. The effect connected to the addition of TIN is an acceleration in the reticulation processes of HTPB.

A minimum concentration of 0.43% in mass is needed to increase sensibly curing reaction speed. In this condition reduction in terms of curing time are big, from about 1 week at 60°*C* without TIN to 25 hours at 36°*C*.

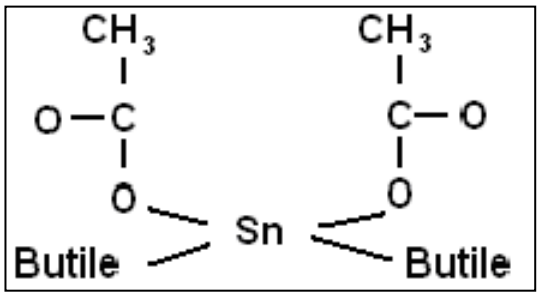

Figure 3.5: TIN chemical structure.

Table 3.4: Physical and chemical properties of TIN.

Physical State at ambient conditions	Uncolored Liquid
Molecular weight [*g/mol*]	351.01
Density [*kg/m³*]	1321
Boiling Temperature [*K*]	415

3.2. Energetic Additives

A simple way tested to increase hybrid solid fuel regression rate is the introduction of energetic materials into the binder inert matrix [44]. Among these additives, metals are largely used, either of micrometric and nanometric size [41].

This work is focused on the ballistic analysis of Aluminum and Copper loaded fuels. All particles have nanometricasize.

Production of bimetallic nano-powders with EEW (Electric Explosion of Wires) method, changes proprieties of the two materials creating intermetallic compounds [6].

This topic will be deeper analyzed in the following chapter.

3.2.1. Aluminum

Aluminum is a silvery white member of the 13rd group of the chemical elements table [45]. Its atomic number is *13*, molecular weight is *26.98 g/mol* and density is *2700 kg/m³.* It is a soft, durable, lightweight, ductile and malleable metal with appearance ranging from silvery to dull gray, depending on the surface roughness. Its melting point is *933 K*. Corrosion resistance can be excellent due to a thin surface layer of aluminum oxide that forms when the metal is exposed to air, effectively preventing further oxidation. Native aluminum atoms are arranged in a face-centered cubic structure. Powders of native aluminum have reducing capacity and in basic water react producing hydrogen. However Aluminum is commonly covered by oxide because is very chemically reactive.

The most common Aluminum oxidation state is *+3,* however compounds with lower oxidation states are known. Stable Aluminum oxide is Al_2O_3. This compound is allotropic and the most common form is the α-oxide.

Heat formation Δh_f of Alumina is considerably negative indicating the great stability of the compound itself.

$$2Al + \frac{3}{2}O_2 \rightarrow Al_2O_3 \qquad \Delta h_f = -1676\ kJ/mol \tag{3.1}$$

Aluminum has high combustion enthalpy. For this reason it is widely used in propellants, pyrotechnics, and explosives. In this work nanometric powders produced by EEW method have been used [46] [47].

Table 3.5: Physical and chemical properties of Aluminum [48].

Physical state in ambient conditions	Solid grey
Molecular weight [*g/mol*]	26.981
Density [kg/m^3]	2700
Melting Point [*K*]	933
Boiling Point [*K*]	2792
Oxide Melting Point [*K*]	2345
Solid Oxide formation Heat [*kJ/mol*]	-1670

3.2.2. Copper

Copper is a member of the 11rd group of the chemical elements table [45]. Its atomic number is *29*, molecular weight is *63.54 g/mol* and density is about *8920* kg/m^3.

It is a ductile metal with very high thermal and electrical conductivity. Pure copper is soft and malleable. A freshly exposed surface has a reddish-orange color. It is used as a conductor of heat and electricity, a building material, and a constituent of various metal alloys. Its melting point is *1357.37 K*.

Copper forms a rich variety of compounds with oxidation states +1 and +2, which are often called cuprous and cupric, respectively.

It does not react with water, but it slowly reacts with atmospheric oxygen forming a layer of brown-black copper oxide. This layer stops the further bulk corrosion.

Cupric oxide (CuO) is the higher oxide of copper. It is a black solid with an ionic structure which melts above 1500 *K*. It can be formed by heating copper in air:

$$\frac{1}{2}Cu + \frac{1}{2}O_2 \rightarrow CuO \qquad \Delta h_f = -156\ kJ/mol \tag{3.2}$$

In these condition cuprous oxides (Cu_2O) is formed as well:

$$2Cu + \frac{1}{2}O_2 \rightarrow Cu_2O \qquad \Delta h_f = -170\ kJ/mol \tag{3.3}$$

In moist air cuprous oxide degrades in cupric oxide [49].

Formation of oxide from Copper is much less energetic than for aluminum, as testified by relative Δh_f.

Using copper inside Hybrid motors has a double aim. At first, during EEW production of Aluminum and Copper bimetallic ultra disperse powders, intemetallic compounds can be generated [6], [7].

Intermetallic compounds can be completely different from the original metals in terms of proprieties, structure and combustion behavior.

Moreover copper has a lower ignition temperature than aluminum (Chapter 3). Copper oxidation could favor ignition of Aluminum that is difficult because of the high melting temperature of Alumina.

Table 3.6: Physical and chemical properties of Copper [48].

Physical state in ambient conditions	Solid
Molecular weight [*g/mol*]	63.54
Density [kg/m^3]	8920
Melting Point [*K*]	1358
Boiling Point [*K*]	2843
Cuprous oxide Melting Point [*K*]	1517
Cuprous oxide formation Heat [*kJ/mol*]	-170.71
Cupric oxide Melting Point [*K*]	1599
Cupric oxide formation Heat [*kJ/mol*]	-156.06

4. Powders Production and Characterization

This chapter is focused on the description of EEW nanopowders production and characterization. The hardware for nano-sized powders production is hereby discussed. Analyses of the pre-burning characteristics of the powders was performed by TEM, DSC/TGA, particle size distribution.

In the present study Al and composite Al-Cu nano-sized powders are investigated. All of the produced powders were passivated in air [50]. Simply air-passivated and air-passivated and coated variants of the produced powders were investigated (Table 4.1). The aim of the investigation was the evaluation of the effects of fluorohydrocarbon coating on powders characteristics [50] [51] [52] .

All the presented metallic powders were produced and then characterized at the *Institute of Strength Physics and Materials Science SB RAS, pr. Akademicheskii 2, Tomsk, 634021 Russia* and the *Department of Technical Physics of Tomsk State University, 36 Lenin Prospekt, Tomsk, 634050, Russia* thanks to the cooperation of their stuffs.

Table 4.1: Tested powders types.

Powder Name	% Al	% Cu	Passivation in air	Coating
ALEX™	100	-	Yes	No
ALEX™ Coated	100	-	Yes	Yes
Al85-Cu15	85	15	Yes	No
Al85-Cu15 Coated	85	15	Yes	Yes
Al74-Cu26	74	26	Yes	No
Al74-Cu26 Coated	74	26	Yes	Yes
Al47-Cu53	47	53	Yes	No
Al47-Cu53 Coated	47	53	Yes	Yes
Al32-Cu68	32	68	Yes	No
Al32-Cu68 Coated	32	68	Yes	Yes
Al15-Cu85	15	85	Yes	No
Al15-Cu85 Coated	15	85	Yes	Yes
Cu	-	100	Yes	No

4.1. Nanopowders Production: the EEW Method

The nano-sized powders characterized in this study were produced by EEW technique. The EEW process provides high yield of the production of the nanopowders (~100 g/hour) thus enabling industrial-level production of nano-sized metals [53]. This technique was originally used by Russian researchers. Focus of this discussion will be on nano-sized Al, and Al-Cu prodcution.

The machine used for the production of Al and Al-Cu nanopowders is the UDP-5 [54]. The latter is an evolution of the UDP-4. Improvements of the updated hardware aim at improving the gas dynamics of exploded particles during their flow toward the machine powder collector. The design of UDP-5 lessens the possible sintering/clustering of nano-particles in the powder collector due to their interaction during following explosions. Electrical scheme and parameters for EEW powder production are the same for UDP-5 as for previous version of the facility.

The EEW process is based on the electric circuit scheme shown in Figure 4.1. The electric wire is placed in a controlled atmosphere of Ar or N_2.

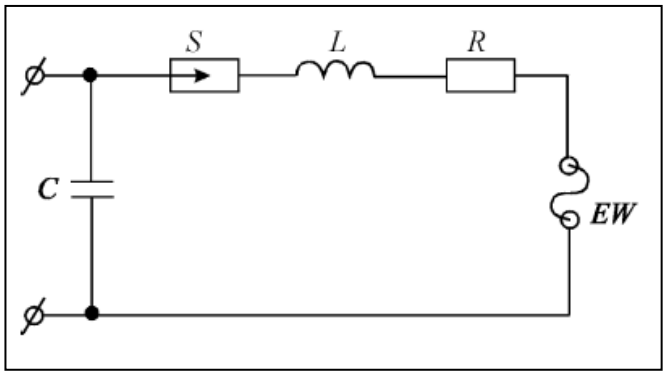

Figure 4.1: Machine simplified electrical scheme [53].

At the beginning of the process, the switch S is open, while the capacitor C is charged. Then S is closed, C is discharged and therefore an electrical current starts to circulate into the circuit connected to the EW. Discharge of he capacitor takes 1-5 *μs*. In this process, the temperature of the EW increases because of Joule effect. The heating phase has high rates (in the order of 10^9 *°C/s*. Due to the incoming power the metal EW reaches its sublimation temperature. Then the EW explodes (see Figure 4.2), pressure in

the explosion chamber of UDP-5 reaches pressures up to ~10^3 MPa. Exploded particles speed ranges from 1 to 5 km/s under EEW procedure. This generates shockwaves that can damage machine wire support, as shown in Figure 4.3. After the explosion the vaporized metal suddenly re-condenses as ultradisperse particles with 10-200 nm diameter size. The nano-sized Al tends to oxidize (at worst to self-ignite) when exposed to air/atmospheric humidity or other oxidizing environment. In order to avoid /limit this, a passivation process is required. Immediately after production, powders produced by EEW are passivated in a slow, dry gaseous stream of Ar + 0.1% Air (by mass) or by immersion in a proper fatty-acid solution [50]. When passivated in air, *nAl* particles are covered by a thin alumina (Al_2O_3) shell protecting the Al core from further oxidation. After passivation a coating can be applied to the tested powders. The coating can be chosen in order to reduce aging of the powders or to enhance the performance of the composition nanopowders will be loaded in [55].

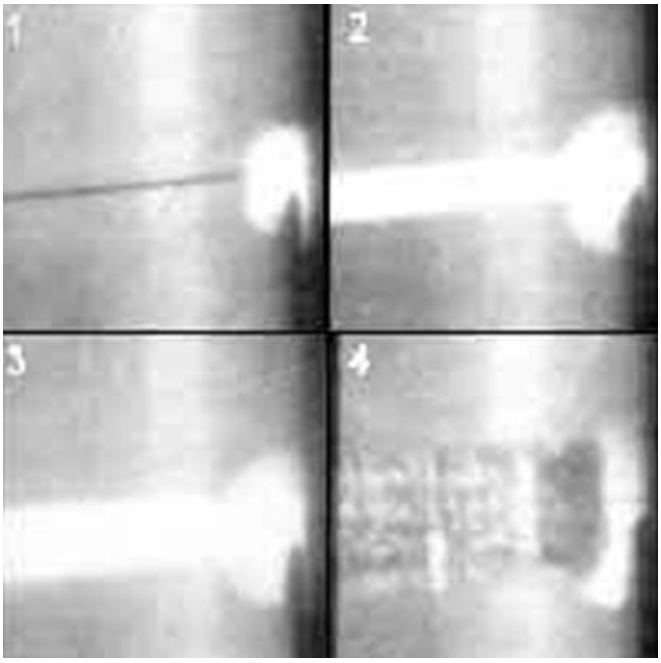

Figure 4.2: Electric wire explosion due to Joule heating in a EEW machine.

Figure 4.3: UDP-5 wire support broken by shockwaves generated by wire explosion.

Aluminum particles produced by EEW generally exhibit spherical shape [56], as seen in Figure 4.4. Particle size distribution can be partially controlled acting on the wire initial characteristics and the electrical parameters leading to wire explosion [46]. During the explosion phase, sintering of particles is likely. An example of the sintering/clustering of particles is shown in Figure 4.4. The passivation layer of nano-sized powders enhance their resistance to oxidation under standard room and temperature, though a detailed study of nano-sized particles ageing is still needed [8]. In spite of this, the passivation in air is not enough to prevent nano-sized particles from heating in presence of an external source. This is due to the relatively high alumina conductivity [50].

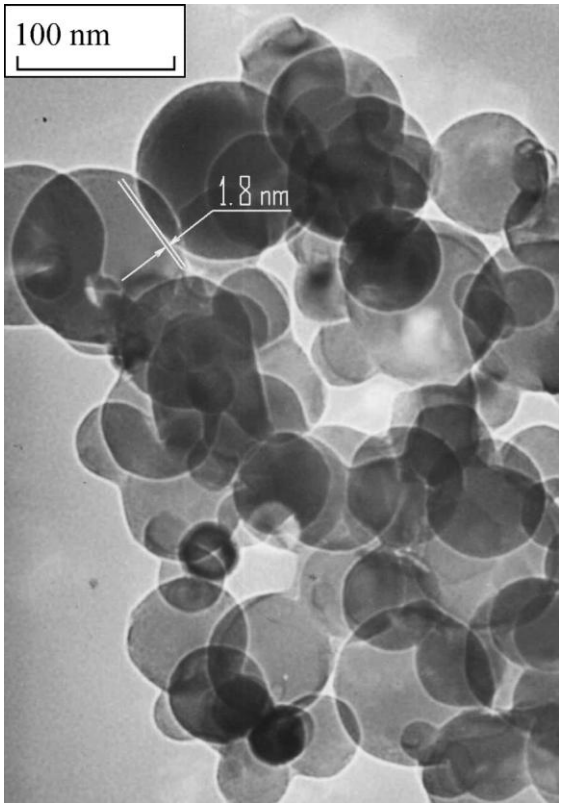

Figure 4.4: TEM images of Aluminum nanopowders [56].

The characteristics of the powders, including their particle size distribution, depend on explosion process parameters. A crucial role is played by the electrical parameters of the UDP-5 circuit [46] [50] [53]. The electrical parameters of interest include: the energy consumed by wire before explosion, energy of arc stage, and the velocity of energy input (or power density). The metal wire and its geometry (length and diameter), as well explosion chamber conditions (pressure and gaseous medium), influence the properties of nanopowders [46] [47].

An important advantage of EEW technology is the control of EEW products properties by means of electrical parameters.

The EEW production method has a low energy consumption (< 10 *kWh/kg*) because it is based on direct heating of wire by electric current, and because of the high heating rates (> 10^7 *K/s*) providing adiabatic conditions of energy transmission to the wire.

The EEW process can be performed in inert gases or active media as hydrogen. This technique enables the production of powders of metals, alloys, and intermetallic compounds. In this work an Argon atmosphere was used in the production phase.

The principal scheme of the experimental installation for producing powders by EEW method is shown in Figure 4.7.

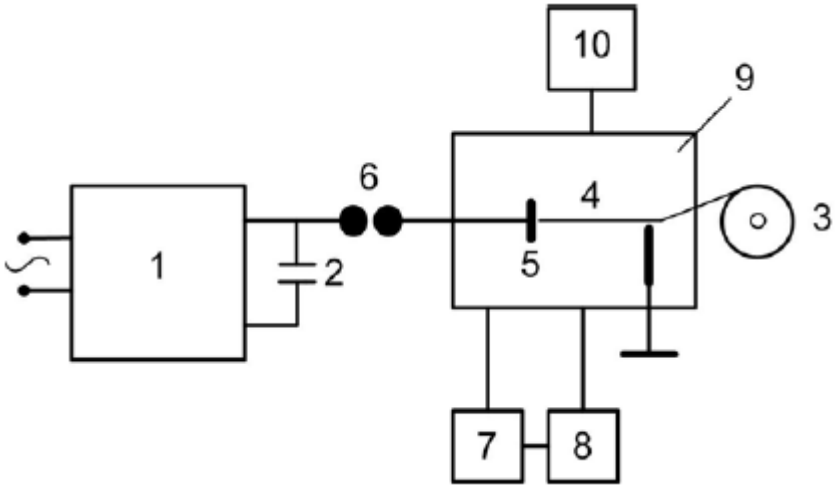

Figure 4.5: Principle Scheme of Experimental Setup [57].

The installation works as hereby reported. An high-voltage power source **(1)** charges the capacitor battery **(2)**. The wire driving mechanism **(3)** is used for automatic feed of the exploding length of wire **(4)** in the electrodes gap.

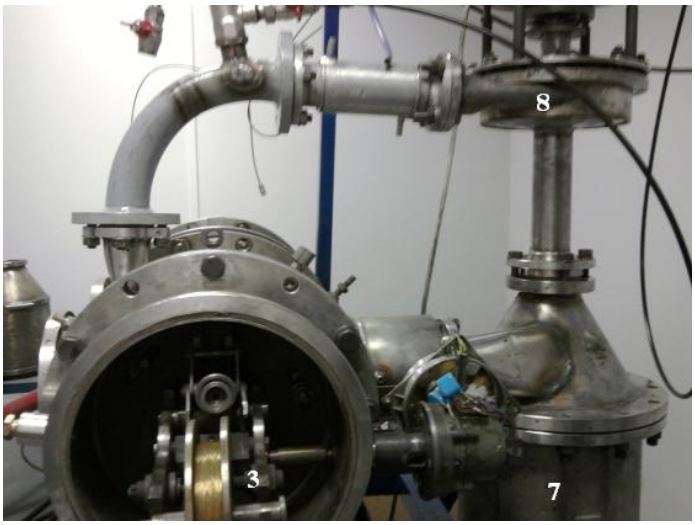

Figure 4.6: EEW Machinery; driving mechanism (3), powder collector (7), ventilator (8).

When the wire reaches the high-voltage electrode **(5)**, the commutator **(6)** operates, thus the capacitor battery discharges on this length of wire and explosion takes place. Obtained powder is collected in the powder collector **(7)** through a filter (Figure 4.7). Gas refined from powder is given back in the explosive chamber **(9)** by means of the

ventilator **(8)**. The explosive chamber is vacuumed before working, and then the chamber is filled with working gas atmosphere by means of system **(10)**.

Figure 4.7: Cone shaped filter.

When the EEW process terminates, the powder collector is separated from the machine and covered with a synthetic cap. The following passivation phase takes 3-4 days [50]. For the powders considered in this work, passivation was performed in a slow dry gaseous stream of (Ar + Air).

The bigger clusters can be broken by inserting the collector in a low frequency vibrating machine (~200 *Hz*) for 20 minutes. After this, powder is manually filtered with metal sieves and packaged into a double layer plastic container.

4.2. Powder Production

Production of composite powders is based on the use of two metal wires exploding together in the same chamber and atmosphere.

4.2.1 Wires Productions

In order to arrange a good set of powder formulations with a wide range of Aluminum-Copper concentrations, different wire diameters were used. Relative dimensions of wires and resulting exploding wire dimension influence the particle-size distribution of powders [46]. Metal wire diameters considered for the production of the tested composite powders are reported in

Table 4.2.

Table 4.2: Metal wires used for powder production.

Metal Wire	Wire Diameter[*mm*]		
Aluminum	0.20	0.25	0.35
Copper	0.10	0.20	0.31

The 0.1 *mm* Copper wire was covered with a thin protective plastic layer to prevent oxidation. Dedicated chemical and thermal treatments were applied to the wire to remove this coating.

At first, the wire was rounded on a metal spool, and then put into a furnace at 350 $°C$ for 4 hours to burn the protective layer.

Once removed from the furnace and cooled down, wire was rounded on a plastic spool in order to increase the surface exposed to chemical agents. The wire was then dipped into a solution of water and 10% *vol* of hydrochloric acid for one day in order to melt plastic residues without attacking the copper wire. Persistent residues were separated using an ultrasonic bath.

The resulting Cu wire was very fragile and hard to handle. The final effective diameter of the copper wire was $\sim$0.08 *mm*.

A small enroller was used to twist the composite wire. The different stiffness of the two wires caused a non-regular twisting. The thinner wire was usually rolled around the stiffer one.

In order to avoid mass fraction errors, 2 *m* of twisted wire were cut from the spool, separated and then weighted on a precision balance to determine the effective mass fraction. The theoretical and real Aluminum and Copper concentrations of the twisted wires used for powder production, are reported in Table 4.3.

Table 4.3: Al/Cu wires combinations and theoretical mass fractions.

Al diameter [mm]	Cu diameter [mm]	Theoretical concentration %		Real Concentration %	
		Al	Cu	Al	Cu
0.20	/	100	/	100	/
0.35	0.08	85	15	85	15
0.25	0.08	75	25	74	26
0.35	0.20	48	52	47	53
0.25	0.20	32	68	32	68
0.20	0.31	16	84	15	85
/	0.20	/	100	/	100

In the present work, powders are classified and named according to the real concentration reported in Table 4.3.

4.2.2 Wires Explosions

Metallic wires used to produce nanopowders by EEW method. It is necessary to choose the right production parameter considering two main aspects: resistivity and sublimation heat for the chosen monometallic or bimetallic wire. The tested powders were all produced in Argon atmosphere at a 2 bar pressure.

Table 4.4: Production parameters.

Wire Diameter [mm]		Length [mm]	ΔV [kV]	C [μF]
Al	Cu			
0.20	/	80	30	1.00
0.35	0.08	50	24	1.94
0.25	0.08	50	22	1.94
0.35	0.20	25	25	1.94
0.25	0.20	60	30	1.94
0.20	0.31	40	32	1.94
/	0.20	60	32	0.80

Three parameters have been set: length of metallic wire for each explosion, capacitance of condenser and voltage difference between the two faces of condenser [47].

4.2.3 Powder Coating

This work focuses on a characterization of composite powders of Al and Cu and on the effect of fluorinated coatings on the characteristics and the burning behavior of Al-Cu powders. In order to do this, both non-coated powders and their coated counterparts were investigated.

About 50 *g* for each type of powder, except the Copper one, has been coated with a polymeric material.

A composed Fluorel™ and Telomer n5 coating was chosen starting from previous results achieved by this research team [50] [52] [58]. In particular, Fluorel™ coating can provide oxidizing species to the particle during combustion, and reduces possible ageing effects of particle bulk *Al* [8].

Fluorel (Figure 4.8) is a commercial polymer product by 3M. It is made by 65.9% of Fluorine 22% Medium Thermal Carbon Black (N990), 2% MgO, and 4% $Ca(OH)_2$ [59].

Figure 4.8: Some blocks of Fluorel.

Table 4.5: Proprieties of Fluorel.

Physical Proprieties	
Appearance	*White Solid*
Density [Kg/m^3]	1800
Hardness	78
Tensile Strength, Ultimate [MPa]	17.0
Elongation at break %	180
Elastic Modulus [MPa]	7.2
Thermal Proprieties	
CTE, linear [$\mu m/mK$]	200
Specific Heat Capacity [$J/g\ K$]	1.65
Thermal Conductivity [$W/m\ K$]	0.240
Glass Transition Temperature [K]	255

Telomer n5 is a commercial product by HaloPolymer. See Figure 4.9 and Table 4.6.

Figure 4.9: Telomer n5.

Table 4.6 : Proprieties of Telomer n5 [60].

Chemical Formula	$H(CF_2CF_2)_2CH_2OH$
Appearance	White amorphous solid
Molecular weight [*g/mol*]	532.13
Melting Point [°*C*]	102
Boiling Point [°*C*]	230

The preparation procedure for the Fluorel™ + Telomer n5 coating is hereby reported:

A 5 *g* of Fluorel™ piece is divided into several smaller pieces and put inside a glass jug with Ethylene acetate.

To speed up the Fluorel™ mixing with Ethylene acetate, the jug is put into an ultrasonic bath for more than 30 minutes until a homogeneous milky cream is obtained (Figure 4.10).

Figure 4.10: Homogeneous solution of FLUOREL and Ethylene acetate.

Then a mixture composed by 50 *g* of metallic powder, 2.5*g* of Telomer n5 and 500 *ml* of Ethylene acetate is put inside a baker and the compound is then mixed with cavitations homogenizer at 500 *rpm* for, at least, 15 minutes to obtain the suspension of nanopowder into the solvent.

Solved Fluorel™ is added into the baker and then mixed again for 90 minutes until reaching a homogenous mixture.

After this the liquid media has been separated from the solid one using IKA HB10/RV10 evaporator/condenser. The powders are put inside a rotating ampoule (60 *rpm*) and heated at 50 *°C*, a vacuum pump forces the evaporation of ethylene acetate that condenses inside another recipient and is then re-used. This operation continues until no more solvent drops fall into the recipient.

Figure 4.11: Condenser/evaporator device.

A solid, porous layer remains inside the glass ampoule bonding the walls. A scraper is used to extract the whole solid compound that is then stored inside a cup.

The coated powders are then dried under vacuum for at least one day to remove the residuals of ethylene acetate.

Once dried, a compound of big, coated nanopowder clusters fill the cup. These are grinded by a pestle in order to reduce their size and then filtered(Figure 4.12).

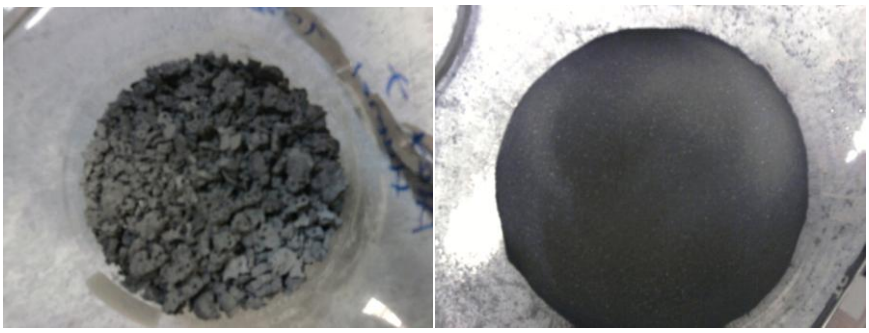

Figure 4.12: Big solid clusters of powder before and after filtering.

It takes almost one hour to obtain about 50 g of well filtered powder . A small amount of hard clusters remaining inside the sieve is wasted.

4.3. Nanopowder Characterization

The produced powders were characterized by different techniques. Performed tests aim at providing a characterization of powder morphologies, particle size distributions, and reactivity parameters. In particular TEM, and DSC/TGA tests were performed. The achieved results are hereinafter reported and discussed.

4.3.1 Nanopowders Particle Size Distribution

In order to measure the particle size distribution of the produced powders, SEM and Centrifuge analyses were performed.

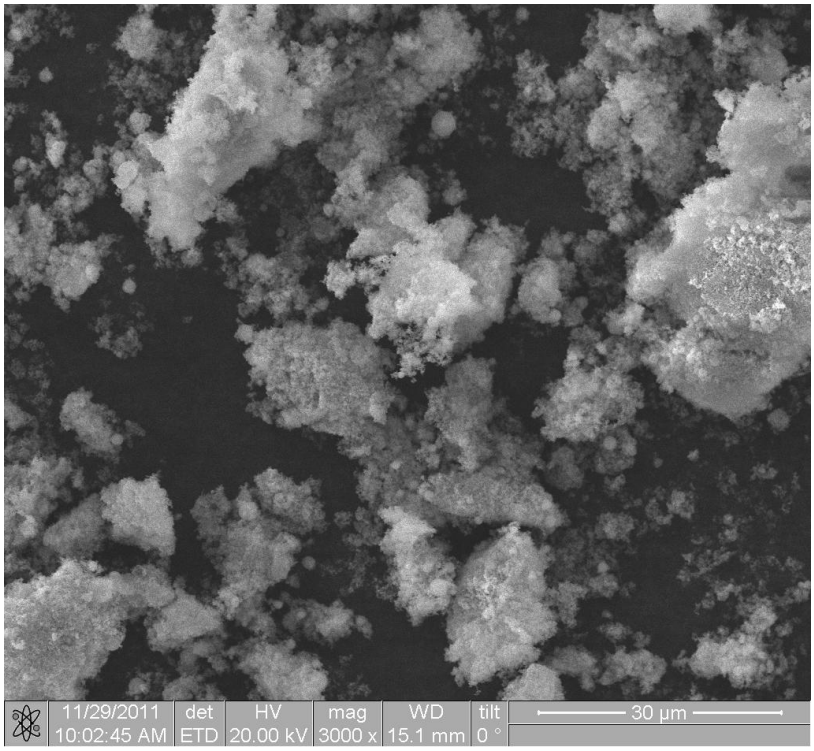

Figure 4.13: SEM image of ALEX™ powders.

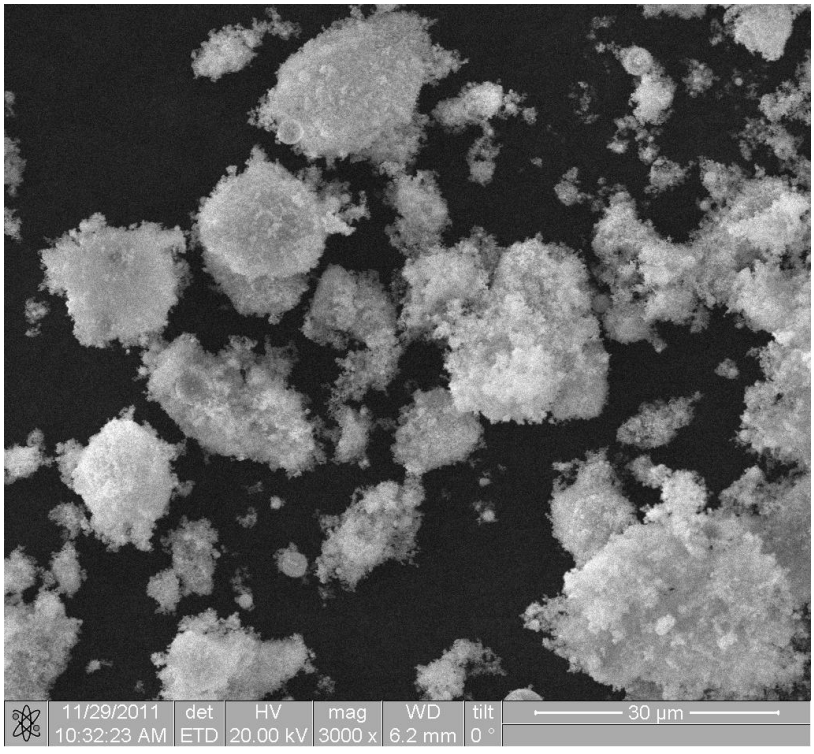

Figure 4.14: SEM image of Al32-Cu68 powders.

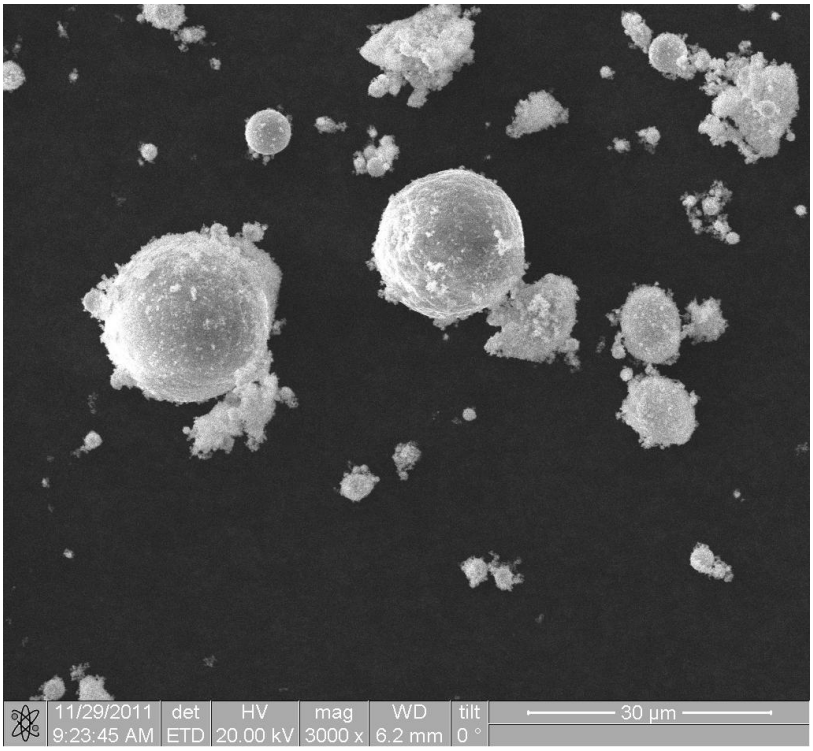

Figure 4.15: SEM image of Al15-Cu85 powders.

TEM images reveal the presence of a relatively broad particle size distribution (see Figure 4.13), with clusters of spherical particles [50]. Particle size distribution was investigated by centrifuge tests conducted by CPS DC24000 machine.

Particle size distribution was investigated on powders without any preliminary treatment and 30 *min* ultrasonication.

Table 4.7: Results of centrifuge tests.

Powder Type	**Mean Diameter [µm]**	
	Initial	30' sonic bath
ALEX™	0.24	0.22
ALEX™ Coated	0.41	0.32
Al85-Cu15	0.35	0.21
Al85-Cu15 Coated	0.38	0.20

Al74-Cu26	0.74	0.44
Al74-Cu26 Coated	0.85	0.34
Al47-Cu53	0.26	0.19
Al47-Cu53 Coated	0.82	N.A
Al32-Cu68	1.84	0.40
Al32-Cu68 Coated	N.A.	N.A.
Al15-Cu85	0.70	0.43
Al15-Cu85 Coated	0.45	0.30
Cu	0.67	0.44

As shown by the results reported in Table 4.7, without any ultrasonication, nanopowder sizes resulted bigger than the expected, nominal 100 *nm*. This was due to the presence of clusters of particles, as shown by the mean particle size reduction produced by ultrasonication. Centrifuge results provide useful information also for the manufacturing phase, highlighting the importance of ultrasonication.

Sonic bath reduces mean particle size (see Table 4.7), since the process, breaks particle clusters. As shown in Figure 4.16, 30 *min* ultrasonication process can provide narrower Al15-Cu85 particle size distribution. Particles with measured diameter of ~400 *nm* starting are obtained from non-ultraonicated powders characterized by a wider particle size distribution.

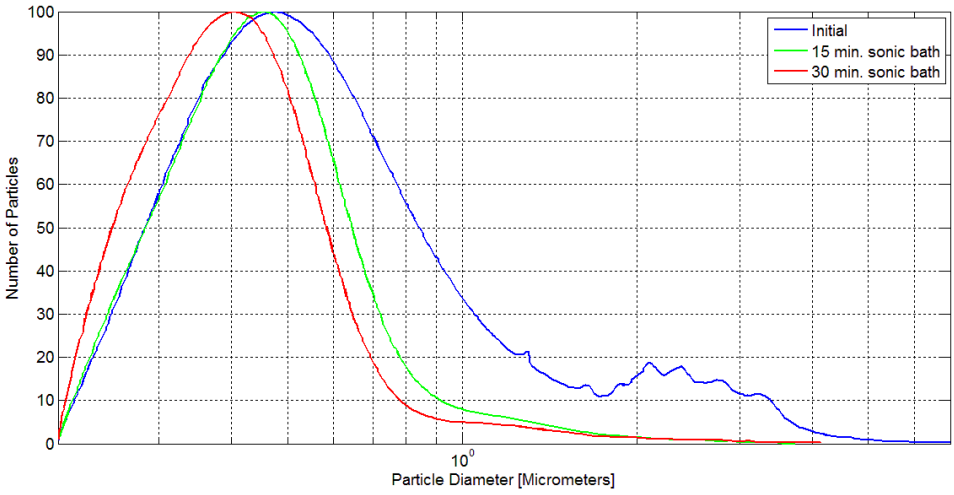

Figure 4.16: Al15-Cu85 centrifuge test results.

4.3.2 DSC-TGA Tests

Produced powders were characterized by DSC-TGA . The DSC-TGA tests were performed at the Technical Physics Department of Tomsk State University with a NETZSCH STA 409 PC/PG machine.

Tests were performed in an air atmosphere, with heating rate of 10°C/min, in the temperature range from standard room temperature to 1200 °C. Argon was used for reference pan atmosphere.

The approach chosen to determine the reactivity parameters of the powders is fully described in [61].

Reactivity parameters are schematically shown in Figure 4.17.

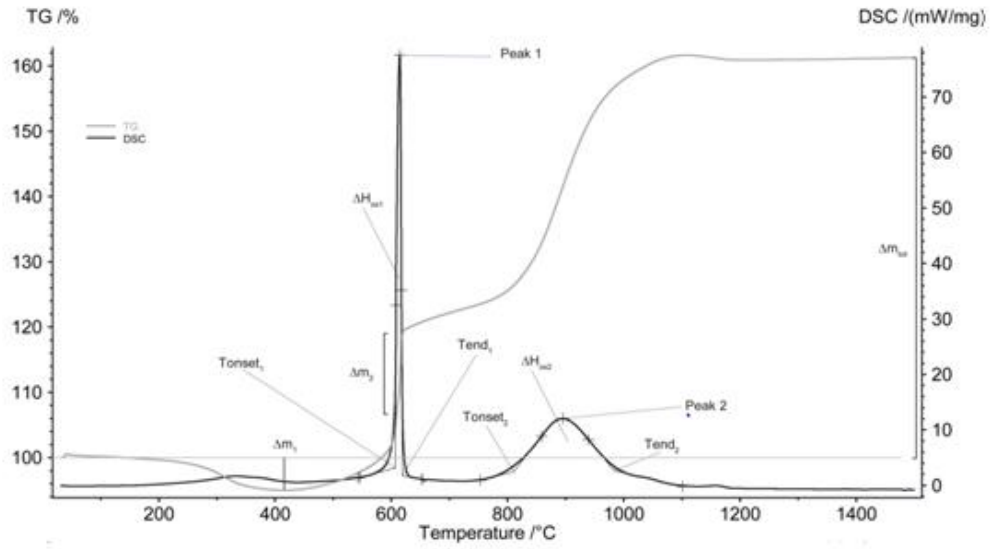

Figure 4.17: DSC-TGA powder reactivity parameters [50] [61].

While nAl is widely studied by thermal analyses, no information is so far available in the open literature for DSC-TGA analyses of composite powders. DSC-TGA data for the tested powders are reported in Table 4.8. All tested powders exhibit a small mass decrease in the earlier phases of the heating process (T < 400 °C). This mass loss (Δm_1) is due to any of the following reasons [58]:

- evaporation of water vapor/gases adsorbed on nanoparticle surfaces;
- evaporation of residual solvent (possible only for coated powders);
- coating decomposition (possible only for coated powders);

Aluminum nanopowders usually exhibit a staged combustion when tested in DSC-TGA with relatively low heating rates [62] [58]. When observed, the two exothermic peaks are separated by Al melting temperature (~660°C). The observed first peak is associated with a fast reaction between the condensed phase aluminum and the gaseous oxidizer. It occurs at temperatures lower than 660°C. The second exothermic peak is usually observed for temperatures higher than 660°C. This second peak is not as marked as the first one, since it is associated with reaction of the residual Al. For DSC-TGA tests conducted in N_2 containing media, staged exothermic reaction of Al can be related also to nitridation of Al [63] [64]. The tested ALEX™ exhibits a marked first oxidation peak whose onset temperature is 583 °C, while maximum of the peak is achieved at 586.8 °C. The heat release during this exothermic process is 2089 *J/g*.

The corresponding mass increase as evaluated by TGA is 28.2%. Then , after melting of the residual Al a less intense oxidation phase with a mass gain up to 64.0%. The achieved ALEX™ DSC-TGA data do not enable evaluation of the heat release in the second peak. This less intense reaction is related to the available Al amount (after the first oxidation process), and particle size distribution. The smaller particles reacts at lower temperatures, while bigger particles/clusters oxidizes at T > 660 °C. The behavior of coated ALEX™ powder is characterized by higher Δm_1 than ALEX™ Coated due to the presence of the coating [50]. The oxidation onset temperature for the first oxidation peak of the Fluorel™ + Telomer n5 coated powder is 608 °C. Thus it results higher than the corresponding ALEX™ value. of ~25 °C. This testifies a protective action of the fluoropolymer coating on the Al core of the coated ALEX™ particles, a result confirming experimental findings reported in [8]. The fluoropolymer coating reduces powder reactivity at low temperatures. First oxidation peak is observed at T = 617.3 °C (see Figure 4.18). A second oxidation stage is observed for T > 700 °C. The heat release of this stage is 1662 *J/g* , while the final mass gain from TGA results 48.0% at 1200 °C.

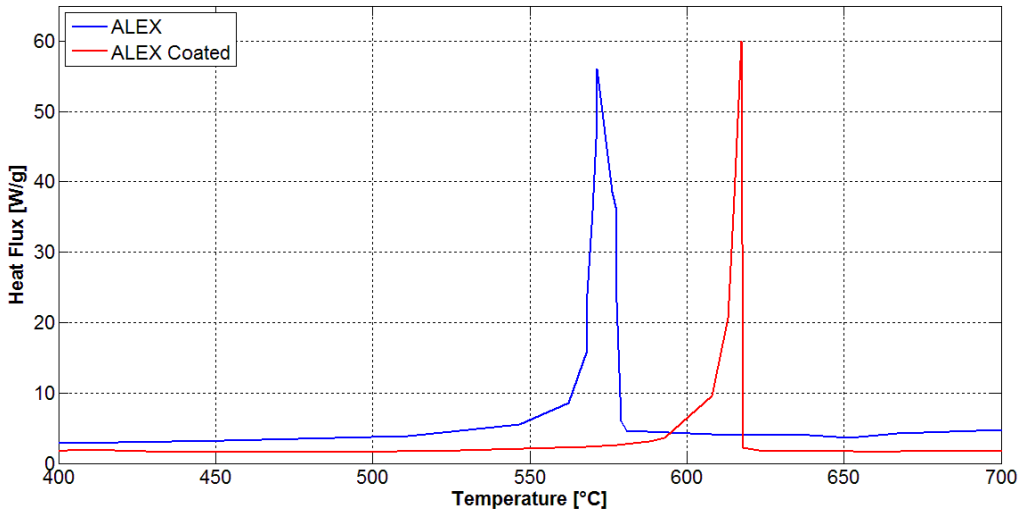

Figure 4.18: Comparison between first peaks of coated and uncoated ALEX™.

Introduction of copper significantly changes powder behavior in DSC-TGA under the investigated conditions. In particular, no clearly staged powder oxidation occurs (see Table 4.8). The oxidation onset and peak temperatures decrease for increasing copper mass fraction, as shown in Figure 4.19. Copper is characterized by a low oxidation onset temperature (179.4 °C), but its oxidation process proceeds slowly. In particular, oxidation reaction produces limited mass gains (8.7 % at T = 196.6 °C), as can be seen by the TGA data reported in Table 4.8.

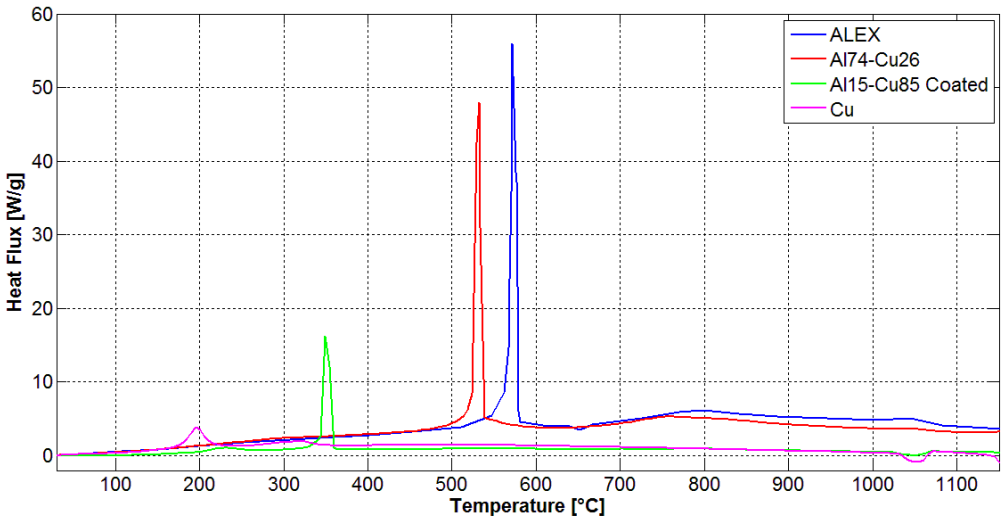

Figure 4.19: DSC analysis results for powder with different concentration of copper.

The powders characterized by high concentration of copper, at temperatures higher than 1000 °C an absorption of heat and a loss of total mass can be observed, as shown in Figure 4.20. This behavior can be due to to a passage from two different types of Cu oxides as shown in Eq.(4.1) and discussed in [65].

$$CuO \rightarrow \frac{1}{2}Cu_2O + \frac{1}{4}O_2 \qquad \textbf{(4.1)}$$

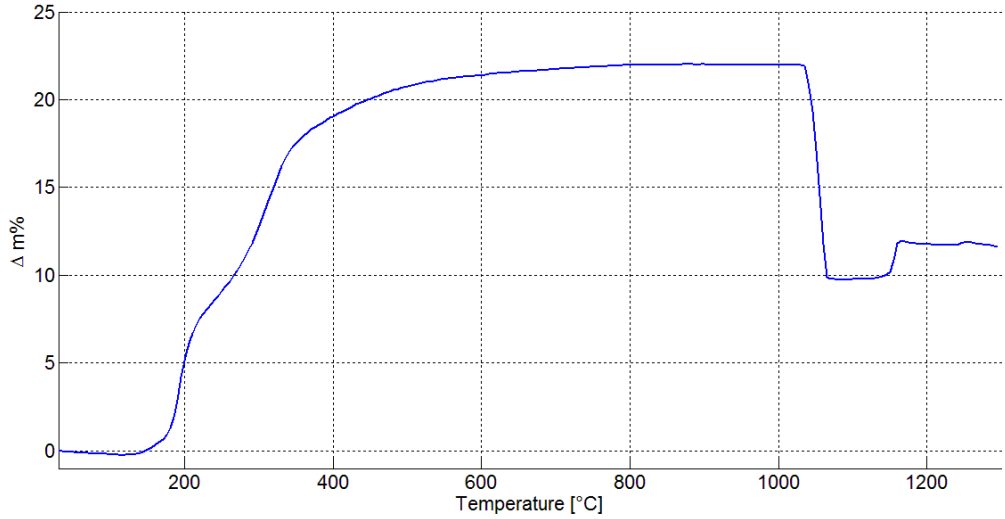

Figure 4.20: TGA results for copper powders.

Considering the total heat release (up to 1200 °C), composite powders containing Cu exhibit an energy release reduction with respect to Al nanopowders (see Table 4.8). This is a consequence of what was extensively discussed in Chapter 3 about oxidation of Al vs. oxidation of Cu. The DSC data reported in Figure 4.23, underline the oxidation onset and peak temperature shift of composite Al-Cu powders vs. ALEX™. Maximum heat flow per gram, for high Aluminum concentration bimetallic powders is close to ALEX™ one.

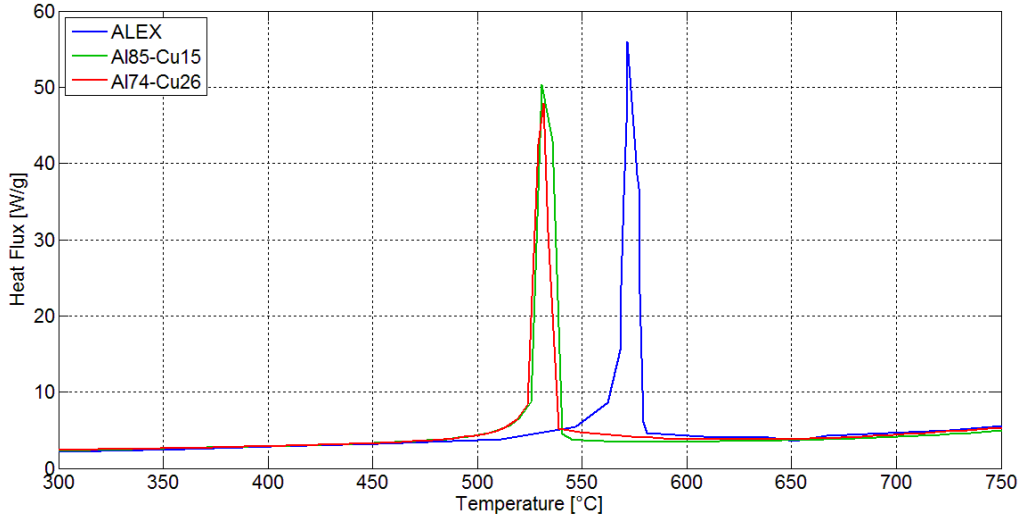

Figure 4.21: Heat flux for low concentration copper powders in comparison with ALEX™.

For high concentration copper powders, on the other hand, maximum heat flow per gram is significantly smaller than ALEX™. Peak temperature is dramatically different from ALEX™ one.

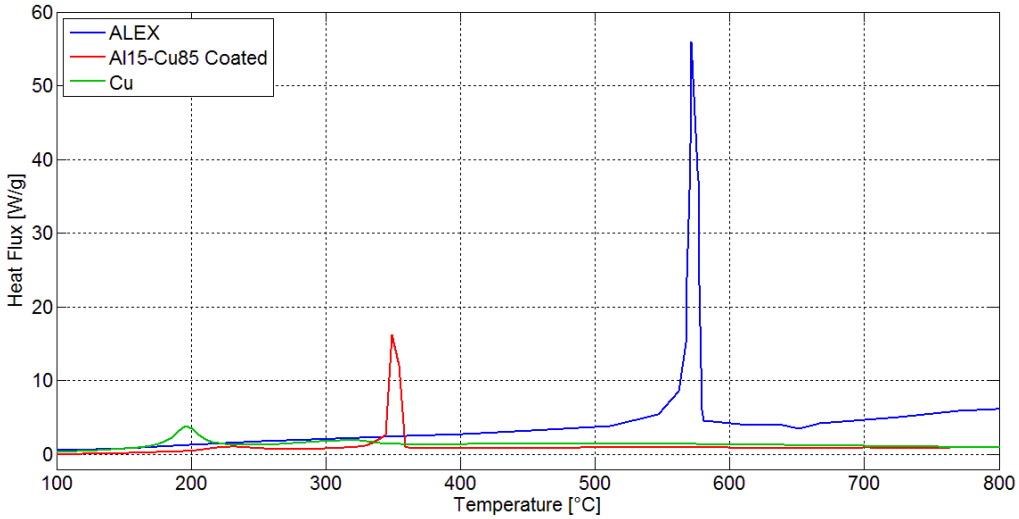

Figure 4.22: Heat comparison of oxidation onset/peak temperatures for ALEXTM and composite Al-Cu powders with 15% and 26% Cu.

In the DSC-TGA of coated powders with high Cu content, coating degradation and metal oxidation can occur over similar temperature range. In these cases it is possible to record a global mass loss when oxidation of metal starts (as for Coated Al15-Cu85 data reported in Table 4.8).

Mass variations due to oxidation of metal are lower when a high concentration of copper is added in powders. This is because of the number of Oxygen atoms inside metal oxide. Copper oxide is (CuO) at low temperatures and (Cu_2O) at high, aluminum oxide is (Al_2O_3).

In order to understand powder non-isothermal oxidation behaviors of Al-Cu powders, metal content is not enough and different factors/characteristics must be considered.

The composite metal powders generated by EEW are made up of single initial metals and new composite molecular structures called intermetallic compounds [66]. These materials have not been extensively investigated in the open literature, though it is proved that they can have different structures and proprieties (and therefore, combustion behavior with respect to original metals. Some research activity was conducted in order to identify and characterize intermetallic compounds created during Al-Cu composite powder production [6]. An important parameter influencing the concentration of intermetallic species is the distance between metallic wires during explosion of the virgin material. In particular, a smaller distance between exploding wires promotes a higher production of intermetallic compounds.

Type and concentration of intermetallic compounds are highly influenced by the energy given to original metals [67].

According to previous studies on EEW produced composite Al-Cu powders a great quantity of Cu_4Al_9 and $CuAl_2$ was observed into powder composition [6]. In spite of this, no information about the ballistic behavior of these powders is available in the open literature. Moreover, intermetallic compounds are only one aspect of the problem; the second is distribution of ingredients inside the bimetallic powder. A different distribution of the metals can affect the oxidation reactions of the different powders.

For Al-Cu powders a higher concentration of Cu on particle surface was observed [6]. This is related to several phenomena (wire explosion, expansion into the combustion chamber), and, in particular, to the higher melting temperature of Cu. An example of the non-homogeneous structure of composite Al-Cu powders is given in Figure 4.23.

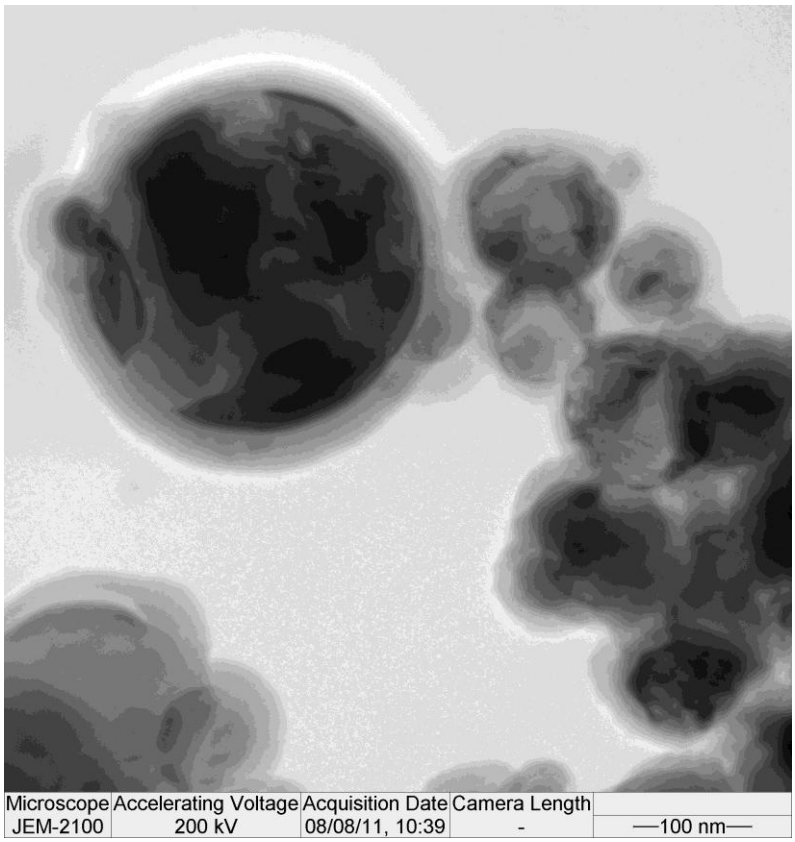

Figure 4.23: High-resolution image of some bimetallic Aluminum-Copper powders.

Table 4.8: Reactivity parameters of powders from DSC-TGA analysis.

Reactivity parameter	ALEX™	ALEX™ Coated	Al85-Cu15	Al74-Cu26	Al15-Cu85 Coated	Cu
T_{onset1} [°C]	583.0	608.0	526.6	524.5	290.0	179.4
$T_{ox\ peak1}$ [°C]	586.8	617.3	531.9	531.8	348.2	196.6
Maximum heat flow $[W/g]$	51.0	55.9	50.7	47.9	16.4	3.8
Δm (before the first peak) [%]	-0.1	-10.4	1.7	-0.2	-3.9/-14.1[4]	0.2
$\Delta H_{ox1}[J/g]$	2089	2317	2031	1529	647	448
ΔH_{ox2} $[J/g]$	N.A.	1662	N.A.	N.A.	N.A.	N.A.
Δm (After the first peak) [%]	28.2	29.1	24.9	19.7	-14.1	8.7
Δm_{tot} (up to 1200 °C) [%]	64.0	48.0	58.0	50.0	-7.0	11.5

[4] Coating decomposition and oxidation starting point are overlapped

5. Samples Manufacture

During experimental activities 13 different metal loaded fuels had been tested. Standard manufacturing HTPB [68] procedure have been partially changed, in order to increase dispersion of powders and reduce porosity of the grain.

Samples for ballistic tests have cylindrical shape. The cylindrical samples are elements of *30 mm* of length and *18 mm* of external diameter casted in a metallic case. The cylindrical grain has a circular central port perforation with an internal diameter of *4 mm*.

Figure 5.1: HTPB + 10% Al15-Cu85 sample.

5.1. Fuel Composition

Each formulation is loaded with a different metallic additive. In order to focus on differences in behavior during combustion of different nano-powders, every fuel was

made using the same concentrations of the ingredients, binder and metal. The energetic powders have been added as 10% of total fuel mass. The choice of this percentage has been made to match the standard SPLab ballistic analysis.

Table 5.1: Fuel composition.

	Mass Fraction %
HTPB-R45	70.97
DOA	11.74
IPDI	6.90
TIN	0.39
Metallic Powder	10.00

Proprieties for each used ingredients are presented in Chapter 3.

5.2. Manufacturing Process

Preparation has been performed in a chemical laboratory with an environment control in terms of humidity and temperature.

1. Required quantity of HTPB-R45 is poured in a Teflon beaker.
2. The beaker containing the HTPB resin is placed in a 60°C oven for at least 30 minutes in order to reduce viscosity and facilitate next steps.
3. The beaker containing the less viscous HTPB resin is placed in a vacuum bell for at least 30 minutes in order to air bubbles inside polymer.
4. Half quantity of required DOA is added to HTPB to reduce viscosity of binder, the ingredients are mixed under vacuum for 30 minutes.
5. Metal powders are prepared into a Pyrex beaker and placed in an ultrasonic bath for at least 15 minutes in order to disaggregate the bigger clusters eventually formed by nanopowders.
6. Powders are added to the HTPB into the main beaker. Ingredients are mixed again in ultrasonic bath under vacuum for at least 30 minutes. Nanoparticles bring together a great quantity of air inside the compound.

7. Curing agent (IPDI) is added to other ingredients. Mixing in ultrasonic bath continues for at least other 30 minutes
8. The last part of DOA and TIN are added to the compound. Mixing still continues in the previous conditions for about 10 minutes. Attention has to be paid to the possible on-set of early reticulation reaction
9. Compound is poured into moulds
10. Samples are closed and placed in 36°C heater for 23 hours. 36°C is temperature needed to activate reaction with curing catalyst.
11. Samples are now placed in 60°C heater for at least 2 hours.

5.2.1. HTPB + 10% ALEX™

Table 5.2: Theoretical vs. real weight of each ingredient for HTPB + 10% ALEX™.

	Theoretical Mass [g]	Real Mass [g]
HTPB	44.173	44.168
DOA	7.303	7.304
IPDI	4.289	4.289
TIN	0.241	0.240
ALEX™	6.225	6.226

5.2.2. HTPB + 10% ALEX™ Coated

Table 5.3: Theoretical vs. real weight of each ingredient for HTPB + 10% ALEX™ Coated.

	Theoretical Mass [g]	Real Mass [g]
HTPB	50.483	50.479
DOA	8.346	8.344
IPDI	4.902	4.902
TIN	0.275	0.275
ALEX™ Coated	7.112	7.115

5.2.3. HTPB + 10% Al85-Cu15

Table 5.4: Theoretical vs. real weight of each ingredient for HTPB + 10% Al85-Cu15.

	Theoretical Mass [g]	Real Mass [g]
HTPB	44.173	44.168
DOA	7.303	7.304
IPDI	4.289	4.289
TIN	0.241	0.238
Al85-Cu15	7.112	7.115

5.2.4. HTPB + 10% Al85-Cu15 Coated

Table 5.5: Theoretical vs. real weight of each ingredient for HTPB + 10% Al85-Cu15 Coated.

	Theoretical Mass [g]	Real Mass [g]
HTPB	52.383	52.382
DOA	8.661	8.660
IPDI	5.086	5.089
TIN	0.286	0.287
Al85-Cu15 Coated	7.379	7.378

5.2.5. HTPB + 10% Al74-Cu26

Table 5.6: Theoretical vs. real weight of each ingredient for HTPB + 10% Al74-Cu26.

	Theoretical Mass [g]	Real Mass [g]
HTPB	44.765	44.764
DOA	7.401	7.401
IPDI	4.347	4.348
TIN	0.244	0.242
Al74-Cu26	6.306	6.308

5.2.6. HTPB + 10% Al74-Cu26 coated

Table 5.7: Theoretical vs. real weight of each ingredient for HTPB + 10% Al74-Cu26 Coated.

	Theoretical Mass [g]	Real Mass [g]
HTPB	52.383	52.384
DOA	8.661	8.658
IPDI	5.086	5.085
TIN	0.286	0.288
Al74-Cu26 Coated	7.380	7.381

5.2.7. HTPB + 10% Al47-Cu53

Table 5.8: Theoretical vs. real weight of each ingredient for HTPB + 10% Al47-Cu53.

	Theoretical Mass [g]	Real Mass [g]
HTPB	51.156	51.155
DOA	8.458	8.459
IPDI	4.967	4.965
TIN	0.279	[5]0.056
Al47-Cu53	7.207	7.381

[5] Less quantity of TIN in order to control reticulation processes during last mix

5.2.8. HTPB + 10% Al47-Cu53 Coated

Table 5.9: Theoretical vs. real weight of each ingredient for HTPB + 10% Al47-Cu53 Coated.

	Theoretical Mass [g]	Real Mass [g]
HTPB	51.500	51.500
DOA	8.515	8.516
IPDI	5.001	5.002
TIN	0.281	0.282
Al47-Cu53 Coated	7.255	7.253

5.2.9. HTPB + 10% Al32-Cu68

Table 5.10: Theoretical vs. real weight of each ingredient for HTPB + 10% Al32-Cu68.

	Theoretical Mass [g]	Real Mass [g]
HTPB	64.158	64.158
DOA	10.607	10.609
IPDI	6.230	6.232
TIN	0.350	[6]0.082
Al32-Cu68	9.038	9.039

[6] Less quantity of TIN in order to control reticulation processes during last mixing under vacuum

5.2.10. HTPB + 10% Al32-Cu68 Coated

Table 5.11: Theoretical vs. real weight of each ingredient for HTPB + 10% Al32-Cu68 Coated.

	Theoretical Mass [g]	Real Mass [g]
HTPB	64.158	64.159
DOA	10.607	10.605
IPDI	6.230	6.228
TIN	0.350	[7]0.084
Al32-Cu68 Coated	9.038	9.043

5.2.11. HTPB + 10% Al15-Cu85

Table 5.12: Theoretical vs. real weight of each ingredient for HTPB + 10% Al15-Cu85.

	Theoretical Mass [g]	Real Mass [g]
HTPB	45.254	45.249
DOA	7.482	7.479
IPDI	4.394	4.396
TIN	0.247	0.248
Al15-Cu85	7.482	7.489

[7] Less quantity of TIN in order to control reticulation processes during last mixing

5.2.12. HTPB + 10% Al15-Cu85 Coated

Table 5.13: Theoretical vs. real weight of each ingredient for HTPB + 10% Al15-Cu85 Coated.

	Theoretical Mass [g]	Real Mass [g]
HTPB	52.384	52.385
DOA	8.661	8.662
IPDI	5.086	5.085
TIN	0.286	0.288
Al15-Cu85 Coated	7.380	7.382

5.2.13. HTPB + 10% Cu

Table 5.14: Theoretical vs. real weight of each ingredient for HTPB + 10% Copper.

	Theoretical Mass [g]	Real Mass [g]
HTPB	64.741	64.741
DOA	10.704	10.702
IPDI	6.286	6.288
TIN	0.353	[8]0.071
Cu	9.120	9.116

[8] Less quantity of TIN in order to control reticulation processes during last vacuum mixing

5.3. Fuel Density Results

The actual fuel density is an important index enabling the evaluation of manufactured fuel overall quality. The densities of the tested formulations were measured by Gibertini Europe 500 precision balance. For a given fuel, the measured actual density is compared to the corresponding TMD. The porosity of the manufactured fuel grain can be evaluated as:

$$\Delta\rho_{f,\%} = 100 \cdot \frac{\mathrm{TMD} - \rho_f}{\mathrm{TMD}} \quad \textbf{(5.1)}$$

Low porosity means a few amount of air trapped into fuel during manufacturing and thus a better overall quality of the samples, though porosity can be negative in case of excess of high density materials (metal, metal oxides) inside the fuel. Minimum $\Delta\rho_{f,\%}$ value is observed for Al47-Cu53 Coated loaded fuel: -1.2 %. The TMD, actual densities and porosities of the tested fuels are reported in Table 5.15. Some fuels exhibit relatively high level of porosity: about + 4 %. This is mainly due to air trapped into nano-sized powder clusters, and viscosity increase due to their addition to the solid fuel formulation. During the mixing phase, enhanced viscosity yields a possible air trapping. Under the investigated conditions, vacuum cycles during manufacturing can only limit these effects. Moreover, when considering Al-Cu bimetallic powders, the difficult determination of additive density must be considered.

Table 5.15: TMD and actual density of the investigated formulations. The reported errors are defined considering 95% confidence interval for four performed measurements.

Fuel	TMD, [g/cm³]	Actual Density, [g/cm³]	$\Delta\rho_{f,\%}$ Eq. (1)
HTPB + 10% ALEX™	0.980	0.953±0.015	2.75
HTPB + 10% ALEX™ Coated	0.980	0.959±0.006	2.14
HTPB + 10 % Al85-Cu15	0.985	N.A.[9]	N.A.
HTPB + 10 % Al85-Cu15 Coated	0.985	0.955±0.015	3.03
HTPB + 10 % Al74-Cu26	0.986	0.967±0.009	1.91
HTPB + 10 % Al74-Cu26 Coated	0.986	0.944±0.018	4.31
HTPB + 10 % Al47-Cu53	0.993	0.985±0.012	0.81
HTPB + 10 % Al47-Cu53 Coated	0.993	1.003±0.015	-1.21
HTPB + 10 % Al32-Cu68	0.996	0.994±0.006	0.23
HTPB + 10 % Al32-Cu68 Coated	0.996	1.002±0.012	-0.56
HTPB + 10 % Al15-Cu85	1.001	0.953±0.015	4.56
HTPB + 10 % Al15-Cu85 Coated	1.001	0.980±0.015	2.13
HTPB + 10 % Cu	1.005	0.992±0.012	1.29

[9] Test not performed due to additive shortage

6. Experimental Set-Up

In this chapter the experimental setup and data reduction technique used for solid fuel ballistic data reduction are presented. The test rig is a 2D-radial micro-burner enabling combustion of cylindrical single port samples under variable operating conditions. Solid fuel regression rate is evaluated on optical, non-intrusive time-resolved technique based on central point sampling during combustion [69] [70].

6.1. 2D-Radial Burner

The 2D-Radial Micro-burner was originally designed by Romano in 1991 [71]. The test rig was deeply modified by Bosisio and Raina [72] [73]. Paravan, Sossi and Duranti [27] [58] [52] designed further updates of the experimental facility.

The test rig is mainly composed by:

1. Combustion chamber;
2. Injector;
3. Inlet pneumatic line;
4. Exhaust line;
5. CO_2 laser
6. Acquisition system
7. Power supply

6.1.1. Combustion Chamber

Combustion chamber is the main component of the facility. Combustion takes place in this closed stainless steel volume. Outer diameter of combustion chamber is 118 *mm*, while inner diameter is 86 *mm.* The free internal volume of the combustion chamber is 591 dm^3. Combustion chamber is made by a fixed part and a movable one. Fixed part is a stainless AISI 316 steel cylindrical shell [71]. Two quartz windows are placed on the lateral surface of the combustion chamber fixed part. Three NPT connections are placed on the base of the cylindrical body. Two of them connect the combustion chamber to the exhaust pipeline, while the third one lodges a Brass lodging for a *ZnSe* lens. The latter is required by the use of a CO_2 laser for tested strand ignition. The movable part of the combustion chamber moves on a rail. The movable part lodges the injector. The two parts are joined together by a thread with O-ring seal. The maximum combustion chamber allowable pressure is *3.0 MPa*. In spite of this, due to optical windows limit is set to 2.0 *MPa*.

6.1.2. Injector

The Injector is made of brass and is connected to oxidizer feed line and to combustion chamber movable part (see Figure 6.1) Injector terminal enables sample lodging for test execution. The inlet oxidizer runs to a pre-combustion chamber homogenizing the flow before it enters the injector-head. The volume of the pre-combustion chamber is limited by two flanges lodging quartz windows. From pre-combustion chamber, oxidizer flows through injector head. This has eight radial channels with proper regulating stems. Acting on radial channel stems it is possible to control the behavior of the oxidizer flow: both standard and swirled flow can be achieved. Sample is inserted into injector terminal. Due to the original design of the injector, no obstacles hinder the visualization of the strand head-end. A 45°-mirror reflects the head-end image of the testing strand to the lateral windows of the combustion chamber, as shown in Figure 6.2. Therefore head-end images can be captured by a digital high speed camera.

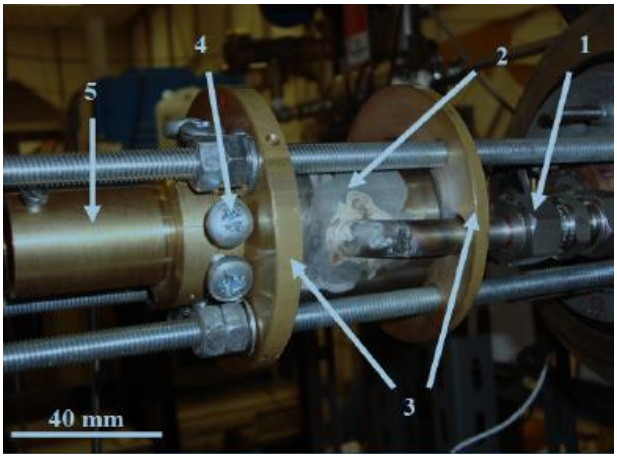

Figure 6.1: **2D radial micro-burner injector. The following elements are highlighter: 1 oxygen feed line, 2 pre-combustion chamber, 3 flanges for optical quartz windows accommodation, 4 injector-head with screws for oxidizer injection control (standard/swirl flow), 5 injector terminal (sample lodging) [52].**

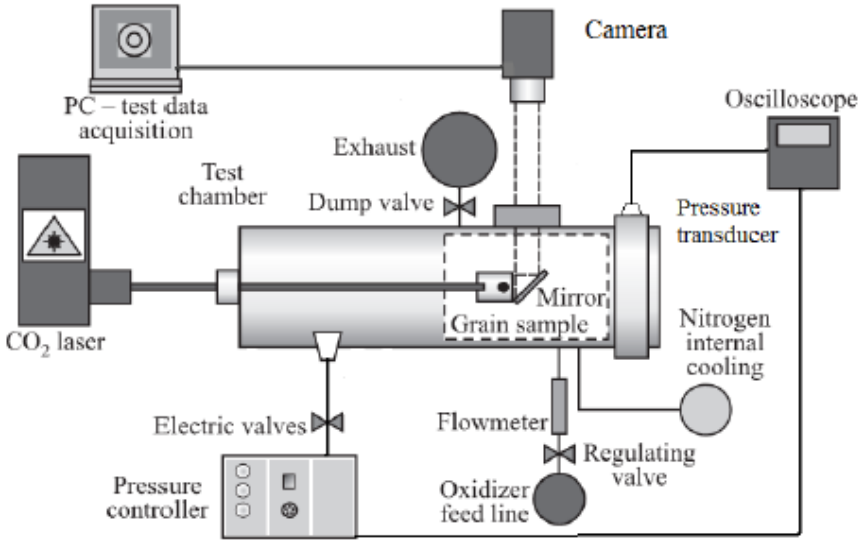

Figure 6.2: experimental line overview [74].

6.1.3. Pneumatic Line

The inlet pneumatic line is made by pipes and junctions delivering to the combustion chamber the gaseous flows of oxidizer and coolant.

The oxygen line starts from oxygen cylinders. A pressure reducer drops the pressure from the cylinder level (~25 *MPa*) to ~3.0 *MPa*. Oxidizer flow passes through a check valve and then reaches an analogical flow-meter. From the latter pipeline enters the movable part of the combustion chamber. The inlet pipe then reaches the pre-combustion chamber (see Figure 6.1-2). The coolant line starts from Nitrogen cylinders

used during combustion to cool down the chamber inner walls and to hinder exhaust gases/soot from combustion to hinder the head-end image reflection by the 45°-mirror. A pressure reducer drops the pressure from 25 *MPa* to ~5.0 *MPa*. Check valves, ball valve and mass flow regulation valve enable controlling the coolant line flow. A compressed air line (0.7 *MPa*) is linked to the Nitrogen line. The latter is used for preliminary controls on pressure losses prior of the experimental runs and for internal cleaning/cooling after each test.

6.1.4. Exhaust Line

Exhaust line is based on two independent stainless steel pipelines. Exhaust line brings the exhaust gases from the combustion chamber to the atmosphere. Each pipe is connected to three electro-valves working in order to maintain combustion chamber pressure (see Figure 6.2). The latter are governed by a pressure controller receiving information from a transducer placed in the combustion chamber. After the electrovalves, polypropylene tubes deliver the exhaust gases to the atmosphere. Exhaust pipelines undergo heavy thermal loads. Because of this a convective cooling by compressed air flow and a water heat exchanger are implemented. The exhaust line electrovalves are driven by a high resolution piezo-resistive pressure transducer whose data are reported in Table 6.1. The electrovalves characteristics are given in

Table 6.2. The closed-loop control architecture enables to maintain a quasi-steady combustion chamber pressure inside the combustion chamber (see Figure 6.3).

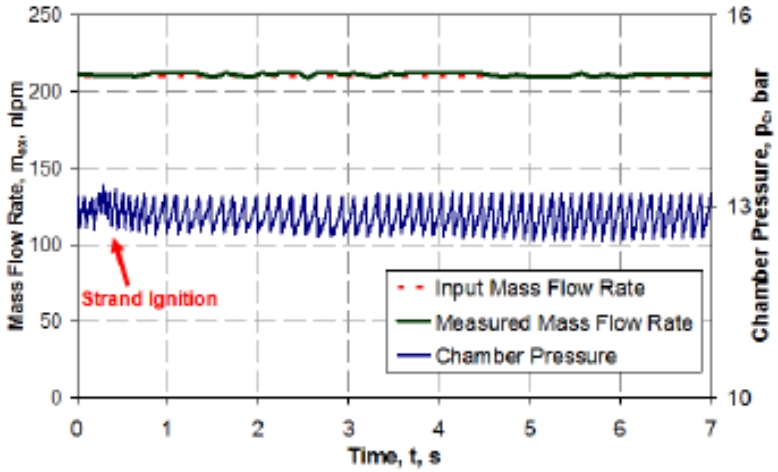

Figure 6.3: Typical operating profile for a ballistic characterization test. Note quasi–steady value of pc. Primer charge and Strand ignition is identified by a marked peak in chamber pressure in time (see red arrow) [52].

Moreover, combustion chamber pressure and oxidizer mass flow rate can be independently controlled varying the Nitrogen flow rate.

Table 6.1: Technical data of the pressure transducer.

Maximum Work Pressure [*bar*]	70
Maximum FS Pressure [*bar*]	210
Sensitivity [*mV/(bar sg)*]	1.456
Output at Zero Pressure [% FS]	± 5
Maximum Output [*mV*]	100
Temperature Field [K]	218 – 440
Power Supply [*VCC*]	10 – 12
Input Impedance [*Ω*]	1000
Output Impedance [*Ω*]	1000

Table 6.2: Technical data of the electro valves.

Model	**Peter & Paul 79K9DGM**
Maximum Pressure Gap [*bar*]	35
Diameter of the central Hole [*in*]	5/32
Junction Type	1/4 NTP
Power supply [*VCC*]	24
Power Consumption [*W*]	16

6.1.5. CO_2 Laser (Strand Ignition)

The tested strands are ignited by a pyrotechnical primer charge. The formulation and sized of the latter are fixed. This grants that ignition energy is the same for all of the tested formulations. The primer charge is ignited by CO_2 infrared laser radiation impinging on it. This allows non-intrusive, easy and reliable ignition of the samples. The main disadvantage of this technique is the impossibility of multiple ignitions since pyrotechnical charge expires after once ignited.

6.1.6. Acquisition System

A Photron Ultima APX high speed, high resolution camera is used to record combustion tests. High speed camera data are reported in Table 6.1. Due to Photron buffer memory size and combustion test duration, a frame rate of 500 *fps* is used for the visualizations. The recorded video is stored in digital format for data processing.

Table 6.3: Technical data of Photron high-speed camera.

Maximum resolution [*pixels*]	1024x1024
Maximum Frame Rate [*fps*]	120000
Minimum Frame Rate [*fps*]	50
Memory Buffer [*GB*]	8
Sensor Model	CMOS

6.1.7. Power Supply

A stabilized 220 *V* AC net supply electric power to part of the test rig hardware. This enables avoiding fluctuations that could damage the equipments. Electro valves are powered by a 24 *V* DC transformer. The pressure controller and the pressure transducer are powered by a 12 *V* DC feeder through a 10 *V* DC transformer.

Laser, high speed camera, lights and laptop need high voltage so they are directly connected to the stabilized laboratory web.

6.2. Typical run description

6.2.1 Preliminary operations

Preliminary checks must be made before tests start. In order:

- Check level of laser-mix gas inside the cylinder in the outside compartment.
- Check that pressure of cooling gas (Nitrogen) is much higher than scheduled tests pressure.
- Remove Photron cover.
- Remove mirror cover.
- Check if there are enough rubber sealing for all the tests.

Preliminary operations required to grant the correct functioning of the 2D radial micro-burner start with hardware warm-up (digital flowmeter, computer, oscilloscope, pressure control chain elements, and laser). Checks on the fixed connections of the combustion chamber are performed in order to avoid possible leakages of dump pipeline and external cooling system, after this, alignment of laser and optical paths must be verified. Laser path verification is mandatory in order to grant homogeneous ignition of the primer charge: anisotropic ignitions could result in irregular ignitions of the tested strand thus altering the quality of the combustion. In order to avoid this, optical elements of the laser path are regulated to grant laser beam impingement at the center of a calibration sample. A small piece of paper is inserted in the latter at head-end side. This element acts as a testing charge, enabling verification/regulation of laser beam impinging point. After this combustion chamber is closed and proper optical alignment of 45° mirror and camera is controlled by a metallic drilled cylinder set as a sight as shown in Figure 6.4.

Figure 6.4: Sight cylinder used for sample alignment

Using a led-light is possible to light the cylinder and see on computer how the port looks like. Small adjustments are mandatory to reach a good alignment suggested by the wires position. If the single wire stays in the middle of the two frontal wires, alignment is correct; both vertical and horizontal alignment are necessary. Video calibration is achieved visualizing a calibration sample that is lit up by a light pointing from the laser optical access. Calibration sample is an empty cylindrical steel case with graph paper at the head-end section. Due to the regular image of the graph paper optics (in particular the 45° mirror and the camera position/focus) are regulated so that possible image distortions are avoided.

At this point a brief calibration video is recorded. This video will be used in the post-analysis phase in order to get a proper conversion factor between millimeters (of the graph paper) and pixels (of the recorded image). Camera operating parameters are

regulated to grant correct video–recording of the combustion (in particular shutter and diaphragm are regulated to provide proper exposure of the sensor during combustion). Next step of the preliminary operations is the check of the absence of leakages from the inlet/outlet pipelines connecting the cylinders to the combustion chamber, and the latter to the dump pipeline. This is done by a cold test during which the combustion chamber is pressurized by a 7 *bar* internal line of air.

During this phase the functioning of the pressure control chain and digital flowmeter response to input by operator are verified. At this point test rig is ready for experimental session.

6.2.2 Strand Preparation

The sample is then prepared using a pyrotechnical charge obtained from an aluminized solid propellant board from which a small cylindrical piece is extracted caring of its dimensions, it must be deep enough to grip the sample internal port under oxidizer flow but not too big to modify the sample behavior at the beginning of combustion.

The pyrotechnical charge is introduced from the smoother side of the sample since this will be recorded by the Photron camera; no bubbles, cuts or curved surface are admitted.

Figure 6.5: HTPB+ 10% Cu sample with pyrotechnical charge.

The primed sample is then pushed into the swirling injector and fixed with two screws, combustion chamber is closed, the two drain pipes are well tightened up as the pipes providing cooling gas and oxidizer gas.

Sealing test begins closing the exhaust valve, spraying water and soap on the seals and opening the pneumatic air valve until maximum reachable pressure is achieved, then closing the pneumatic air valve.

If pressure inside combustion chamber drops there is a leakage; in this case exhaust valve must be opened, all the seals tightened harder and the sealing test repeated.

After reaching the acceptable sealing external air–cooling is activated, then combustion chamber is slowly pressurized with nitrogen. Secondary flows enable combustion chamber pressure to rise till the selected threshold value is reached.

When this happens pressure regulator commands electro-valves thus granting quasi-steady chamber pressure.

At this point the operator starts video acquisition which in turn triggers the flow meter. Then the operator commands laser ignition. Flow meter enables the selected oxidizer mass flow rate to reach the sample while laser beam impinges on primer charge surface igniting it. Energy released by primer charge combustion yields to ignition of the tested strand. From this point burning test proceeds under quasi–steady chamber pressure.

When combustion is finished operator stops oxidizer flow and then nitrogen flow. A by-pass on the dump line excludes electro valves thus enabling combustion chamber discharge. Air is used as secondary flow for combustion chamber cooling. In the meanwhile operator saves data of the performed combustion (recorded video, pressure and flow meter traces) for use in the analysis phase.

6.3. Data reduction: Time Resolved Ballistic

Data reduction is based on the strand central port diameter sampling from recorded video of the burning test. The time-resolved data reduction technique was developed and validated at SPLab [52] [70] [69].

6.3.1. Video Editing

The recorded video can be modified in order to improve visualization quality by editing performed by the freeware software VirtualDub®.

6.3.2. Scale Factor

The calibration scale between pixels of the digital video and millimeters in the real sample must be determined. The scaling factor and diameter sampling are performed by the same software: RedLake Imaging MotionScope CAMERA v.2.3.0. The recorded video with the graph paper sample is used. Real distance of two points on the graph paper is measured from their x-y coordinates. Both horizontal and vertical measurements are used to limit calibration errors. Pixels to length conversion is obtained as ratio between the length in pixel on the image and the effective length in *mm.*

$$cal = \frac{\sqrt{(x_1 - x_2)^2 + (y_1 - y_2)^2}}{5} \quad \textbf{(6.1)}$$

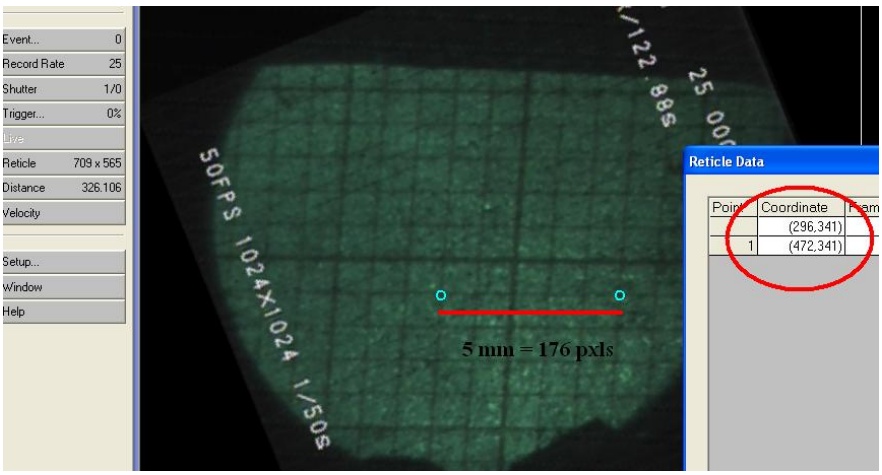

Figure 6.6: Example of calibration scale.

6.3.3. Strand Ignition

Once the calibration equivalence has been determined, the first flame frame t_{ff} and ignition frame $t_{ign,ff}$ must be identified from the video. The former is associated to the time in which the pyrotechnical charge ignition starts at the head-end section of the sample, the latter is the time central port is completely visible at (after primer charge ignition). The t_{ff} and the $t_{ign,ff}$ are used in the earlier phases of the data reduction procedure. The time-resolved technique implemented at SPLab requires the definition of an ad-hoc evaluated $t_{ign,ff}$ (see Paragraph 6.3.4 for further details).

6.3.4. Time-resolved Data

Regression rate measurement is based on a time-resolved technique based on central port diameter sampling in time. The sampling frequency ranges from 1 to 10 Hz, depending on combustion visualization quality and operating conditions. Sampling frequency is higher at the beginning of the run. In a run, the last sampled diameter depends on overall quality of the combustion visualization.

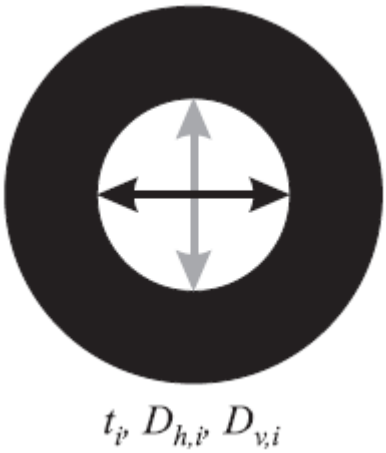

Figure 6.7: Time-resolved quasi-steady regression rate: definition of mean sampled diameter [75].

Starting from $t_{ign,ff}$ each sampled diameter is obtained from measurements over two different radial directions. The average diameter is obtained from 3 vertical and 3 horizontal diameters. Considering Figure 6.1 the space-average diameter at time t_i is given as:

$$\overline{D} = \frac{1}{6}\left(\sum_{i=1}^{3} D_{v,i} + \sum_{j=1}^{3} D_{h,j}\right) \quad \textbf{(6.2)}$$

Multiple diameters measurements allow to define statistical indicators as mean, variance and confidence interval.

Figure 6.8: Example of Vertical diameter sampling, note head-end burning.

During combustion the central port diameter increases in time, due to solid fuel consumption. The sequence of $\overline{D_i}$ vs. t_i is a discrete information in time. A continuous $\overline{D}(t)$ is achieved by power law interpolation of sampled data as hereby shown:

$$\overline{D}(t) - D_0 = a_D(t - t_0)^{n_D}, t \geq t_{ign} \tag{6.3}$$

The power law of Eq.(6.3) is defined for $t \geq t_{ign}$ where t_{ign} is ad-hoc defined for each test. The ad-doc defined t_{ign} value is determined by maximizing the data fitting of Eq. (6.3). Details are given in [76] [52]. A representative result of the definition $\overline{D}(t) - D_0$ is reported in Figure 6.9.

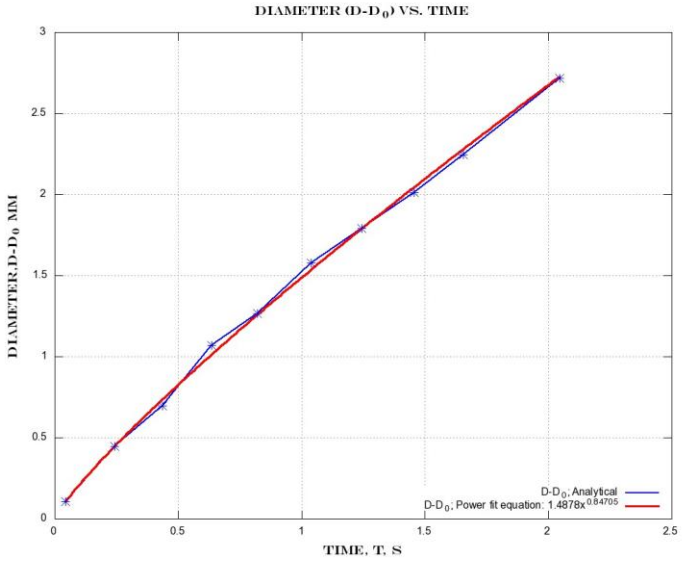

Figure 6.9: $\overline{D}(t) - D_0$ vs. time trend interpolated by power law (HTPB + 10% Al35-Cu65, 210 nlpm, test n°1).

By analytical derivation an expression for the regression rate vs. time relationship can be defined.

$$r_f(t) = \frac{1}{2} a_D n_d (t - t_0)^{n_D - 1}, t \geq t_{ign} \quad \textbf{(6.4)}$$

The other relevant ballistic parameters can be determined according to the following expressions [Eq.(6.5), (6.6) and (6.7)].

Oxidizer mass flux, $G_{ox}(t)$ is defined as the ratio between oxidant mass flow and the instantaneous port area:

$$G_{ox}(t) = 4 \frac{\dot{m}_{ox}}{\pi [D(t)]^2}, t \geq t_{ign} \quad \textbf{(6.5)}$$

Fuel mass flow rate, is defined as:

$$\dot{m}_f(t) = \rho_f r_f(t) A_b(t) = \rho_f r_f(t) L_p \pi \overline{D}(t), t_{ign} > t_0 \quad \textbf{(6.6)}$$

Therefore the oxidizer to Fuel ratio is evaluated as:

$$O/F(t) = \frac{\dot{m}_{ox}(t)}{\dot{m}_f(t)} = \frac{\dot{m}_{ox}(t)}{\rho_f r_f(t) \cdot [D_0 + a_D (t - t_0)^{n_D}]}, t \geq t_{ign} > t_0 \quad \textbf{(6.7)}$$

Behavior of these parameters is shown in the following figures. Data belong to the same ballistic test.

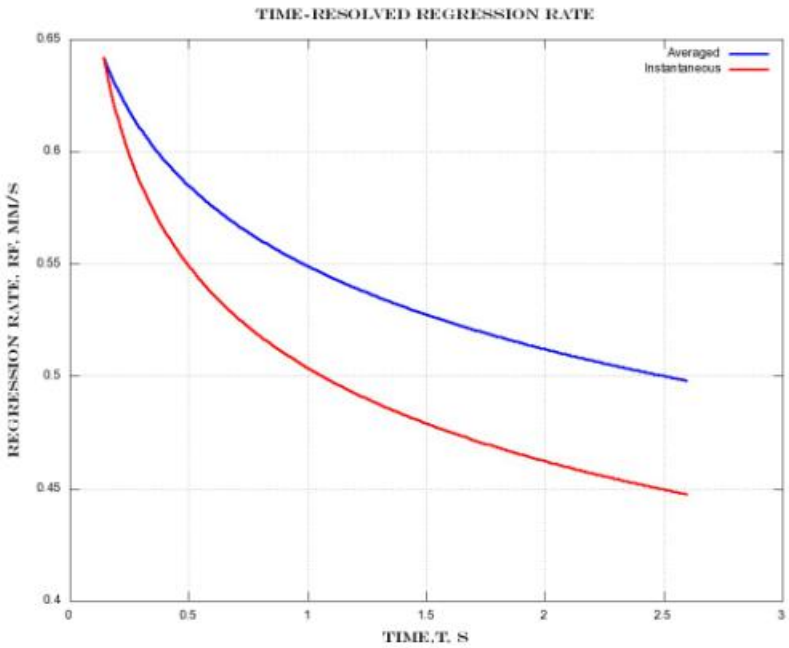

Figure 6.10: r_f vs time (HTPB + 10% Al32-Cu68, 10 bars, 210 nlpm, test n°1).

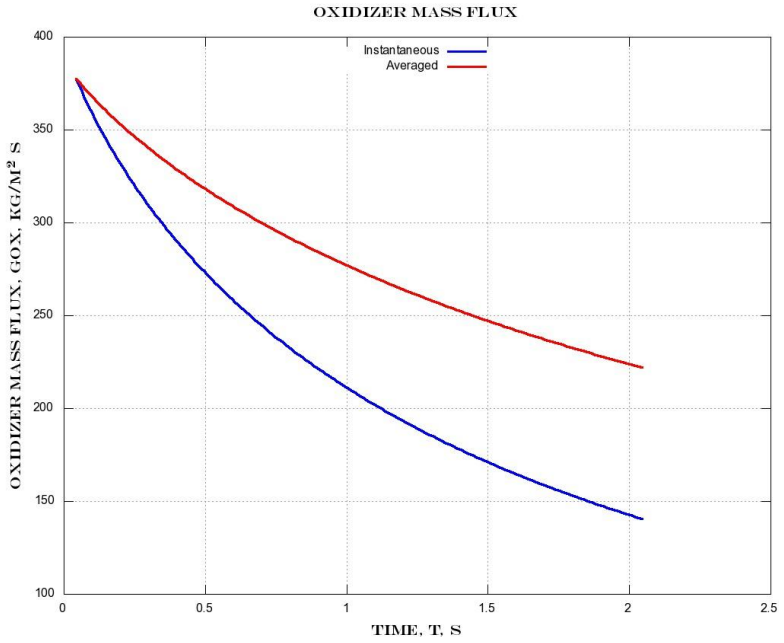

Figure 6.11: G_{ox} trend vs. time trend (HTPB + 10% Al32-Cu68, 10 bars, 210 nlpm, test n°1).

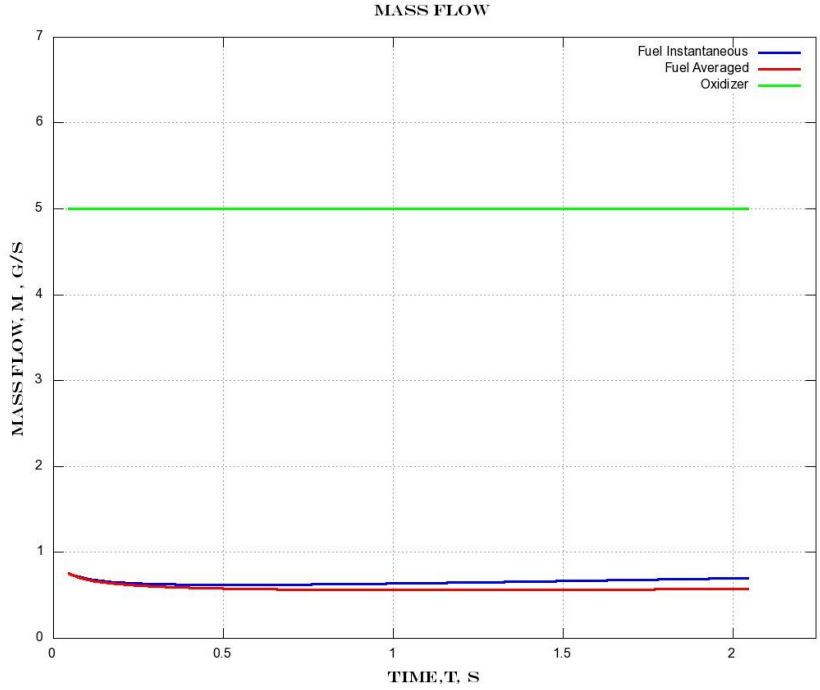

Figure 6.12: Fuel and Oxidizer Mass flows vs. time resolved trend (HTPB + 10% Al32-Cu68, 210 nlpm, test n°1).

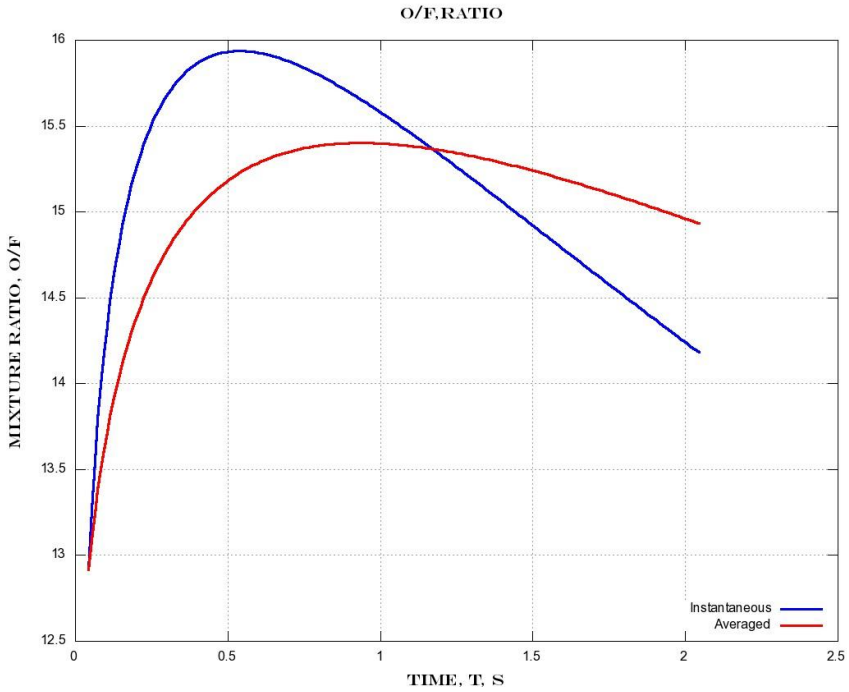

Figure 6.13: O/F ratio trend vs. time(HTPB + 10% Al32-Cu68, 10 bars, 210 nlpm, test n°1).

By numerical derivation is possible to link time and diameter of the central port. Then, from the relationship between oxidizer mass flux and diameter variation, an expression for the fuel regression rate as function of oxidizer mass flux is achieved.

$$r_f(G_{ox}) = \frac{1}{2} a_D n_D \left(\frac{2}{a_D} \sqrt{\frac{\dot{m_{ox}}}{\pi G_{ox}}} - \frac{D_0}{a_D} \right)^{\frac{n_D - 1}{n_D}} \tag{6.8}$$

The resulting behavior is approximated by the commonly used power law expression (eq. 5.8) derived from the Marxman's Model [32] [77] [78].

$$r_f(G_{ox}) = a_r G_{ox}^{n_r} \tag{6.9}$$

The final results for r_f vs. G_{ox} are plotted in Figure 6.14.

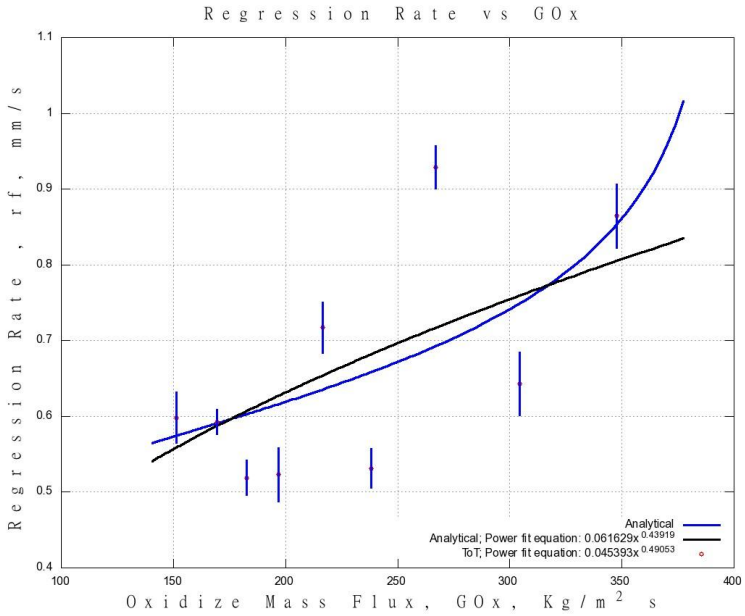

Figure 6.14: Regression rate versus Gox (HTPB + 10% Al32-Cu68, 10 bars, 210 nlpm, test n°1).

Results achieved by time-resolved technique are compared with TOT data in order to gain information on final results consistency between different data reduction techniques. It is worth to notice that these checks are linear, so a possible non satisfaction can be connected to non linear phenomena that can occur during the burning tests.

$$r_f(t_{ign}) = \frac{1}{2} a_D n_D (t - t_0)^{n_D - 1} \quad \textbf{(6.10)}$$

$$< r_f(t_{fin}) > = \frac{1}{t_{fin} - t_{ign}} \int_{t_{ign}}^{t_{fin}} r_f(t) dt \quad \textbf{(6.11)}$$

$$< G_{ox}(t_{fin}) > = \frac{1}{t_{fin} - t_{ign}} \int_{t_{ign}}^{t_{fin}} G_{ox}(t) dt \quad \textbf{(6.12)}$$

For a given fuel formulation, all tests performed under the same operating conditions are collapsed into an ensemble curve Figure 6.15. A power-law approximation of rf vs. Gox is identified by the application of Eq.(6.9). Baseline ensemble is considered for the relative ballistic grading of the considered fuel formulations.

Moreover error bars are defined [79]. In order to evaluate error bars, a proper range of oxidizer mass flux is evaluated. It is necessary to consider Gox limits where curve from all experimental test are defined. Therefore, over this latter interval, error bars are evaluated by confidence interval of fuel regression rate centered in the average value at a given oxidizer mass flux. The confidence level is determined by the resulting standard deviation of experimental data and Student's t parameter. A 95% confidence level is considered in this work.

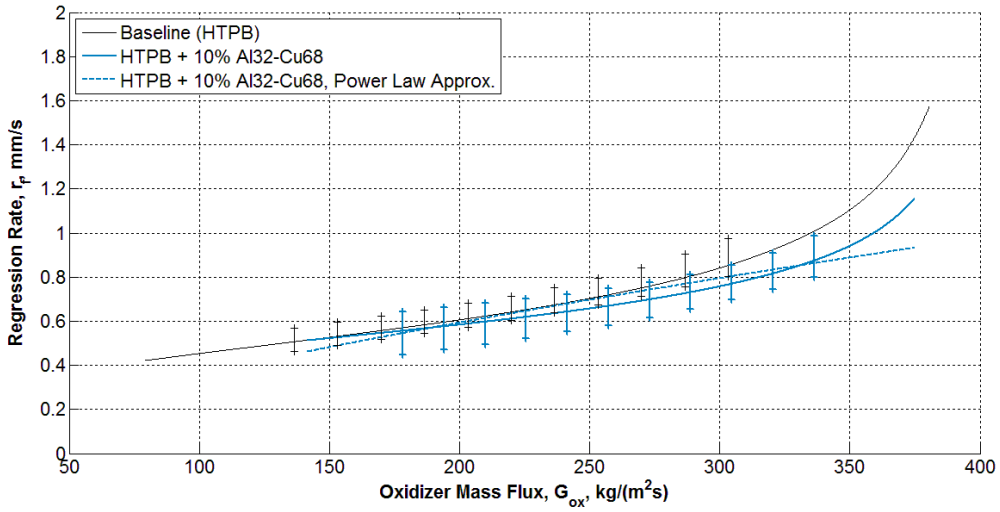

Figure 6.15: Ensamble curve for HTPB + 10% Al32-Cu68 in Gox.

7. Results

In this chapter ballistic characterization results achieved by time-resolved data reduction are presented and discussed. The focus of the investigation is on solid fuel regression rate. The performances of fuel formulations loaded with innovative Aluminum-Copper nano-sized powders are evaluated on a relative grade. Baseline formulation is cured HTPB. Investigated operating conditions are characterized by p_c = 1.0 *MPa*, and m_{ox} = $5 \cdot 10^{-3}$ *kg/s*. The tested HTPB-based fuel formulations contain 10% additive (by mass).

As discussed in Chapter 2, solid fuel r_f depends mainly on G_{ox}. Due to this, for a given solid fuel grain geometry and given operating conditions, the following power-law equation is commonly used in the literature in order to present data:

$$r_f(G) = a_r {G_{ox}}^{n_r} \tag{7.1}$$

Ballistics of loaded formulations is compared to the one of baseline formulations. The percent increase in fuel regression rate $\Delta \boldsymbol{r_{f,\%}}$ is defined as follows:

$$\Delta r_{f,\%} = 100 \frac{r_f - r_{f,baseline}}{r_{f,baseline}} \tag{7.2}$$

In order to calculate variation in terms of fuel mass burning rate a $\Delta \boldsymbol{\dot{m}_{f,\%}}$ is defined:

$$\Delta \dot{m}_{f,\%} = 100 \frac{\dot{m}_f - \dot{m}_{f,baseline}}{\dot{m}_{f,baseline}} \tag{7.3}$$

This parameter is necessary because tested formulation have different densities linked to the metallic composition of powders.

7.1. Ballistic Results

7.1.1. Baseline: HTPB

Cured HTPB is considered as baseline for relative ballistic grading of fuels loaded with nano-sized particles. The ballistic characterization of HTPB burning in G_{OX} was conducted by Paravan and Manzoni [68]. A complete summary of baseline ballistics is hereinafter reported. An overview of baseline ballistics is hereinafter reported. The time-resolved ballistics of baseline formulation is reported in Figure 7.1. In this figure, time runs from right to left. Eight tests were performed, but only the ensemble curve is reported. During the combustion G_{ox} monotonically decreases from the initial to the final value. The baseline parameters for power law approximation of r_f vs. G_{ox} are reported in Table 7.2. Under the investigated conditions an $n_r \sim 0.7$ is achieved. This latter value is in agreement with a convective heat transfer driven combustion, limited by diffusion, as originally observed by Marxman et al. [80]. Data fitting of power-law approximation of time-resolved r_f is relatively low. This result is mainly due to the initial marked value of experimental r_f that is not caught by power-law approximation as originally reported by Evans et al [81] [68]. This behavior is common to all the tested fuels. For the baseline, assuming time-resolved data as reference, the percent difference between this value and r_f evaluated by Eq. (7.1) is 32.5% at G_{ox}(t_ign) = 380 *kg/(m²s)*.

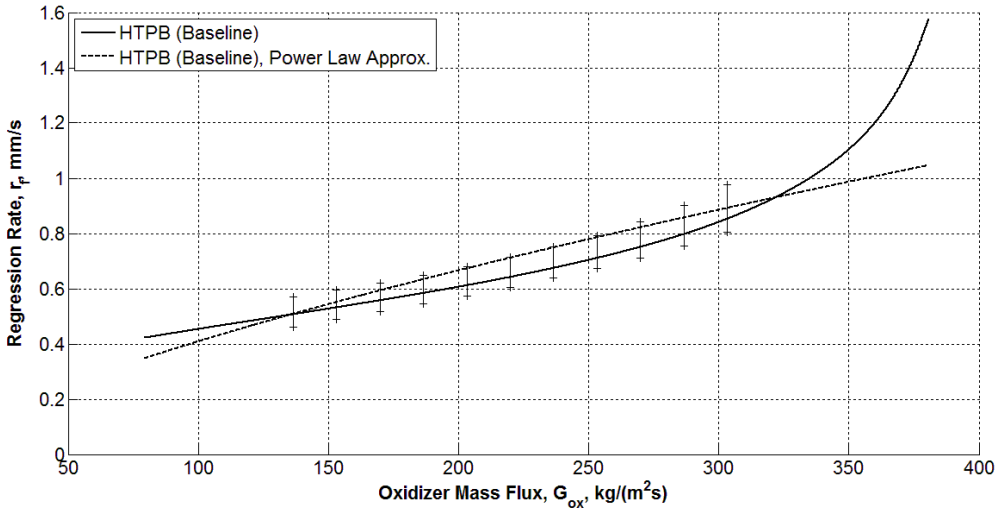

Figure 7.1: Ballistic characterization of HTPB in G_{ox} Initial marked r_f value is followed by monotonic decrease.

Table 7.1: Parameters of Eq. (7.1) of baseline ensemble curve [68]. The n_r value is close to the 0.8 identified in [80].

Fuel Formulation	a_r	n_r	R^2
HTPB	0.016±0.001	0.704±0.003	0.880

7.1.2. HTPB + 10% ALEX™

Hereby ballistic results for HTPB loaded with 10% of ALEX™ are presented. Five tests were performed for this fuel formulation. The resulting ensemble is shown in Figure 7.2. The relevant parameters for power law approx. of r_f vs. G_{ox} are reported. The value of the n_r coefficient (Table 7.16) testifies a strong sensitivity of r_f to G_{ox} changes. This confirms previous results achieved under similar operating conditions [58] [52] [82].

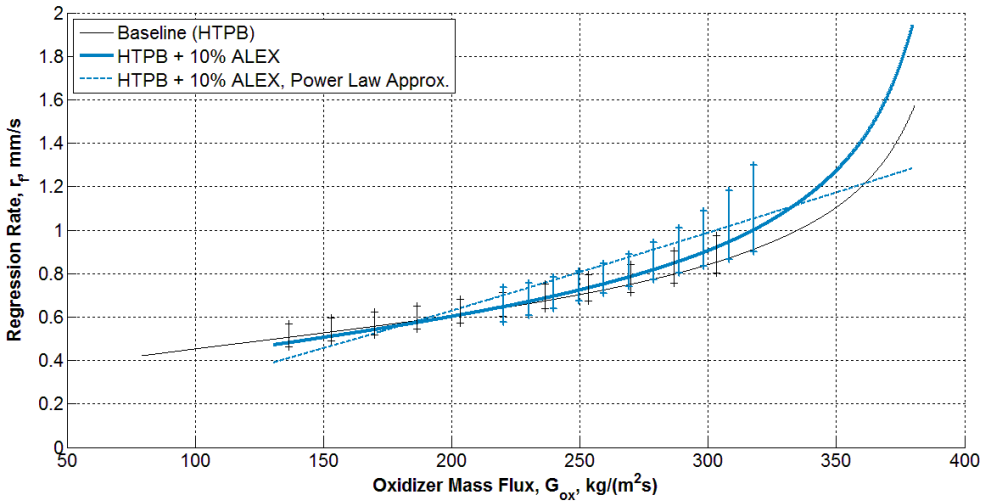

Figure 7.2: Ballistic characterization of HTPB + 10% ALEX™ in G_{ox} .

Relative grading of HTPB + 10% ALEX™ with respect to baseline is reported in Table 7.2. The ALEX™ loaded fuel produces r_f enhancement for G_{ox} > 250 *kg/(m²s)*. Maximum $\Delta r_{f,\%}$ is achieved in the initial phases of the combustion. At G_{ox} = 380 *kg/(m²s)*, a $\Delta r_{f,\%}$= +24.6 % is achieved. Performance of ALEX™ exhibits strong G_{ox} sensitivity, possibly due to subsurface aggregation of particles. Under the investigated conditions, due to the density increase, HTPB + 10% ALEX™ exhibits mass burning rate enhancement over the whole G_{ox} range.

Table 7.2: r_f and mass burning rate percent increases with respect to baseline for HTPB + 10% ALEX™.

G_{ox}	150 *kg/(m²s)*	250 *kg/(m²s)*	350 *kg/(m²s)*
$\Delta r_{f,\%}$	-4.2	2.9	15.2
$\Delta \dot{m}_{f,\%}$	2.6	10.2	23.3

Single test results for ALEX™-loaded fuel show some data scattering among the five performed tests. The ensemble curve for HTPB + 10% ALEX™ for the three of the five performed tests is reported in Figure 7.3. . Resulting ballistic data are reported in Table 7.3. Since production parameters and lot of ALEX™, its storage conditions, and solid fuel manufacturing procedure are common to all the performed tests. Resulting data scattering could be related to proper ALEX™ powder characteristics.

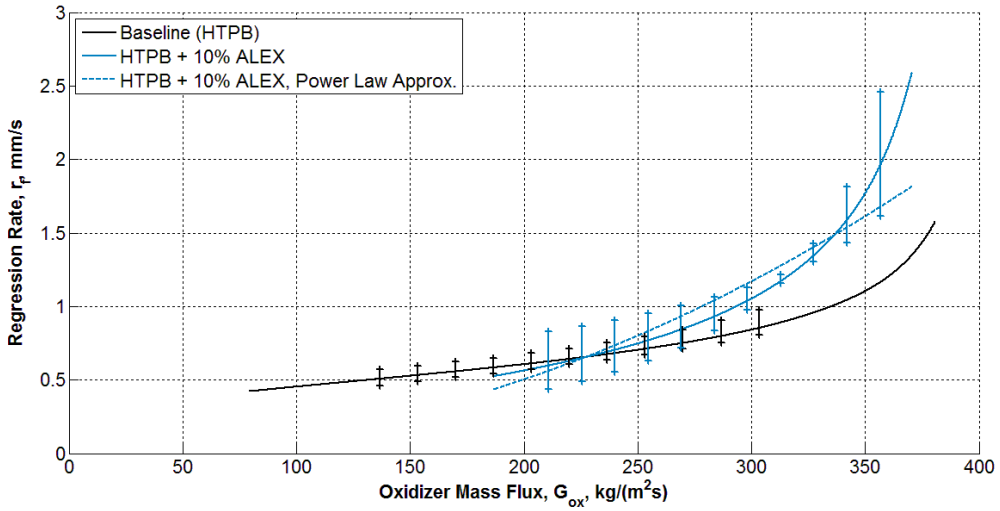

Figure 7.3: Ballistic characterization of HTPB + 10% ALEX™ in G_{ox} (FAST TESTS).

Table 7.3: r_f and mass burning rate percent increases with respect to baseline for HTPB + 10% ALEX™(FAST TESTS).

G_{ox}	150 *kg/(m²s)*	250 *kg/(m²s)*	350 *kg/(m²s)*
$\Delta r_{f,\%}$	N.A.	6.2	60.3
$\Delta \dot{m}_{f,\%}$	N.A.	13.8	71.7

7.1.3. HTPB + 10% ALEX™ Coated

Hereby ballistic results for HTPB loaded with 10% of ALEX™ Coated are presented. Six tests were performed for this fuel formulation. resulting ensemble is shown in Figure 7.4. Power law approximation of r_f vs. G_{ox} is reported in Table 7.16. The coated ALEX™ n_r = 0.609 testifies a lower sensitivity of r_f to G_{ox} changes than both baseline and ALEX™ loaded fuel (n_r = 0.706 and n_r = 1.116 respectively).

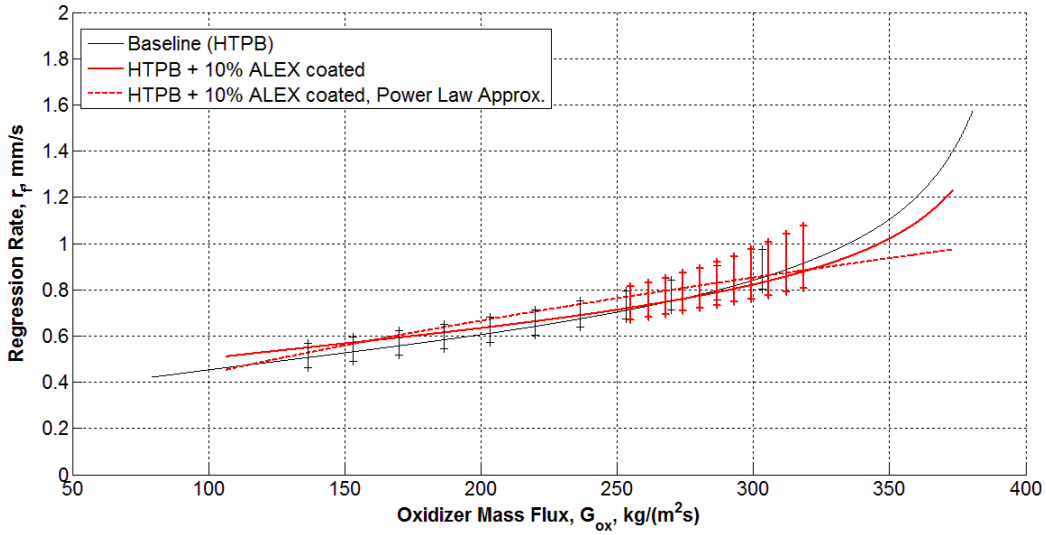

Figure 7.4: Ballistic characterization of HTPB + 10% ALEX™ Coated in G_{ox}.

Relative grading of HTPB + 10% Coated ALEX™ with respect to the baseline is reported in Figure 7.4. The ALEX™ Coated loaded fuel produces r_f enhancement for Gox < 250 *kg/(m²s)*. Maximum $\Delta r_{f,\%}$ is achieved in the last phases of the combustion: for Gox = 105 *kg/(m²s)*, a +10.3 % is achieved. At ignition time the lowest value of $\Delta r_{f,\%}$ is observed: -12.1 %. Under the investigated conditions, due to the density increase, HTPB + 10% ALEX™ Coated shows higher $\Delta \dot{m}_{f,\%}$ with respect to $\Delta r_{f,\%}$ for the same Gox.

Table 7.4: r_f and mass burning rate percent increases with respect to baseline for HTPB + 10% ALEX™ Coated.

G_{ox}	150 *kg/(m²s)*	250 *kg/(m²s)*	350 *kg/(m²s)*
$\Delta r_{f,\%}$	7.4	1.3	-7.7
$\Delta \dot{m}_{f,\%}$	15.1	8.5	-1.1

7.1.4. HTPB + 10% Al85-Cu15

Hereby ballistic results for HTPB loaded with 10% of Al85-Cu15 are presented. Four tests were performed for this fuel formulation, but only ensemble average is reported. The value of the n_r (Table 7.16) testifies a lower G_{ox} sensitivity than baseline. In this case data dispersion is very low, close to baseline one.

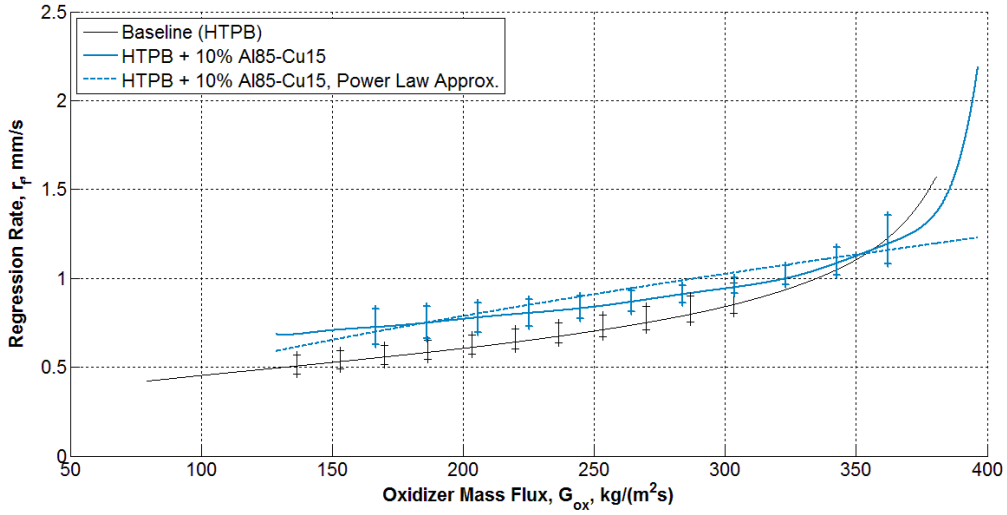

Figure 7.5: Ballistic characterization of HTPB + 10% Al85-Cu15 in G_{ox}.

Relative grading of HTPB + 10% Al85-Cu15 with respect to baseline is reported in Table 7.5. The Al85-Cu15 loaded fuel produces r_f enhancement for G_{ox} < 350 *kg/(m²s)*. Maximum $\Delta r_{f,\%}$ is achieved in the last phases of the combustion: for G_{ox} = 130 *kg/(m²s)*, a +37.7 % is achieved. For G_{ox} = 355 *kg/(m²s)* loaded fuel and baseline have the same fuel regression rate. Under the investigated conditions, due to the density increase, HTPB + 10% Al85-Cu15 exhibits mass burning rate enhancement over the whole G_{ox} range.

Table 7.5: : r_f and mass burning rate percent increases with respect to baseline for HTPB + 10% Al85-Cu15.

G_{ox}	150 *kg/(m²s)*	250 *kg/(m²s)*	350 *kg/(m²s)*
$\Delta r_{f,\%}$	33.7	19.8	0.8
$\Delta \dot{m}_{f,\%}$	43.9	28.9	8.5

7.1.5. HTPB + 10% Al85-Cu15 Coated

Hereby ballistic results for HTPB loaded with 10% of Coated Al85-Cu15 are presented. Three tests were performed for this fuel formulation. The resulting ensemble is shown in Figure 7.6. Power law approximation of r_f vs. G_{ox} is reported in Table 7.16. The $n_r = 0.615$ testifies a lower G_{ox} sensitivity than baseline.

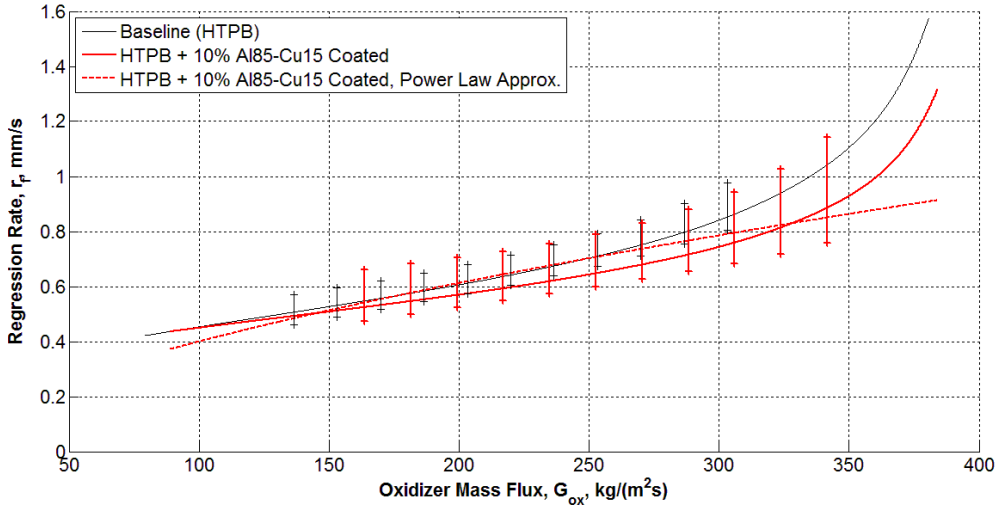

Figure 7.6: Ballistic characterization of HTPB + 10% Al85-Cu15 Coated in G_{ox}.

Relative grading of HTPB + 10% Al85-Cu15 Coated with respect to the baseline is reported in Table 7.6. The Al85-Cu15 Coated loaded fuel produces r_f reduction all over the investigated G_{ox} conditions. Maximum $\Delta r_{f,\%}$ decrease is achieved in the first combustion phase: for $G_{ox} = 380$ kg/(m²s), a -16.5 % is observed. In the last part of combustion doped fuel and baseline have approximately the same r_f. For this fuel formulation, the $\Delta\dot{m}_{f,\%}$ is not sufficient to compensate the r_f reduction with respect to baseline.

Table 7.6: rf and mass burning rate percent increases with respect to baseline for HTPB + 10% Al85-Cu15 Coated.

G_{ox}	150 *kg/(m²s)*	250 *kg/(m²s)*	350 *kg/(m²s)*
$\Delta r_{f,\%}$	-3.6	-8.6	-16.0
$\Delta\dot{m}_{f,\%}$	3.7	-1.7	-9.6

7.1.6. HTPB + 10% Al74-Cu26

Hereby ballistic results for HTPB loaded with 10% of Al74-Cu26 are presented. Three tests were performed for this fuel formulation. The resulting ensemble is shown in Figure 7.7. Power law approximation of r_f vs. G_{ox} is reported in Table 7.16. The Al74-Cu26 n_r = 0.873 testifies a higher G_{ox} sensitivity than baseline. Data dispersion is sensibly higher with respect to baseline, especially at high G_{ox}.

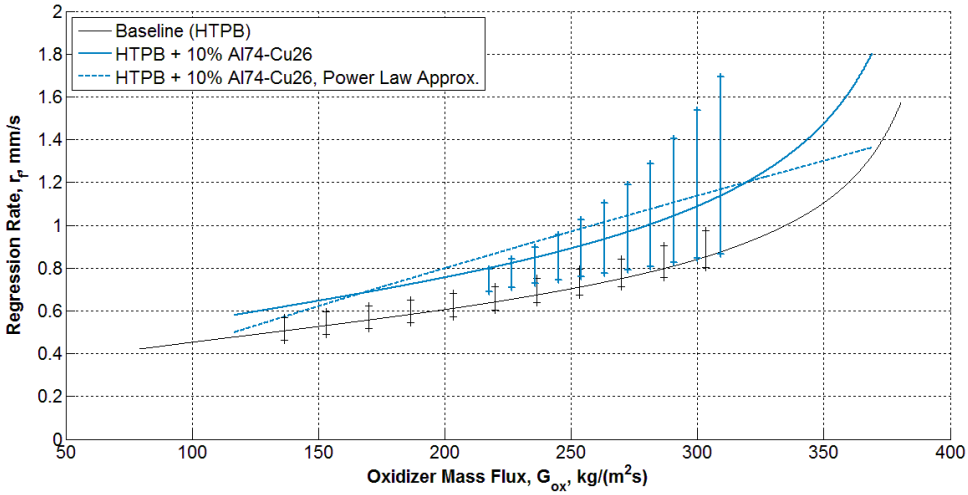

Figure 7.7: Ballistic characterization of HTPB + 10% Al74-Cu26 in G_{ox}.

Relative grading of HTPB + 10% Al74-Cu26 with respect to baseline is reported in Table 7.7. The Al74-Cu26 loaded fuel produces r_f enhancement for all investigated conditions. Maximum $\Delta r_{f,\%}$ is achieved in the first phases of the combustion: for G_{ox} = 370 *kg/(m²s)*, a +35.9 % is achieved. In the last part of combustion doped fuel is still faster than baseline. Under the investigated conditions, due to the density increase, HTPB + 10% Al74-Cu26 exhibits a significant mass burning rate enhancement over the whole G_{ox} range.

Table 7.7: r_f and mass burning rate percent increases with respect to baseline for HTPB + 10% Al74-Cu26.

G_{ox}	150 *kg/(m²s)*	250 *kg/(m²s)*	350 *kg/(m²s)*
$\Delta \dot{r}_{f,\%}$	22.6	26.7	33.5
$\Delta \dot{m}_{f,\%}$	32.2	36.6	43.9

7.1.7. HTPB + 10% Al74-Cu26 coated

Hereby ballistic results for HTPB loaded with 10% of Al74-Cu26 Coated are presented. Four tests were performed for this fuel formulation. The resulting ensemble is shown in Figure 7.8. Power law approximation of r_f vs. G_{ox} is reported in Table 7.16. The value of the $n_r = 0.681$ testifies a lower G_{ox} sensitivity than baseline.

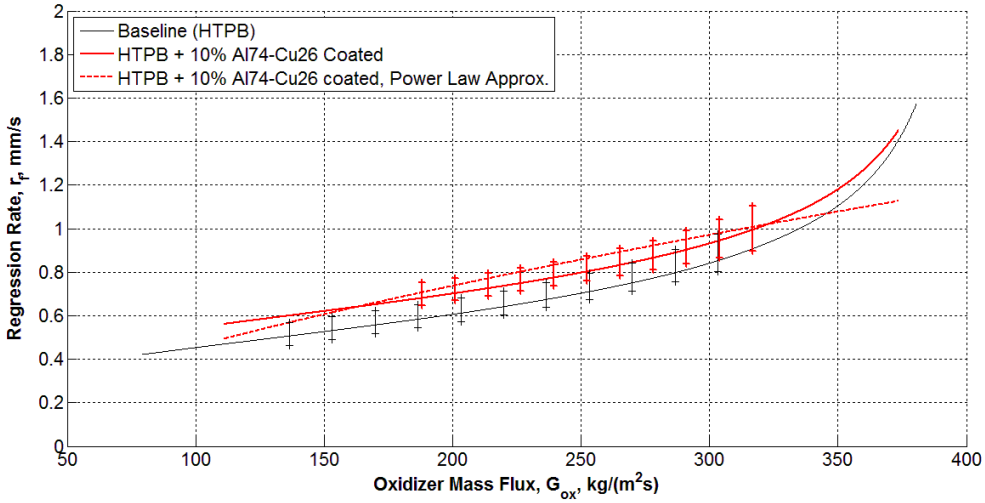

Figure 7.8: Ballistic characterization of HTPB + 10% Al74-Cu26 Coated in G_{ox}.

Relative grading of HTPB + 10% Al74-Cu26 Coated with respect to baseline is reported in Table 7.8. The Al74-Cu26 Coated loaded fuel produces r_f enhancement for all investigated conditions. Maximum $\Delta r_{f,\%}$ is achieved in the last phases of the combustion: for Gox = 110 *kg/(m²s)*, a +19.5 % is achieved. However, in the first part of combustion doped fuel is still faster than the baseline. Under the investigated conditions, due to the density increase, HTPB + 10% Al74-Cu26 Coated exhibits a mass burning rate enhancement over the whole G_{ox} range.

Table 7.8: r_f and mass burning rate percent increases with respect to baseline for HTPB + 10% Al74-Cu26 Coated.

G_{ox}	150 *kg/(m²s)*	250 *kg/(m²s)*	350 *kg/(m²s)*
$\Delta r_{f,\%}$	17.7	13.3	6.8
$\Delta \dot{m}_{f,\%}$	26.9	22.1	15.1

7.1.8. HTPB + 10% Al47-Cu53

Hereby ballistic results for HTPB loaded with 10% of Al47-Cu53 are presented. Four tests were performed for this fuel formulation. The resulting ensemble is shown in Figure 7.9. Power law approximation of r_f vs. Gox is reported in Table 7.16.

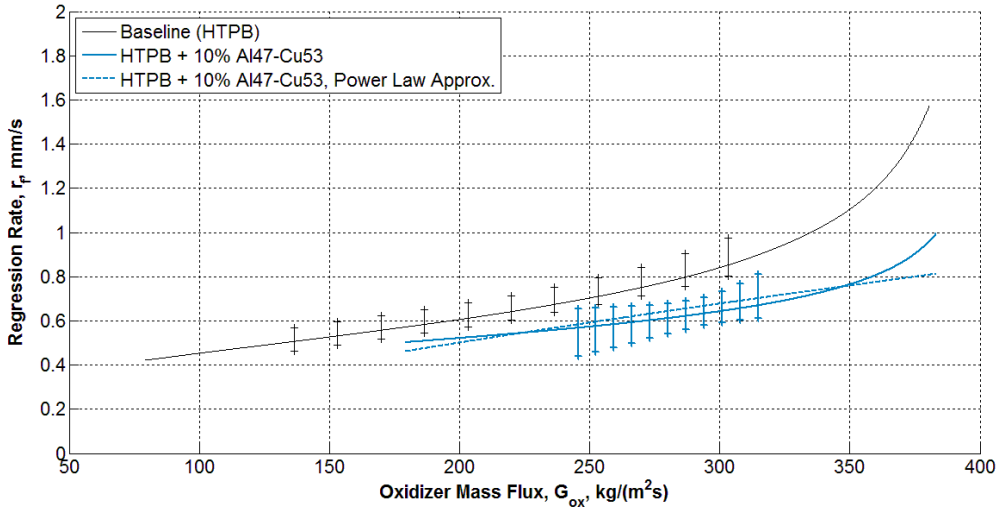

Figure 7.9: Ballistic characterization of HTPB + 10% Al47-Cu53 in G_{ox}.

Relative grading of HTPB + 10% Al47-Cu53 with respect to the baseline is reported in Table 7.9. The Al47-Cu53 loaded fuel produces r_f reductions for all investigated conditions. Maximum $\Delta r_{f,\%}$ reduction is observed in the first phases of the combustion: for Gox = 380 *kg/(m²s)*, a -39.5 % is achieved. Moreover, in the last part of combustion doped fuel is still slower than the baseline. Despite the higher density of metal loaded fuel, the use of Al47-Cu53 produces a significant mass burning rate reduction for all investigated condition with respect to the baseline. Bad quality combustion did not allow calculating regression rate at low oxidizer fluxes. For this reason, $\Delta r_{f,\%}$ and $\Delta \dot{m}_{f,\%}$ for G_{ox} = 150 *kg/(m²s)* is not available.

Table 7.9: r_f and mass burning rate percent increases with respect to baseline for HTPB + 10% Al47-Cu53.

G_{ox}	150 *kg/(m²s)*	250 *kg/(m²s)*	350 *kg/(m²s)*
$\Delta \dot{r}_{f,\%}$	N.A.	-18.5	-30.9
$\Delta \dot{m}_{f,\%}$	N.A.	-11.6	-25.0

7.1.9. HTPB + 10% Al47-Cu53 Coated

Hereby ballistic results for HTPB loaded with 10% of Al47-Cu53 Coated are presented. Six tests were performed for this fuel formulation. The resulting ensemble is shown in Figure 7.10. Power law approximation of r_f vs. G_{ox} is reported in Table 7.16.

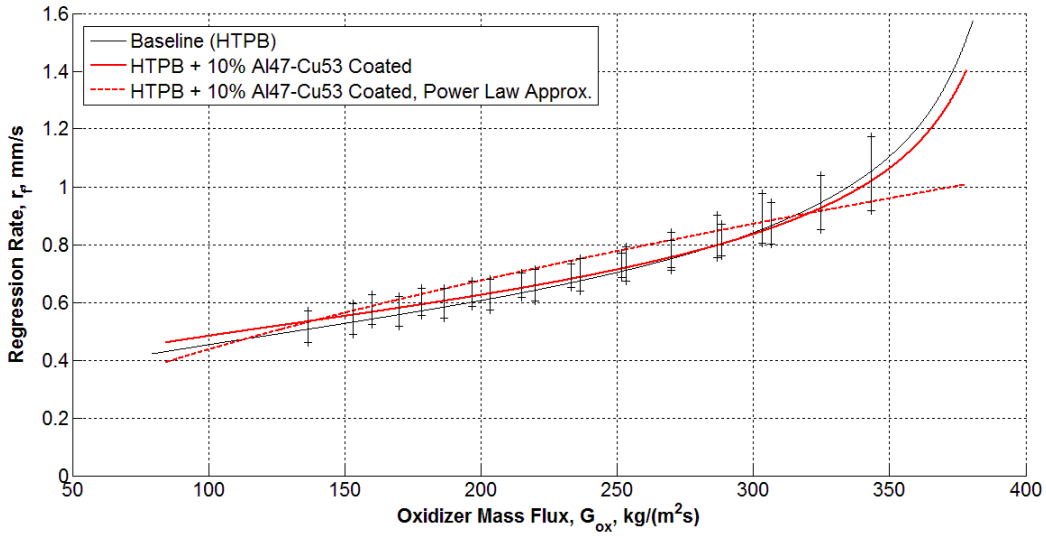

Figure 7.10: Ballistic characterization of HTPB + 10% Al47-Cu53 Coated in G_{ox}.

Relative grading of HTPB + 10% Al47-Cu53 Coated with respect to the baseline is reported in Table 7.10. The Al47-Cu53 Coated loaded fuel produces light r_f variations for all investigated conditions. Maximum $\Delta r_{f,\%}$ is achieved in the last phases of the combustion: for G_{ox} = 84 *kg/(m²s)*, a +7.3 % is achieved. Minimum $\Delta r_{f,\%}$ is observed in the first phases of the combustion: for G_{ox} = 378 *kg/(m²s)*, a -7.2 % is achieved. Mass burning rate for the Al47-Cu53 Coated formulation is higher with respect to the baseline for all investigated conditions.

Table 7.10: : r_f and mass burning rate percent increases with respect to baseline for HTPB + 10% Al47-Cu53 Coated.

G_{ox}	150 *kg/(m²s)*	250 *kg/(m²s)*	350 *kg/(m²s)*
$\Delta \dot{r}_{f,\%}$	6.6	1.4	-3.7
$\Delta \dot{m}_{f,\%}$	13.7	10.0	4.5

7.1.10. HTPB + 10% Al32-Cu68

Hereby ballistic results for HTPB loaded with 10% of Al32-Cu68 are presented. Four tests were performed for this fuel formulation. The resulting ensemble is shown in Figure 7.11. Power law approximation of r_f vs. G_{ox} is reported in Table 7.16.

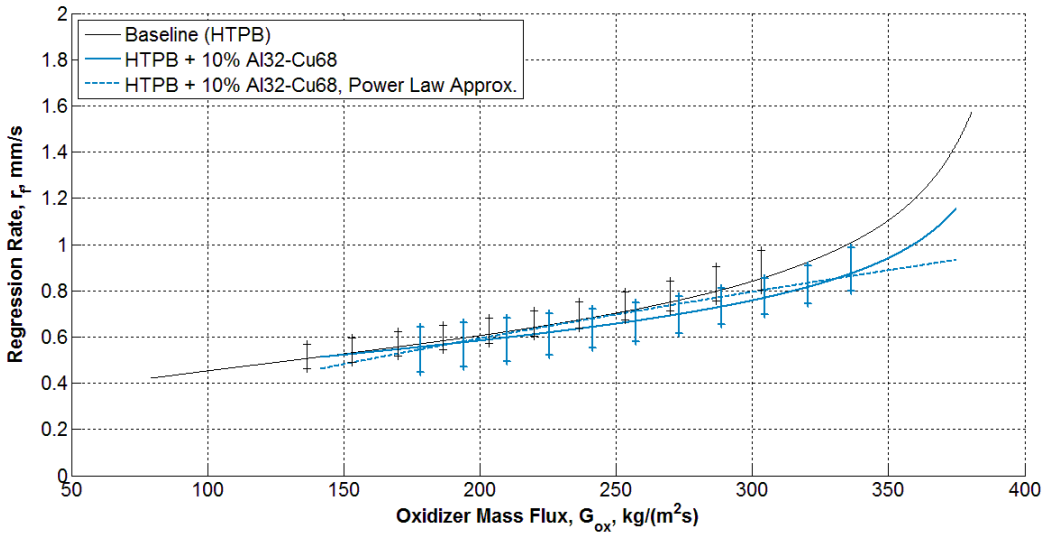

Figure 7.11: Ballistic characterization of HTPB + 10% Al32-Cu68 in G_{ox}.

Relative grading of HTPB + 10% Al32-Cu68 with respect to baseline is reported in Table 7.11. The Al32-Cu68 loaded fuel produces light r_f reductions for all investigated conditions. Minimum $\Delta r_{f,\%}$ is achieved in the first phase of the combustion: for G_{ox} = 375 *kg/(m²s)* , a -19.5 % is achieved. Despite the reduction in r_f, $\Delta \dot{m}_{f,\%}$ at low G_{ox} is positive thanks to the increase of density due to metallic powders addition.

Table 7.11: r_f and mass burning rate percent increases with respect to baseline for HTPB + 10% Al32-Cu68.

G_{ox}	150 *kg/(m²s)*	250 *kg/(m²s)*	350 *kg/(m²s)*
$\Delta \dot{r}_{f,\%}$	-0.9	-6.6	-14.9
$\Delta \dot{m}_{f,\%}$	7.9	1.7	-7.3

7.1.11. HTPB + 10% Al32-Cu68 Coated

Hereby ballistic results for HTPB loaded with 10% of Al32-Cu68 Coated are presented. Five tests were performed for this fuel formulation. The resulting ensemble is shown in Figure 7.12. Power law approx. of r_f vs. G_{ox} is reported in Table 7.16. The value of the n_r = 1.070 testifies a higher G_{ox} sensitivity than Baseline. Increase of n_r value is about 48.7%. Especially for low G_{ox}, data dispersion is small with respect to baseline.

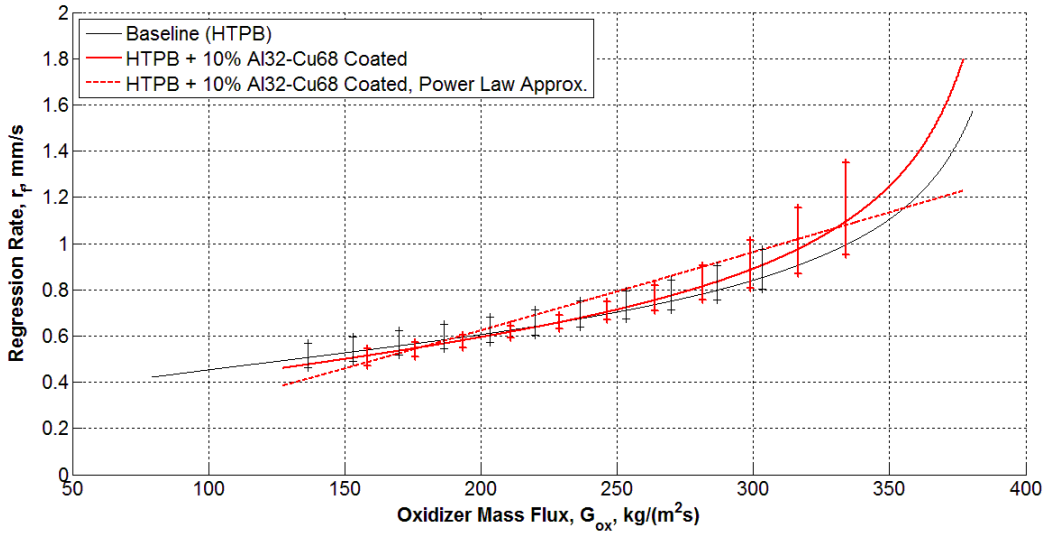

Figure 7.12: Ballistic characterization of HTPB + 10% Al32-Cu68 Coated in G_{ox}.

Relative grading of HTPB + 10% Al32-Cu68 Coated with respect to the baseline is reported in Table 7.12. Maximum $\Delta r_{f,\%}$ is achieved in the first phase of the combustion: for G_{ox} = 375 *kg/(m²s)*, a +21.1 % is achieved. Minimum $\Delta r_{f,\%}$ is observed in the first phase of the combustion: for G_{ox} = 127 *kg/(m²s)*, a -6.3 % is achieved. Al32-Cu68 Coated loaded fuel exhibits mass burning rate enhancements with respect to baseline all over the investigated G_{ox} range.

Table 7.12: r_f and mass burning rate percent increases with respect to baseline for HTPB + 10% Al32-Cu68 Coated.

G_{ox}	150 *kg/(m²s)*	250 *kg/(m²s)*	350 *kg/(m²s)*
$\Delta \dot{r}_{f,\%}$	-5.2	1.46	12.9
$\Delta \dot{m}_{f,\%}$	3.2	10.5	23.0

7.1.12. HTPB + 10% Al15-Cu85

Hereby ballistic results for HTPB loaded with 10% of Al15-Cu85 are presented. Three tests were performed for this fuel formulation. The resulting ensemble is shown in Figure 7.13. Power law approximation of r_f vs. G_{ox} is reported in Table 7.16 . The value of the $n_r = 0.922$ testifies a higher G_{ox} sensitivity than baseline.

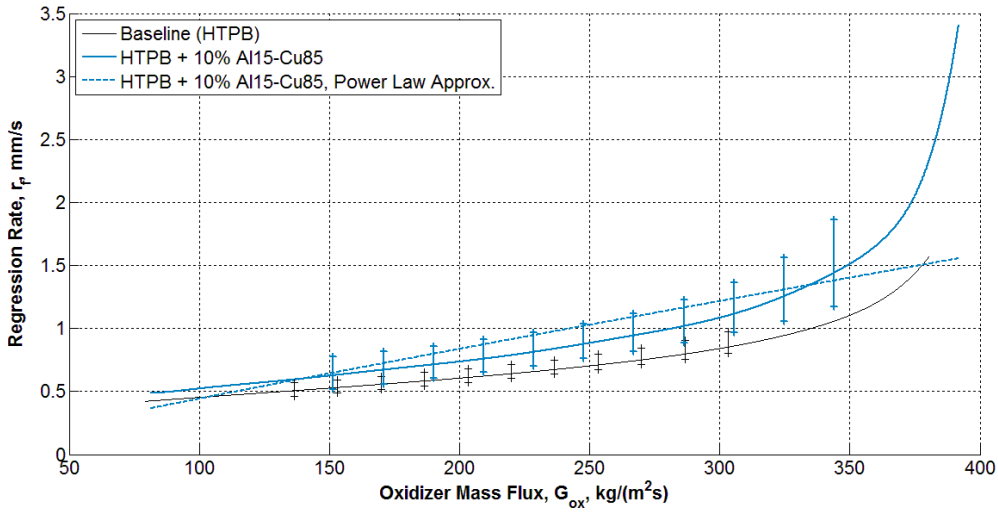

Figure 7.13: Ballistic characterization of HTPB + 10% Al15-Cu85 in G_{ox}.

Relative grading of HTPB + 10% Al15-Cu85 with respect to the baseline is reported in

Table 7.13. The Al15-Cu85 loaded fuel produces high r_f enhancements for all investigated G_{ox} conditions. Maximum $\Delta r_{f,\%}$ is achieved in the first phase of the combustion: for G_{ox} = 380 *kg/(m²s)*, a 48.7 % is achieved. HTPB + 10% Al15-Cu85 fuel exhibits high $\Delta\dot{m}_{f,\%}$ all over the investigated G_{ox} range.

Table 7.13: : r_f and mass burning rate percent increases with respect to baseline for HTPB + 10% Al15-Cu85.

G_{ox}	150 *kg/(m²s)*	250 *kg/(m²s)*	350 *kg/(m²s)*
$\Delta\dot{r}_{f,\%}$	18.4	21.1	36.6
$\Delta\dot{m}_{f,\%}$	29.5	36.9	49.4

7.1.13. HTPB + 10% Al15-Cu85 Coated

Hereby ballistic results for HTPB loaded with 10% of Al15-Cu85 Coated are presented. Five tests were performed for this fuel formulation. The resulting ensemble is shown in Figure 7.14. Power law approximation of r_f vs. G_{ox} is reported in Table 7.16. The value of the n_r =0.499 testifies a significant reduction of G_{ox} sensitivity with respect to baseline.

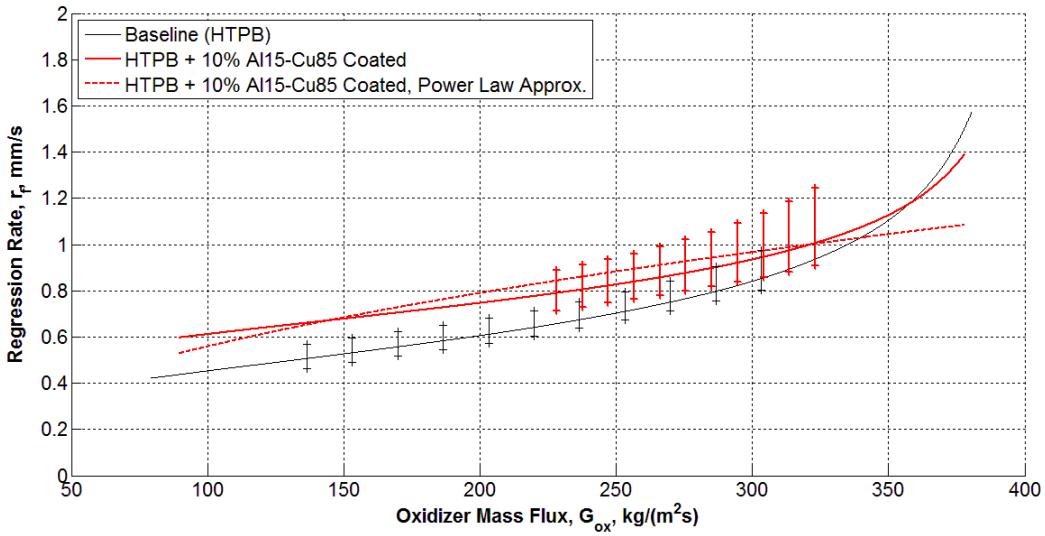

Figure 7.14: Ballistic characterization of HTPB + 10% Al15-Cu85 Coated in G_{ox}.

Relative grading of HTPB + 10% Al15-Cu85 Coated with respect to the baseline is reported in Table 7.14. The Al15-Cu85 Coated loaded fuel produces high r_f enhancements especially at low G_{ox}. Maximum $\Delta r_{f,\%}$ is achieved in the last phase of the combustion: for G_{ox} = 90 *kg/(m²s)*, a 36.3 % is achieved. For the highest investigated G_{ox}, $\Delta r_{f,\%}$a is slightly negative. On the other hand, $\Delta \dot{m}_{f,\%}$ is positive for every investigated G_{ox} because of the increase of fuel density connected to the addiction of metal powders.

Table 7.14: r_f and mass burning rate percent increases with respect to baseline for HTPB + 10% Al15-Cu85 Coated.

G_{ox}	150 *kg/(m²s)*	250 *kg/(m²s)*	350 *kg/(m²s)*
$\Delta \dot{r}_{f,\%}$	34.9	17.5	2.0
$\Delta \dot{m}_{f,\%}$	40.8	28.6	11.6

7.1.14. HTPB + 10% Cu

Hereby ballistic results for HTPB loaded with 10% of Copper are presented. Six tests were performed for this fuel formulation. The resulting ensemble is shown in Figure 7.15. Power law approximation of r_f vs. G_{ox} is reported in Table 7.16 . The value of the n_r =0.505 testifies a lower G_{ox} sensitivity than baseline.

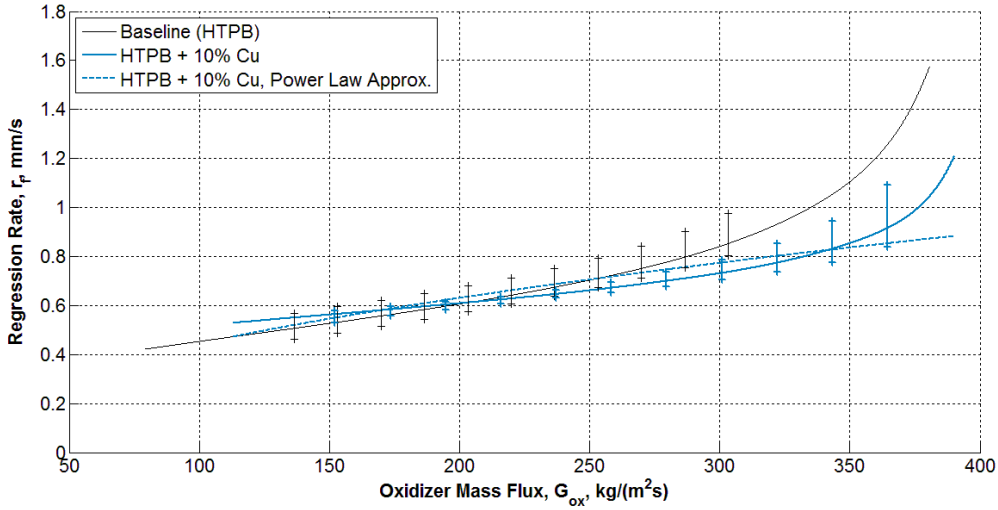

Figure 7.15: Ballistic characterization of HTPB + 10% Copper in G_{ox}.

Relative grading of HTPB + 10% Copper with respect to the baseline is reported in Table 7.14. Maximum $\Delta r_{f,\%}$ is observed in the last phase of the combustion: for G_{ox} = 115 *kg/(m²s)*, a +25.1 % is achieved. Minimum $\Delta r_{f,\%}$ is observed in the first phase of the combustion: for Gox = 115 *kg/(m²s)*, a -34.1 % is achieved. At low G_{ox}, mass burning rate is significantly higher with respect to the baseline. This is due to the high Copper powders density: 8920 *kg/m³*. Nevertheless, for high G_{ox} increase in density is not sufficient to compensate r_f reduction.

Table 7.15: r_f and mass burning rate percent increases with respect to baseline for HTPB + 10% Cu.

G_{ox}	150 *kg/(m²s)*	250 *kg/(m²s)*	350 *kg/(m²s)*
$\Delta \dot{r}_{f,\%}$	6.6	-6.0	-22.8
$\Delta \dot{m}_{f,\%}$	17.1	3.3	-15.2

Table 7.16 : Parameters of Eq. (7.1) of baseline ensemble curve for all investigated formulations.

Fuel	a_r	n_r	R^2
Baseline(HTPB)	0.016±0.001	0.704±0.003	0.880
HTPB+ 10% ALEX™	0.002±0.001	1.116±0.004	0.902
HTPB + 10% ALEX™ Coated	0.026±0.001	0.609±0.001	0.905
HTPB + 10% Al85-Cu15	0.025±0.001	0.651±0.003	0.792
HTPB + 10% Al85-Cu15 Coated	0.023±0.001	0.615±0.002	0.872
HTPB+10% Al74-Cu26	0.008±0.001	0.873±0.002	0.917
HTPB+10% Al74-Cu26 Coated	0.020±0.001	0.681±0.002	0.906
HTPB+10% Al47-Cu53	0.010±0.001	0.745±0.003	0.898
HTPB+10% Al47-Cu53 Coated	0.024±0.001	0.629±0.002	0.888
HTPB+10% Al32-Cu68	0.013±0.001	0.722±0.002	0.911
HTPB+10% Al32-Cu68 Coated	0.022±0.001	1.070±0.003	0.902
HTPB+10% Al15-Cu85	0.006±0.001	0.922±0.004	0.833
HTPB+10% Al15-Cu85 Coated	0.056±0.001	0.499±0.002	0.890
HTPB+10% Cu	0.043±0.001	0.505±0.002	0.850

Table 7.17: r_f and mass burning rate percent increases with respect to baseline(pure HTPB) for all investigated formulations.

Fuel	$\Delta r_{f,\%}$		$\Delta \dot{m}_{f,\%}$	
	150 *kg/(m²s)*	350 *kg/(m²s)*	150 *kg/(m²s)*	350 *kg/(m²s)*
HTPB+ 10% ALEX™	-4.2	15.2	2.6	23.3
HTPB+ 10% ALEX™(Fast Tests)	N.A.	60.3	N.A.	71.1
HTPB + 10% ALEX™ Coated	7.4	-7.7	15.1	-1.1
HTPB + 10% Al85-Cu15	33.7	0.8	43.9	8.5
HTPB + 10% Al85-Cu15 Coated	-3.6	-16	3.7	-9.6
HTPB+10% Al74-Cu26	22.6	33.5	32.2	43.9
HTPB+10% Al74-Cu26 Coated	17.7	6.8	26.9	15.1
HTPB+10% Al47-Cu53	N.A.	-30.9	N.A.	-25.0
HTPB+10% Al47-Cu53 Coated	6.6	-3.7	13.7	4.5
HTPB+10% Al32-Cu68	-0.9	-14.9	7.9	-7.3
HTPB+10% Al32-Cu68 Coated	-5.2	12.9	3.2	23.0
HTPB+10% Al15-Cu85	18.4	36.6	29.5	49.4
HTPB+10% Al15-Cu85 Coated	34.9	2.0	40.8	11.6
HTPB+10% Cu	6.6	-22.8	17.1	-15.2

7.2. Discussion

In this section the previously presented ballistic data are discussed. Focus of the discussion will be on Cu concentration and coating effects on r_f and G_{ox} sensitivity. Composite Al-Cu powders were preliminary characterized in terms of composition in [6]. Fluorohydrocarbon-based powder coating effects on powder characteristics and fuel ballistics are investigated in [50] [51]. In spite of this, no detailed investigation on Fluorel™ + Telomer n5 is available in the open literature.

7.3.1. Effects of Powder Composition

Data concerning tested uncoated metal powders are reported in Figure 7.16.

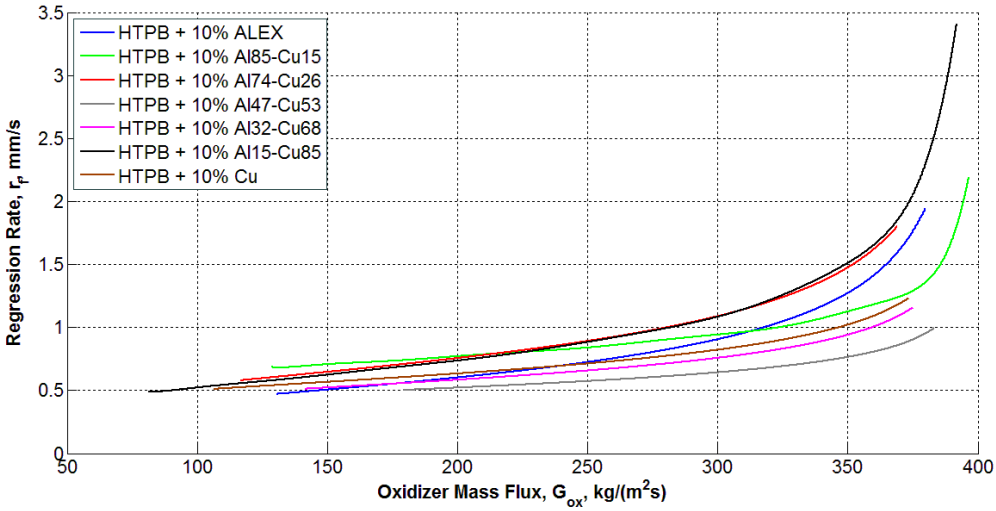

Figure 7.16: Ballistic characterization of all investigated fuels in G_{ox}. Error bars are not reported to improve readability.

The results for the relative ballistic grading of Al-Cu loaded fuels with respect to HTPB baseline was reported in previous section. Here, in order to evaluate the Cu effects on performance enhancement of composite nano-sized powders, HTPB+10% ALEX™ is chosen as reference formulation. Relative ballistic grading between ALEX™ loaded fuel and the Al-Cu loaded formulations is presented in Table 7.18. Parameters $\Delta r_{f,\%}$ and $\Delta \dot{m}_{f,\%}$ are defined according to Eq. (7.2) and Eq. (7.3), with ALEX™ loaded fuel as baseline.

Table 7.18: r_f and mass burning rate percent increases with respect to HTPB + 10 % ALEX™.

Metal Additive	$\Delta r_{f,\%}$		$\Delta \dot{m}_{f,\%}$	
	150 *kg/(m²s)*	350 *kg/(m²s)*	150 *kg/(m²s)*	350 *kg/(m²s)*
Al85-Cu15	39.5	-12.4	43,1	-12.0
Al74-Cu26	28.0	15.9	28.8	16.7
Al47-Cu53	N.A.	-40.0	N.A.	-39.2
Al32-Cu68	3.4	-26.1	5.1	-24.3
Al15-Cu85	23.5	18.6	26.2	21.1
Copper	11.3	-33,0	14.1	-31.3

According to the data reported in Table 7.18, ballistic performance of Al-Cu loaded fuels do not exhibit a clear trend as Cu mass fraction changes. This can be due to the non-uniform formation of intermetallic compounds during EEW process [6]. Aluminum and Copper can create intermetallic compounds when condensed once simultaneously exploded under EEW conditions. At least of two types of intermetallic components (Al_2Cu and Al_4Cu_9) can be created. These materials, can exhibit mechanical and thermal proprieties completely different with respect to the original metals [7]. The available studies on intermetallic compounds reports their chemical and physical variability [66]. Moreover, production of composite bimetallic powders changes not only the materials inside particles but also particle structures. Considering Al-Cu powders, a higher concentration of copper is expected on the surface/subsurface layer of particle [6].

Under the investigated conditions, two powders offer enhanced performance with respect to the ALEX™-loaded fuel over the whole investigated range. The HTPB loaded with Al74-Cu26 and the formulation with Al15-85 provide significant performance enhancement in the earlier as well as in the last part of the combustion. The best performance in terms of $\Delta r_{f,\%}$ at high fluxes is achieved by HTPB + 10% Al15-Cu85. With a G_{ox} = 350 *kg/(m²s)* a $\Delta r_{f,\%}$ = +18.6% characterizes this formulation. Regression rate enhancement of this solid fuel slightly increases as oxidizer mass flux decreases (see Table 7.18). In spite of the great difference in copper concentration in the powder, performance of Al74-Cu26 loaded fuel are close to HTPB + 10% Al15-Cu85. Performance

of the latter fuel formulation is particularly attractive for low G_{ox} values. Under the investigated conditions, HTPB + 10% Al15-Cu85 provides a $\Delta r_{f,\%}$ = +23.5 % at G_{ox} = 150 *kg/(m²s)*. The best performance for the low G_{ox} range is achieved by HTPB + 10% Al85-Cu15.

The HTPB + 10 % Al32-Cu68 and HTPB + 10% Cu formulations are lightly faster than Baseline for low G_{ox} conditions, but exhibits significant fuel regression rate reductions in the earlier phases of the combustion. The poorest performance are achieved by HTPB + 10% Al47-Cu53. This r_f of this fuel is always lower than the reference formulations as testified by data reported in Table 7.18. For this fuel formulation, a poor visualization limits diameter sampling in time, thus yielding to diameter low diameter sampling frequency. Under the investigated conditions, metal additives containing Cu less sensitive than ALEX™-loaded fuel to oxidizer mass flux changes. While regression rate enhancement is crucial for the development of HREs, strong G_{ox} sensitivity is a possible drawback for applications since it is related to performance shift. The lowest sensitivity to oxidizer mass flux changes is exhibited by Cu-loaded fuel.

Table 7.19: n_r values for uncoated investigated formulations.

Metal Additive	n_r
ALEX™	1.116
Al85-Cu15	0.651
Al74-Cu26	0.873
Al47-Cu53	0.745
Al32-Cu68	0.722
Al15-Cu85	0.922
Cu	0.505

A better understanding of the ballistic behavior of Al-Cu loaded formulations can be achieved matching burning data with results of DSC-TGA data of powders (see Chapter 4). The investigated Al-Cu powders present an oxidation onset temperature depending on Cu content. This temperature decreases as Cu concentration increases. On the other hand, possible energy release during combustion decreases because Cu oxidation is less energetic than the one of Al.

The fuels exhibiting the best performance are loaded with Al15-Cu85 and Al74-Cu26 powders. In both cases oxidation onset temperature of powders was lower than the

corresponding value for ALEX™ (see Table 4.8). The Al74-Cu26 powder exhibits an oxidation peak at 531.4°C with a maximum heat flux of 50.7 *W/g*. ALEX™ powder, under the same operating conditions, shows an oxidation peak at 586.8 °C with a maximum heat flow of 51.0 *W/g*. In this case, Al74-Cu26 exhibits the same maximum heat flow per gram of ALEX™, while peak temperature is sensibly reduced. On the other hand Al15-Cu85 powder exhibits a behavior that is really different from the one of ALEX™. The maximum heat flow is lower (16.4 *W/g* vs. 51.0 *W/g*) than ALEX™, but decrease in oxidation onset temperature is more than 200°C. For Al15-Cu85 oxidation peak temperature is 348.2 °C. In spite of differences in the heating rate of DSC-TGA experiments and solid fuel burning, the differences in powder behavior evaluated by calorimetric analyses can affect solid fuel ballistics.

Solid fuel grain regression rate enhancement seems to be related to oxidation onset and peak temperature. Nevertheless, maximum heat flow per gram has a great importance too. Lower ignition temperature means enhanced reactivity, while high heat flow is crucial for energy feedback toward the regressing surface.

7.3.2. Effects of Coating

Produced powders were realized in two variants: uncoated and coated. The coating is realized with Fluorel™ + Telomer n5 (see details given in Chapter 4, Section 4.2.3). The coating effects on ballistics of the solid fuel are hereinafter discussed. For a given powder composition, relative grading of the ballistics of the coated variant will be discussed with respect to the performance of the formulation loaded with the uncoated powder. Therefore, in this part of the investigation a baseline is defined for every tested additive. Since applied coating is in general a very thin layer [83], TMDs of coated and non coated particles are assumed equal. Thus, the $\Delta r_{f,\%}$ and the $\Delta \dot{m}_{f,\%}$ of a given fuel formulation are equal.

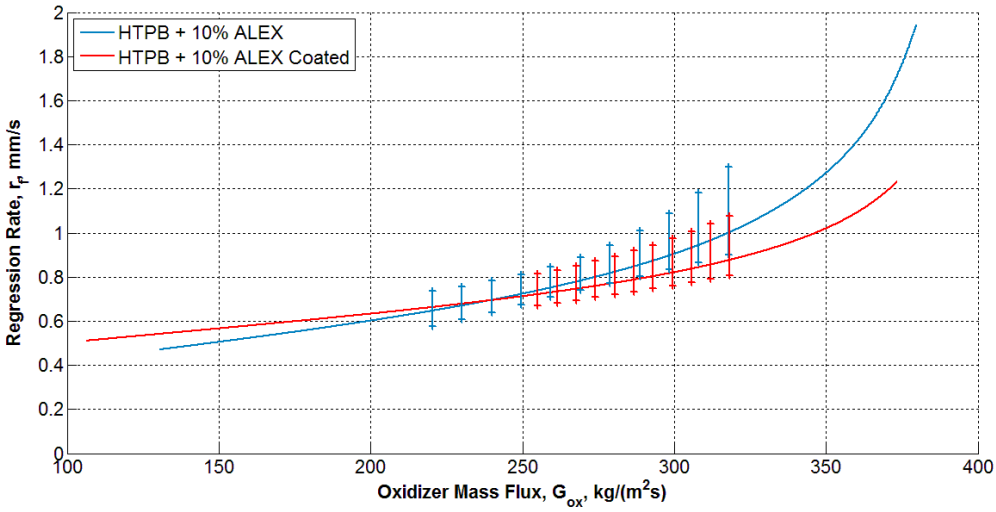

Figure 7.17: Ballistic characterization of HTPB + 10% ALEX™ Coated and Uncoated in G_{ox}.

In ALEX™ loaded fuels, coating causes a general decrease in r_f for G_{ox} > 250 *kg/(m²s)*, see Figure 7.17. In the earlier phases of the test fuel formulation loaded with coated powder exhibits a lower r_f than HTPB + 10% ALEX™. With G_{ox} = 375 *kg/(m²s)*, a $\Delta r_{f,\%}$ = -29.2 % is achieved. On the other hand, for G_{ox} < 250 *kg/(m²s)*, combustion of coated powders loaded fuel presents a faint performance enhancement with respect to the considered baseline. With G_{ox} = 130 *kg/(m²s)* a $\Delta r_{f,\%}$ = +16.0 % is achieved. Coated powders fuel exhibits a lower influence from G_{ox}, as testified by the smaller n_r value (see Table 7.16). All these observations can be related to DSC-TGA data. Thermal analyses reveal that coated ALEX™ is characterized by a lower reactivity than ALEX™. The oxidation onset temperature and the first oxidation peak are shifted toward higher temperature when fluorinated coatings are used [50] [51]. Hindering the powder reactivity, coating can cause the performance detriment observed in the earlier phases of the combustion. On the other hand, coating decomposition products, containing oxidizing species, can produce regression rate enhancement for relatively low oxidizer mass fluxes [52].

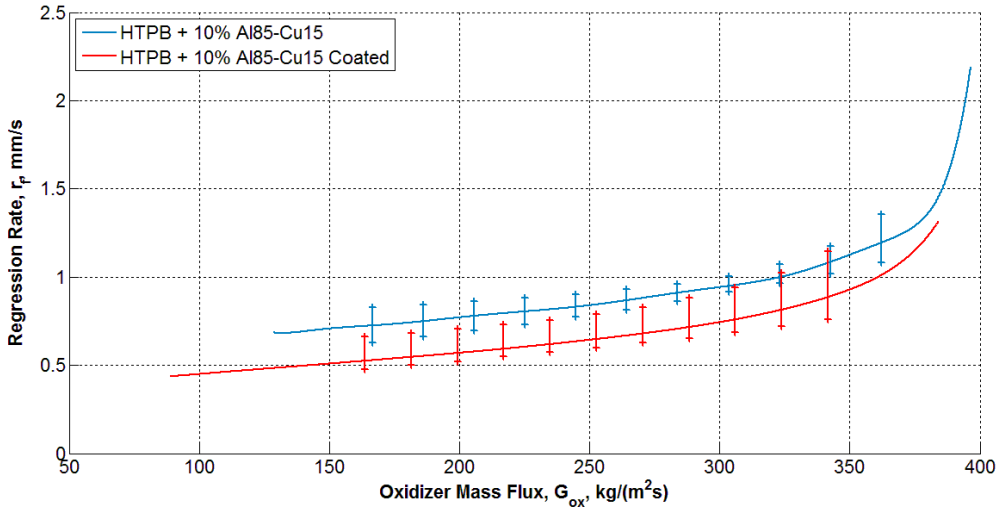

Figure 7.18: Ballistic characterization of HTPB + 10% Al85-Cu15 Coated and Uncoated in G_{ox}.

In Al85-Cu15 loaded fuels, coating reduces fuel r_f over the whole investigated G_{ox} range, see Figure 7.18. Minimum performance detriment is achieved in the earlier phases of the combustion. With G_{ox} = 130 *kg/(m²s)* a $\Delta r_{f,\%}$ = -29.5 % is recorded. In spite of this, G_{ox} sensitivity of the coated powder is lower than the corresponding uncoated powder value, as testified by the value of n_r exponent reported in Table 7.16.

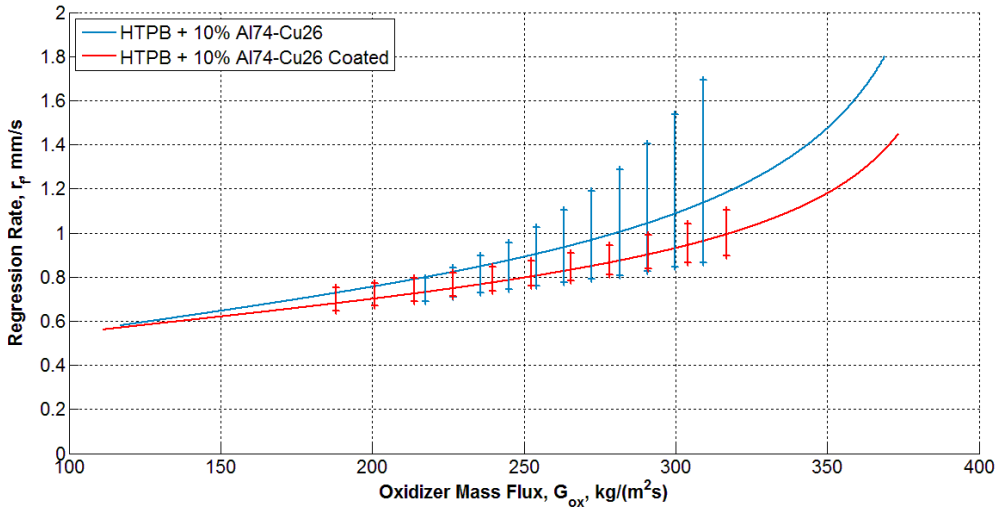

Figure 7.19: Ballistic characterization of HTPB + 10% Al74-Cu26 Coated and Uncoated in G_{ox}.

The coated Al76-Cu24 loaded fuel is characterized by a general r_f decrease with respect to baseline, see Figure 7.19. On the other hand coated powders loaded fuel, exhibits a

weaker G_{ox} influence on r_f. The solid fuel formulation loaded with coated powders exhibits a reduced data scattering than the uncoated counterpart.

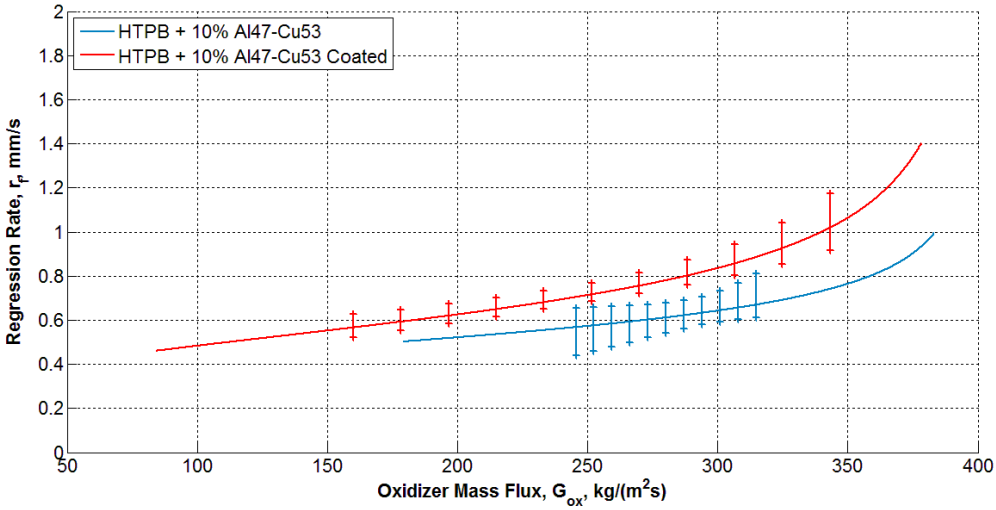

Figure 7.20: Ballistic characterization of HTPB + 10% Al47-Cu53 Coated and Uncoated in G_{ox}.

In contrast to the previous formulations, for Al47-Cu53 loaded fuels, coating significantly increases regression rate over the whole investigated range. Maximum $\Delta r_{f,\%}$ is achieved for G_{ox} = 380 *kg/(m²s)* with a 50 % increase. Solid fuel loaded with coated particles exhibits a weaker G_{ox} influence on r_f. Combustion of HTPB + 10% coated Al47-Cu53 presents higher combustion uniformity than the uncoated counterpart.

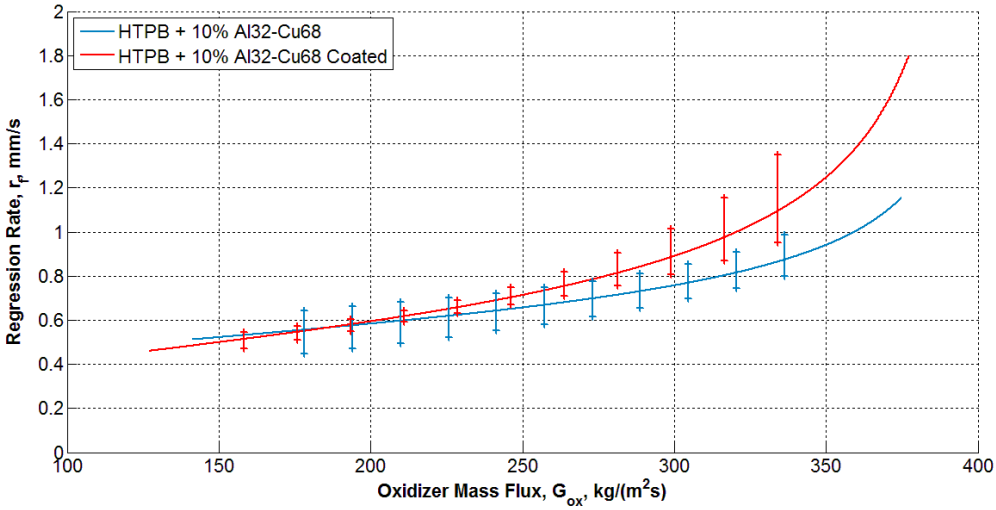

Figure 7.21: Ballistic characterization of HTPB + 10% Al32-Cu68 Coated and Uncoated in G_{ox}.

Ballistic behavior of coated Al32-Cu68 loaded fuels is reported in Figure 7.21. Achieved data present a performance enhancement for G_{ox} > 200 *kg/m²s*. Maximum $\Delta r_{f,\%}$ is

achieved at ignition: G_{ox} = 380 *kg/(m²s)* corresponds to 48.6 % increase. For G_{ox} < 200 *kg/(m²s)*, performance of the fuels loaded with uncoated and coated Al32-Cu68 are almost identical. This is the only case in which, under the investigated conditions, coating fuel is more sensible to the influence of G_{ox} than the uncoated one.

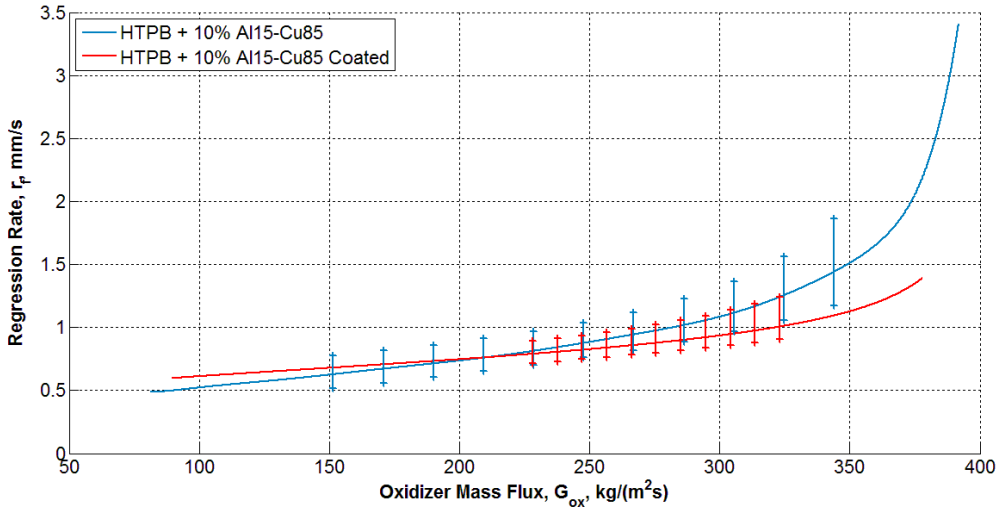

Figure 7.22: Ballistic characterization of HTPB + 10% Al15-Cu85 Coated and Uncoated in G_{ox}.

The performance of HTPB + 10% coated Al15-Cu85 do not present significant performance enhancement. Moreover, for G_{ox} > 250 *kg/(m²s)* performance of Fluorel™ + Telomer n5 coated powders are lower than the uncoated counterpart. At ignition, Gox = 370 *kg/(m²s)*, with a -33.4 % performance detriment. In this specific case, introduction of coating have the great advantage to significantly limit influence of G_{ox} on fuel regression rate. This behavior is testified by the big differences in n_r values between uncoated and coated variants.

Figure 7.20: Percent r_f increase with respect to corresponding uncoated powder for tested Al-Cu powders loaded fuels.

Fuel	$\Delta r_{f,\%}$		
	150 *kg/(m²s)*	250 *kg/(m²s)*	350 *kg/(m²s)*
HTPB + 10% ALEX™ Coated	12.1	-1.6	-19.8
HTPB + 10% Al85-Cu15 Coated	-27.9	-23.7	-16.7
HTPB + 10% Al74-Cu26 Coated	-4.0	-10.6	-20.0
HTPB + 10% Al47-Cu53 Coated	N.A.	24.4	39.2
HTPB + 10% Al32-Cu68 Coated	-4.3	8.7	32.7
HTPB + 10% Al15-Cu85 Coated	13.0	-4.3	-26.2

In general, particle coating by Fluorel™ + Telomer n5 reduces the G_{ox} sensitivity of the regression rate. An exception is given by HTPB loaded with coated Al32-Cu68. Coated powders effects on the regression rate depends on formulation details. The fuel formulation based on HTPB loaded with coated Al85-Cu15 exhibits a reduced r_f over the whole investigated range. Fluorel™ and Telomer n5 coating provides performance gains for Al47-Cu53 and Al32-Cu68 loaded fuels. The effects of coating on the regression rate of HTPB loaded with Al47-Cu53 completely change the combustion behavior of the formulation. With uncoated powders, sample head-end is interested by an intense combustion and central port presents strong anisotropies. This behavior significantly lowers quality of burning visualization. Using coated powders, a regular combustion during all test and excellent burning visualization were achieved.

In order to explain this behavior it is possible to consider effect of coating from two different points of view. Literature data show that introduction of coating usually reduces the specific surface of particles [58], due to an increase in mean particle size. The latter is due to the clustering of particles when coating is applied. On the other hand, decomposition of fluoropolymer coating produces fluorine based oxidizing species. In case of high reactivity powders, increase in specific surface could overcome benefits due to decomposition of coating, at least at high oxidizer fluxes. This lowers fuel regression rate at high G_{ox}. For low oxidizer flux values, coating decomposition enables oxidizing species to be delivered close to the regressing surface. Thus, the drawbacks related to a reduced specific surface of particles are overcome by the performance gain due to oxidizing species availability. This effects can explain also the general decrease in G_{ox} sensitivity characterizing fuels loaded with coated particles.

8. Conclusions and Future Developments

8.1. Conclusions

In this work innovative nano-sized composite Al-Cu powders were produced, characterized and tested as additives in solid fuel formulations for hybrid propulsion. The work is inserted in the studies on hybrid propulsion of the Aerospace Propulsion Laboratory (SPLab) of Politecnico di Milano. Focus of the investigation is the regression rate enhancement of solid fuel formulations.

The Al-Cu powders were produced by EEW at the Institute of Strength Physics and Materials Science and at the Department of Technical Physics of Tomsk State University, Tomsk, Russia. Several types of powders were produced in order to evaluate composition and coating effects. Copper mass fraction in the starting exploding wire ranged from 0% to 100%. The produced powders were passivated in air after production. The effects of coating by Fluorel™ + Telomer n5 on particle characteristics and oxidation/burning behavior was investigated by comparing coated powders with uncoated counterparts. The uncoated nano-sized Aluminum (ALEX™), produced by EEW starting from 100 % Al wire , is a promising additive for solid fuel loading. It is undergoing extended investigation at international level. Nowadays no detailed information about Al-Cu nanopowders combustion behavior is available in literature.

The produced powders were extensively characterized in the pre-burning phase by SEM, TEM, DSC-TGA and particle size distribution. Calorimetric analyses shown marked shift in oxidation onset temperature and oxidation peak due to Cu addition. Under DSC-TGA operating conditions, Copper reduces oxidation onset temperature of the composite powder. The achieved reduction is stronger for increasing Cu mass fraction in the composite powder. This suggest Al-Cu powders can exhibit lower oxidation onset temperature than conventional nano-sized Al. In spite of this, heat flux from the powder during oxidation can be reduced by the presence of Cu.

Tested solid fuels were based on HTPB loaded with 10 % additive (by mass). A dedicated procedure for additive dispersion into solid fuel matrix was used for the manufacturing phase. Combustion tests were performed using GOX as oxidizer, under combustion chamber pressure of 1.0 MPa and initial oxidizer mass flux (G_{ox}) of ~390 kg/(m^2s). Non-loaded, cured HTPB was considered as baseline for the relative grading of the loaded fuel formulations. A time-resolved technique for regression rate was implemented for data reduction. With this technique, a single test can provide a complete r_f vs. G_{ox} characterization.

Ballistic characterization of HTPB + 10% Al74-Cu26 and HTPB + 10% Al15-Cu85 show good overall performance. In first phases of the combustion, with G_{ox} = 350 kg/(m^2s), $\Delta r_{f,\%}$ is +33.5% for the first fuel formulation and +36.6 % for the second. These two formulations are characterized by significant performance gains at G_{ox} = 150 kg/(m^2s). The HTPB + 10% Al74-Cu26 formulation exhibits +22.6 %, while HTPB + 10% Al15-Cu85 exhibits $\Delta r_{f,\%}$ = +18.4 % . The poorest performance are achieved by the Al47-Cu53 loaded fuel. For G_{ox} = 350 kg/(m^2s), a $\Delta r_{f,\%}$ = - 30.9 % is observed. The ALEX™ loaded fuel, which is the reference formulation for nano-sized additives in this study, exhibits a $\Delta r_{f,\%}$ = +15.2 % for G_{ox} = 350 kg/(m^2s), while for G_{ox} = 150 kg/m^2s regression rate decreases of 4.2 % with respect to HTPB baseline.

For fuel formulations loaded with uncoated powders, introduction of Copper is connected to an increase of r_f for low G_{ox}. In these conditions all the tested Al-Cu based formulations are characterized by enhanced regression rates with respect to the ALEX™ loaded fuel. Nevertheless Al15-Cu85 and Al74-Cu26 loaded fuels still result faster than HTPB + 10% ALEX™ at high flux conditions. For G_{ox}=350 kg/(m^2s), the percent r_f increase is 18.6 % using Al15-Cu85 and 15.9 % using Al74-Cu26. Mass burning rate increases are even better because of the higher density of Copper (8900 *kg/m³*) in comparison to Aluminum (2700 *kg/m³*). Moreover, in every case, Copper lowers the G_{ox} influence on fuel regression rate. This could be an advantage for a possible application of Al-Cu powders in a real HRE.

No clear relationship between Cu concentration in Al-Cu powders and their performance was identified in the work. The best performance are achieved using high concentration of Aluminum or Copper bimetallic powders. On the other hand, Al47-Cu53 and Al32-Cu68 powders exhibit the worst performances. This is probably connected to the presence of different types and concentration of intermetallic compounds. It is proved, in fact, that Aluminum and Copper can create new molecular structures during production of powders by EEW method [84]. Moreover these new materials exhibit different

mechanical and thermal proprieties with respect to the original metals [66]. Another aspect that could change powder combustion behavior is ingredient mixing. Copper in fact has an higher concentration on particle surface because its higher melting temperature [84]. In order to deepen this analysis XRD and high resolution TEM images are needed. From a macroscopic point of view, DSC-TG analysis exhibits a reduction in peak temperature that is function of Copper concentration in powders. Moreover a reduction of heat release and maximum heat flux are observed. Probably there is a connection between temperature, maximum heat flux of oxidation peak and r_f of hybrid fuels. The best powders from ballistic analysis (Al15-Cu85 & Al74-Cu26) exhibits, in fact, smaller heat release and maximum heat flux with respect to ALEX™, but oxidation peak temperature is considerably lower, especially for Al15-Cu85.

Introduction of Fluorel™ and Telomer n5, coating on powders is linked to a general reduction of r_f, especially for the fastest formulations. For high G_{ox}, the biggest r_f decrease is observed. At low oxygen flux conditions differences are smaller and there are cases in which coated formulation is faster than the uncoated one. On the other hand, coated powder loaded fuels exhibit, in general, a smaller influence of r_f on G_{ox}. Moreover Fluorel provide a better protection to oxidation of Aluminum. Coated powders could maintain high active metal concentrations for a longer time in comparison to uncoated particles [55].

In order to explain the different behavior of Coated and Uncoated powder loaded fuels, two main parameters could be considered. At first, coating increases, in general, specific surface of powders [28], secondly Fluorinated coating decomposition produces oxidizer species. Probably in high flux conditions, the increase of specific surface of powders overcomes the advantages connected to the higher concentration of oxidizer. For low G_{ox}, on the other hand, the lack of oxidizer is partially compensated by coating decomposition and this effect is more significant than reduction of powder specific surface.

8.2. Future Developments

This work of thesis offers many possible developments, in production of powders, characterization and test of powders inside fuel or propellants.

In order to better understand powders combustion behavior, a series of XRD and high resolution TEM analysis are needed. These tests could show types and concentrations of intermetallic compounds inside particles. Moreover it could be possible to understand the structure of powder in terms of disposition of ingredients. Then these data should be compared to DSC-TG results in order to understand the behavior of the different intermetallic compounds in combustion.

Another important aspect, which should be deeper analyzed, is the correlation between DSC-TG results of powder combustion in air and performances achieved using the same

particles inside a Hybrid fuel. A production of different powder types should be made. In this way it could be possible to establish the influence of all parameters. Powders used for this type of analysis must exhibit the maximum possible variability in terms of: oxidation peak temperature, heat release, maximum heat flux etc.

As regards coating, a wider range of Fluorinated Polymer could be tested. A particular work should be made to increase Fluorine concentration inside powders, changing polymer type or concentration. A higher quantity of Fluorine could be connected to a higher quantity of oxidizer species produced during decomposition of polymer. Moreover particles could be covered before passivation in air. Fluorel™ and organic polymer in general, in fact, are used to stabilize active aluminum content of powders. Indeed Alumina layer would be thinner than air passivated particles, so specific heat release in combustion could be higher.

In order to have a deeper knowledge about bimetallic Aluminum-Copper powders combustion in hybrid fuels, could be useful to perform some visualization using a high resolution camera. In particular differences in combustion with respect to ALEX™ burning dynamics must be observed. The same process could be made for coated powders. It could be possible to understand better, what is the real effect of coating in powder combustion. Further numerical analyses using chemical kinetic models could be made and compared with experimental results.

The last but not the least, Aluminum-Copper bimetallic powders could be tested inside a HTPB-AP based solid propellant. Copper oxide in fact has a catalytic effect on AP decomposition. Introduction of Al-Cu bimetallic powders could, theoretically increase burning rate.

Bibliography

[1] L.T. DeLuca, "Energetic Problems in Aerospace Propulsion", 3rd Edition, Premani, Milano, 2009, ch. 1.

[2] G.P. Sutton, "Rocket Propulsion Elements", 7th Edition, John Wiley & Sons, 2001.

[3] L.T. DeLuca, "Energetic Problems in Aerospace Propulsion", 3rd Edition, Premani, Milano, 2009, ch. 12.

[4] Y. Maisonneve and G. Lengellé, "Hybrid Propulsion: Past, Present and Future Perspectives", 8th International Workshop on Combustion and Propulsion, paper 08 pp. 1-16, Pozzuoli, Naples, 16-21 June 2002.

[5] L.T. DeLuca, "Energetic Problems in Aerospace Propulsion", 3rd Edition, Premani, Milano, 2009, ch. 11.

[6] E.I. Azarkevich, A.P. Il'in, D.V. Tikhonov and G.V. Yablunovskii, Electric erosion synthesis of ultrafine powders of alloys and intermetallic compounds, Physics and Chemistry of Materials Treatment, Scientific Research Institute of High Voltage, Tomsk, 1997.

[7] Yu.S. Nilborodenko and V.I. Itin, "High-temperature synthesis of intermetallic compounds", Tomsk University, Tomsk, 1989, pp. 3-4.

[8] A. Vorozhtov, A. Gromov, M. Lerner and N. Rodkevich, "Characterization and Analysis of Al Nanoparticles Passivated with Organic Layers for Energetic Applications", Energetic Materials for High Performance, Insensitive Munitions and Zero Pollution, 41th International Annual Conference of ICT, Tomsk, 2010.

[9] D. Altman and A. Holzman., "Overview and History of Hybrid Rocket Propulsion", Fundamentals of Hybrid Rocket Combustion and Propulsion, AIAA Progress in Astronautics and Aeronautics, Vol. 218, pp. 1-36, 2007.

[10] A. Ulrich, "The Soviet Armaments Industry", pp. 74-75, Routledge, 1993.

[11] L. Green, "Introductiory Considerations on Hybrid Rocket Combustion", vol. 15, pp. 451-484, Academic Press, New York, 1964.

[12] D. Altman, "Highlights in Hybrid Rocket Propulsion", 10th International Workshop on Combustion and Propulsion, paper 17.1 - 17.1.21, September 2003, Leric i- La Spezia.

[13] K. Munson, "World Unmanned Aircrafts", Jane's, 1988.

[14] W. Wagner and W.P. Sloan, "Fireflies and Other UAVs", Midland Publishing, 1992.

[15] COMMISSION, U.S. PRESIDENTIAL, "Report of the Presidential Commission on the Space Shuttle Challenger Accident", Vol. 1, ch. 4, 6th June 1986.

[16] B.J. Cantwell, Course Material for AA283, 2005, ch. 11, p. 8. on website: http://www.stanford.edu/~cantwell/AA283_Course_Material/AA283_Course_Notes/Ch_11_Hybrid_Rockets.pdf on November 2012.

[17] C. Carmicino, G. Giulietti, T. Marchione, F. Lavorgna and A. Russo Sorge, "Regression Rate Measurements in a Hybrid Rocket", Proceedings of the 8th International Workshop on Combustion and Propulsion, paper 13-1 to 13-10, Pozzuoli, 2002.

[18] C.Carmicino and A. Russo Sorge, "Investigation of the fuel regression Rate Dependence on Oxidizer Injection and Chamber Pressure in a Hybrid Rocket", AIAA paper 2003-4591, 2003.

[19] Sorge, C. Carmicino and A. Russo, "Progress in the Fuel Regression Rate Behaviour Understanding in a GOX/HDPE Hybrid Rocket" , Mechanical Engineering Congress, pp. 1-8, 2004.

[20] A. Bettella, M. Lazzarin, N. Bellomo, F. Barato, D. Pavarin and M. Grosse, "Testing and CFD Simulation of Diaphragm Hybrid Rocket Motors", 47th AIAA/ASME/SAE/ASEE Joint Propulsion Conference and Exhibit, San Diego, USA, 2011.

[21] F. Barato, N. Bellomo, M. Faenza, M. Lazzarin and A.Bettella, "A Numerical Model to Analyze the Transient Behavior and Instabilities on Hybrid Rocket Motors", 47th AIAA/ASME/SAE/ASEE Joint Propulsion Conference and Exhibit, San Diego, USA, 2011.

[22] M. Lazzarin, M. Faenza, F. Barato, N. Bellomo, A. Bettella, D. Pavarin and M. Grosse, "CFD Simulation of a Hybrid Rocket Motor with Liquid Injection", 47th AIAA/ASME/SAE/ASEE Joint Propulsion Conference and Exhibit, San Diego, USA, 2011.

[23] L. Casalino and D. Pastrone, "Optimal Design of Hybrid Rocket Motors for Launchers Upper Stages" , JPP Journal of Propulsion and Power, Vol. 24, No. 3, pp. 491-498, 2008.

[24] A. Biancotti and D. Pastrone, "Modeling Combustion Instability in Aluminized Hybrid Propellants" , 43rd AIAA/ASME/SAE/ASEE Joint Propulsion Conference and Exhibit, Cincinnati, USA, 2007.

[25] A. Reina, C. Paravan, F. Maggi, G. Colombo, L.T. DeLuca and M. Belkova, "Nanometric Powders Dispersion into Polymeric Matrix", in Proceedings of 4th EUCASS (European Conference for Aerospace Science), San Petersburg, Russia, 2011.

[26] L.T. DeLuca, L. Galfetti, F. Bosisio, H. Raina, A. Colombo and G. Colombo, "A Hybrid Microcombustor for Regression Rate Measurements" , in Proceedings of 57th International Astronautical Congress (IAC), 2006.

[27] C. Paravan, M. Viscardi, L.T. DeLuca and L. Prada López, "Anisotropy Effects in Hybrid Fuels Burning in a Micro-burner", in Proceedings of XX AIDAA Congress, Milan, Italy, 2009.

[28] E. Duranti, A. Sossi, N.G. Rodkevich, A.B. Vorozhtsov, M. I. Lerner, A.A. Gromov, C. Paravan and L.T. DeLuca, "Comparison Between Nano-sized Aluminum Powders with Different Coatings: Physical Analyses and Performance Test", in Proceedings of HEMs, 2010.

[29] A. Reina, G. Colombo, L.T. DeLuca, F. Maggi, I. Lesniak, D.B. Lempert and G.B. Manelis, "Magnesium and Aluminum Ignition in CO2 Atmosphere", in Proceedings of XX AIDAA Congress, Milan, Italy, 2009.

[30] L.T. DeLuca, L. Galfetti, G. Colombo, F. Maggi, A. Bandera, M. Boiocchi, G. Gariani, L. Merotto, C. Paravan and A. Reina , "Time-Resolved Burning of Solid Fuels for Hybrid Rocket Propulsion", Paper under press by Taurus Press, 2011.

[31] L.T. DeLuca, C. Paravan, A. Reina, E. Marchesi, F. Maggi, A. Bandera, G. Colombo and B.M. Kosowski, "Aggregation and Incipient Agglomeration in Metallized Solid Propellants and Solid Fuels for Rocket Propulsion", in Proceedings of the 46th AIAA Aerospace.

[32] G. Marxman and M.Gilbert, "Turbolent Boundary Layer Combustion in the Hybrid Rocket", in 9th International Symposium on Combustion, pp. 371-383, New York, 1963.

[33] G.A. Marxman, C.E. Wooldridge and R.J. Muzzy, Fundamentals of Hybrid Boundary Layer Combustion. AIAA Paper, No. 63-505, 1963.

[34] T.S. Lee and A. Potapkin, "The Performance of a Hybrid Rocket with Swirling GOx Injection", Novosibirsk, Russia, 2002.

[35] C. Lee, J. Lee and Y. Byun, "Effect of Induced Swirl Flow on Regression Rate of Hybrid Rocket Fuel by Helical Grain Configuration", EUCASS (European Conference for Aero-Space Sciences), Moscow, Russia, 2005.

[36] W. Knuth, M. Chiaverini, J. A. Sauer and D. J. Gramer, "Solid-Fuel Regression Rate Behavior of Vortex Hybrid Rocket Engines", Journal of Propulsion and Power, Vol. 18, 2002.

[37] M.A. Karabeyoglu, D. Altman and B.J. Cantwell, "Combustion of Liquefying Hybrid Propellants: Part I. General Theory", Journal of Propulsion and Power, 2002.

[38] E.W. Price, "Combustion of Aluminum in Solid Propellant Flames", AGARD Solid Rocket Motor Technology, N80-10281 0120, 1979.

[39] R.K. Sigman and E.W. Price, "Combustion of Aluminized Solid Propellants", American Institute of Aeronautics and Astronautics Inc.,1999.

[40] A. Marinovich, Mg-B Duel Metal Powders as Performance Enhancer for Solid Rocket Propellants, Master Thesis, Politecnico di Milano, 2009.

[41] V.A. Babuk, V.A. Vasilyev and M.S. Malakhov, "Condensed Combustion Products at the Burning Surface of Aluminized Solid Propellant", Journal of Propulsion and Power, Vol.15, No.6, November-December 1999.

[42] M.A. Daniel, "Polybutadiene Binder Systems for Polymer Bonded Explosives", Australian Governament Department of Defence, 2006.

[43] C. Paravan, "Effetti dell'Anisotropia nei Combustibili a Base di Paraffina per la Propulsione Ibrida", Master Thesis, Politecnico di Milano, 2008.

[44] L. Galfetti, L.T. DeLuca, P. Grassi, C. Paravan, V. Luoni, A. Bandera,G. Colombo, L. DeCillia, R. Sempio, and H. Raina, "Advances in Hybrid Propulsion", in 7th International Symposium on Special Topics in Chemical Propulsion, Kyoto, Japan, 2008.

[45] P.Atkins and L. Jones, "Principi di Chimica", 3th edition, Zanichelli, 1998.

[46] M. I. Lerner, N. V. Svarovskaya, S. G. Psakhie and O. V. Bakina, "Production Technology, Characteristics, and Some Applications of Electric Explosion Nanopowders of Metals", Nanotechnologies in Russia, Vol. 4, Nos. 11–12, pp. 741–757, Tomsk, 2009.

[47] V. V.Shamanskii and M. I. Lerner, "Synthesis of Nanoparticles by High-Power Current Pulses" ,Journal of Structural Chemistry, Vol. 45, pp. S111-S114, Tomsk, 2004.

[48] N. I. o. S. a. Technology, "NIST Chemistry WebBook," [Online]. Available: http://webbook.nist.gov/chemistry.

[49] A. Earnshaw and N. Greenwood, "Chemistry of the Elements", Butterworth-Heinemann, Oxford, 1997.

[50] A. Sossi, E. Duranti, C. Paravan, L.T. DeLuca, A. B. Vorozhtsov, A. A. Gromov, Y.I. Pautova, M. I. Lerner, N. G. Rodkevich, "Non-Isothermal Oxidation of Aluminum Nanopowder Coated by Hydrocarbons", Under Press, 2012.

[51] A. Sossi, E. Duranti, M. Manzoni, C. Paravan, L.T. DeLuca, A. B. Vorozhtsov, M.I. Lerner, N.G. Rodkevich, A.A. Gromov, N. Savin, "Combustion of HTPB-Based Solid Fuels Loaded with Coated Nanoaluminum", Combustion Science and Technology, Under Press, 2012.

[52] C. Paravan, Ballistic of Innovative Solid Fuel Formulations for Hybrid Engines, PhD Thesis, Politecnico di Milano,2012.

[53] Y.F. Ivanov, M.N.Osmonoliev and V.S.Sedoi, "Productions of Ultra-Fine Powders and Their Use in High Energetic Compositions", Propellants, Explosives, Pyrotechnics, Vol. 28, No. 6, 2003.

[54] A. Gromov, A. Ilyin, U. Foerter-Barth and U. Teipel, "Effect of the passivating coating type, particle size, and storage time on oxidation and nitridation of aluminum powders", Combustion, Explosion and Shock Waves, vol.42, pp. 177-184, 2006.

[55] A.A. Gromov, U. Förter-Barth, U. Teipel, "Aluminum nanopowders produced by electrical explosion of wires and passivated by non-inert coatings: Characterisation and reactivity with air and water", Powder Technology, Vol.164, pp. 111–115, 2006.

[56] Y. Kwon, A. A. Gromov, A.P. Ilyin and G. Rim, "Passivation process for superfine aluminum powders obtained by electrical explosion of wires", Applied Surface Science, Vol.211, pp. 57–67, 2003.

[57] O. Nazarenko, "Nanopowders Produced by Electrical Explosion of Wires", Proceedings of European Congress of Chemical Engineering, Copenhagen, September 2007.

[58] A. Sossi, E. Duranti, C. Paravan, L.T. DeLuca A. B. Vorozhtsov, A.A. Gromov, M. I.Lerner, N. G. Rodkevich and N. Savin, Coated nano-sized Aluminum powders: physicalanalyses and performance tests in hybrid propulsion, accepted for publication on Combustion Science and Technology, 2012.

[59] 3M, "3M Global Gateway Page," [Online]. Available: http://www.3m.com.

[60] HaloPolymer, "HaloPolymer[ENG]," [Online]. Available: http://www.halopolymer.ru.

[61] A. Gromov, A. Ilyin, V. An, F. Faubert, C. de Izarra, A. Espagnacq and L. Brunet, "Characterization of Aluminum Powders: I. Parameters of Reactivity of Aluminum Powders", Propellants, Explosives, Pyrotechnics, Vol.27, pp. 361-364, 2007.

[62] L. Chen, W. L. Song, J. Lv, L. Wang, and C. S. Xie, "Effect of Heating Rates on TG-DTA Results of Aluminum Nanopowders Prepared by Laser Heating Evaporation", Journal of Thermal Analysis and Calorimetry, Vol. 96, pp. 141-145, 2009.

[63] A. Gromov and V. Vereshchagin, "Study of aluminum nitride formation by superfine aluminum powder combustion in air", Journal of the European Ceramic Society, Vol. 24, pp. 2879–2884, 2004.

[64] A. Gromov, "Study of Non-isothermal Nitridation of Aluminum Nanopowders Passivated by Non-oxide Layers", Central European Journal of Energetic Materials, Vol. 3, pp. 65-72, 2006.

[65] Y. Zhu, K. Mimura, J. Lim, M. Isshiki and Q. Jiang, "Brief Review of Oxidation Kinetics of Copper at 350 °C to 1050°C ", Metallurgical and Materials Transactions A, Vol.4, pp. 1231-1237, 2006.

[66] D.M.Rabkin, V.R.Rayabov, A. V. Lozovskaya and V. A.Dovzhenko, "Preparation and Proprieties of Copper-Alluminium Intermetallic Compounds", Metallurgy and Metal Ceramics , vol. 9, pp. 695-700, 1970.

[67] T. A. Sviridova, A. P. Shevchukov, E. V. Shelekhov and P. A. Borisova, "Use of Mechanical Alloying and Subsequent Annealing for Obtaining Intermetallic Compound CuAl2", National Research Technological University (Moscow Institute for Steel and Alloys), 2011.

[68] C. Paravan, A. Sossi, A. Reina, G. Massini, M. Manzoni, E. Duranti, G. Rambaldi, A. Adami, E. Seletti, and L.T. DeLuca, Micro and Nano-sized Metal Additives for Solid Fuels in Hybrid Rocket Lab-scale Burner, under press in Advances in Propulsion Physics, Vol. 4, 2012.

[69] L.T. DeLuca, L. Galfetti, G. Colombo, F. Maggi, A. Bandera, M. Boiocchi, G. Gariani, L. Merotto, C. Paravan, and A. Reina, "Time-Resolved Burning of Solid Fuels for Hybrid Rocket Propulsion", Advaces in Propulsion Physics, Vol. 2, 2011.

[70] C. Paravan, A. Reina, A. Sossi, M. Manzoni, G. Massini, G. Rambaldi, E. Duranti, A. Adami, E. Seletti, and L.T. DeLuca, Time-resolved Regression Rate of Innovative Hybrid Solid Fuel Formulations, 4th European Conference for Aerospace Sciences (EUCASS), 2012.

[71] M. Romano, "Influenza della pressione sui processi di ablazione in propulsione spaziale", Master Thesis, Politecnico di Milano, 1991.

[72] F. Bosisio, Progetto e Realizzazione di un Banco Sperimentale per un Microcombustore Ibrido, Master Thesis, Politecnico di Milano, 2007.

[73] L.T. DeLuca, L. Galfetti, F. Bosisio, H. Raina, F. Maggi, G. Colombo, "An Hybrid Micro-combustor for Regression Rate Measurements", Proceedings of the 57th IAC (International Astronautical Congress), Valencia, october 2006.

[74] C. Paravan, M. Viscardi, L.T. DeLuca and A. Kazakov, ""Regression Rates and Anisotropy Effects in Hybrid Rockets Microburner", Versailles, 2009".

[75] L.T. De Luca, L. Galfetti, G. Colombo, F. Maggi, A. Bandera, M. Boiocchi, G. Gariani, L. Merotto, C. Paravan, and A. Reina, Time-Resolved Burning of Solid Fuels for Hybrid Rocket Propulsion, EUCASS 2010, 2010.

[76] A. Green, "Effetti del Transitorio di Ignizione sulla Balistica di Combustibili Metallizzati per la Propulsione Ibrida", Master Thesis, Politecnico di Milano, 2010.

[77] G.A. Marxman, "Boundary Layer Combustion in Propulsion" , 11th Symposium (International) on Combustion, Pittsburgh, 1967.

[78] G.A. Marxman and C.E. Wooldridge., "Research on the Combustion Mechanism of Hybrid Rockets", Advances in Tactical Rocket Propulsion, Penner, pp. 421-477, 1968.

[79] M. Manzoni, "Experimental Investigation and Modeling of Solid Fuel Regression Rate for Hybrid Propulsion", Master Thesis, Politecnico di Milano, 2012.

[80] G.A. Marxman and M. Gilbert, "Turbulent Boundary Layer Combustion in the Hybrid Rocket", 9th Symposium (International) on Combustion, New York, 1963.

[81] B. Evans, N. A. Favorito, E.Boyer, G.A. Risha, R.B. Wehrman and K.K. Kuo, "Characterization of Nano-Sized Energetic Particle Enhancement of Solid-Fuel Burning Rates in an X-Ray Transparent Hybrid Rocket Engine", 40th AIAA/ASME/SAE/ASEE Joint Pro.

[82] L. Fanton, C. Paravan and L. T. De Luca, "Testing and Modeling Fuel Regression Rate in a Miniature Hybrid Burner", International Journal of Aerospace Engineering, Volume 2012, Article ID 673838.

[83] A. Ilyin and A. Gromov, "Characterization of Aluminum Powders: II. Aluminum Nanopowders Passivated by Non-Inert Coatings", Propellants, Explosives, Pyrotechnics 31, No. 5 (2006).

[84] E.I. Azarkevich, A.P. II'in, D.V. Tikhonov and G.V. Yablunovski, ""Electric erosion synthesis of ultrafine powders of alloys and intermetallic compounds", Physics and Chemistry of Materials Treatment, Scientific Research Institute of High Voltage, Tomsk, 1997".

[85] Rodrigo I Caro, John M Bellerby and Esam Kronfli, "Characterization and Thermal Decomposition Studies of a Hydroxil Terminated Polyether (HTPE) Copolymer and binder for composite rocket propellants", Department of Environmental and Ordnance Systems, Cranfield University, United Kingdom.

Appendix A

Table A.1: HTPB + 10% ALEX™ burning under Gox, data consistency checks. Percentages evaluated with respect to TOT value.

ID Test	Equation(6.10)	Equation(6.11)	Equation(6.12)
1	-0.548	3.063	1.656
2	0.043	-0.694	3.445
3	2.725	-2.471	-1.053
4	-2.146	-9.757	2.954
5	-0.078	-1.030	2.814

Table A.2: HTPB + 10% ALEX™ Coated burning under Gox, data consistency checks. Percentages evaluated with respect to TOT value.

ID Test	Equation(6.10)	Equation(6.11)	Equation(6.12)
1	1.890	-3.879	-0.751
2	0.428	-4.024	2.187
3	0.320	-3.176	0.655
4	-0.517	-2.469	0.898
5	0.488	-3.695	2.296
6	-0.383	0.302	-0.766

Table A.3: HTPB + 10% Al85-Cu15 burning under Gox, data consistency checks. Percentages evaluated with respect to TOT value.

ID Test	Equation(6.10)	Equation(6.11)	Equation(6.12)
1	0.400	1.917	-1.975
2	1.410	-1.237	-1.083
3	0.910	-5.977	0.835
4	-1.774	1.516	-0.281

Table A.4: HTPB + 10% Al85-Cu15 Coated burning under Gox, data consistency checks. Percentages evaluated with respect to TOT value.

ID Test	Equation(6.10)	Equation(6.11)	Equation(6.12)
1	0.036	1.323	0.1651
2	-0.114	0.456	-4.414
3	0.150	-2.843	2.684

Table A.5: HTPB + 10% Al74-Cu26 burning under Gox, data consistency checks. Percentages evaluated with respect to TOT value.

ID Test	Equation(6.10)	Equation(6.11)	Equation(6.12)
1	-0.671	2.789	-0.175
2	0.331	1.006	1.273
3	1.391	-4.425	4.074

Table A.6: HTPB + 10% Al74-Cu26 Coated burning under Gox, data consistency checks. Percentages evaluated with respect to TOT value.

ID Test	Equation(6.10)	Equation(6.11)	Equation(6.12)
1	-1.022	-1.150	0.263
2	0.715	-2.390	-1.083
3	-1.623	-2.162	-0.434
4	0.606	-0.583	-4.506

Table A.7: HTPB + 10% Al47-Cu53 burning under Gox, data consistency checks. Percentages evaluated with respect to TOT value.

ID Test	Equation(6.10)	Equation(6.11)	Equation(6.12)
1	0.216	-3.810	1.628
2	0.269	-0.975	-0.670
3	0.623	-4.964	0.624
4	-1.089	1.961	3.765

Table A.8: HTPB + 10% Al47-Cu53 Coated burning under Gox, data consistency checks. Percentages evaluated with respect to TOT value.

ID Test	Equation(6.10)	Equation(6.11)	Equation(6.12)
1	-0.656	0.647	0.464
2	0.664	-2.362	0.527
3	0.100	-1.791	-3.413
4	1.205	-1.058	2.929
5	-0.443	-1.164	-0.038
6	0.418	-1.142	-1.691

Table A.9: HTPB + 10% Al32-Cu68 burning under Gox, data consistency checks. Percentages evaluated with respect to TOT value.

ID Test	Equation(6.10)	Equation(6.11)	Equation(6.12)
1	0.104	-0.479	-2.217
2	-1.504	-0.187	-1.411
3	0.110	-3.319	1.664
4	-0.219	2.351	0.669

Table A.10: HTPB + 10% Al32-Cu68 Coated burning under Gox, data consistency checks. Percentages evaluated with respect to TOT value.

ID Test	Equation(6.10)	Equation(6.11)	Equation(6.12)
1	-0.358	-2.413	2.469
2	-0.100	-1.076	3.133
3	-0.396	0.495	3.139
4	-0.169	-2.190	1.557
5	-0.766	0.602	-2.413

Table A.11: HTPB + 10% Al15-Cu85 burning under Gox, data consistency checks. Percentages evaluated with respect to TOT value.

ID Test	Equation(6.10)	Equation(6.11)	Equation(6.12)
1	-0.316	1.220	0.841
2	-0.121	-0.374	0.529
3	0.169	-0.535	-0.666

Table A.12: HTPB + 10% Al15-Cu85 Coated burning under Gox, data consistency checks. Percentages evaluated with respect to TOT value.

ID Test	Equation(6.10)	Equation(6.11)	Equation(6.12)
1	-0.940	2.223	-1.234
2	-0.253	0.634	-0.151
3	0.052	0.190	-2.809
4	0.168	-0.366	0.286
5	-0.129	-3.342	0.603

Table A.13: HTPB + 10% Copper burning under Gox, data consistency checks. Percentages evaluated with respect to TOT value.

ID Test	Equation(6.10)	Equation(6.11)	Equation(6.12)
1	0.346	-2.220	-0.804
2	0.054	-3.823	-3.527
3	0.095	-2.833	-0.761
4	-0.318	-2.916	-2.744
5	-0.101	0.945	-2.637
6	-0.084	1.433	-1.718